UNIVERSIDAD TÉCNICA FEDERICO SANTA MARÍA
DEPARTAMENTO DE INGENIERÍA MECÁNICA
VALPARAÍSO - CHILE

TURBULENT CONVECTIVE FLOWS IN A DIFFERENTIALLY HEATED CAVITY: A GLOBAL AND LOCAL ANALYSIS

MATÍAS SÁEZ BARRAZA

TESIS DE GRADO PARA OPTAR AL GRADO DE:
MAGISTER EN CIENCIAS DE LA INGENIERÍA MECÁNICA

Y AL TÍTULO DE:
INGENIERO CIVIL MECÁNICO

PROFESOR GUÍA: DR. ING. OLIVIER SKURTYS
PROFESOR CO-REFERENTE: DR. ING. ROMAIN GERS

MAYO - 2026

CONSTANCIA DE VALIDACIÓN Y CONFIDENCIALIDAD DE MONOGRAFÍA A REPOSITORIO ACADÉMICO

1.- IDENTIFICACIÓN DEL TRABAJO ACADÉMICO

Tipo de monografía (marcar una opción): ☐ Memoria o trabajo de título; ☒ Tesis de Postgrado;

Título del trabajo: Turbulent Convective Flows in a Differentially Heated Cavity: A Global and Local Analysis

Nombre del candidato(a): Matías Ignacio Sáez Barraza

Carrera / Grado: Magíster en Ciencias de la Ingeniería Mecánica

Campus: Casa Central Valparaiso **;** **Departamento**: Departamento de Ingeniería Mecánica

2.- VALIDACIÓN DEL PROFESOR GUÍA/DIRECTOR DE TESIS

Yo, Olivier Skurtys, en mi calidad de profesor(a) guía/director(a) del trabajo académico mencionado anteriormente **DEJO CONSTANCIA** que:

- He revisado esta versión del documento y corresponde a la versión final aprobada del trabajo.
- El trabajo cumple con los requisitos académicos y de formato establecidos por la institución

3.- EVALUACIÓN DE CONFIDENCIALIDAD POR PROPIEDAD INDUSTRIAL

☒ El trabajo **NO contiene información que amerite confidencialidad** y puede ser publicado de inmediato en repositorio con acceso abierto.

☐ El trabajo **CONTIENE** información con potenciales implicancias de propiedad industrial o intelectual y requiere un periodo de confidencialidad (embargo) por:

☐ 6 meses; ☐ 12 meses; ☐ 2 años; ☐ 3 años; ☐ 5 años; ☐ 10 años

Fundamentación de la necesidad de confidencialidad (obligatorio si se solicita embargo):

4.- FIRMAS

Profesor(a) guía o director(a) de memoria o tesis:

Fecha: 24/06/2026 **; Firma:** ____________________

Estudiante o Candidato(a):

Fecha: 24/06/2026 **; Firma:** ____________________

Este formulario debe ser insertado como página 2 de la memoria o tesis, completado y firmado por estudiante y profesor(a) antes de la entrega en portal PRISMA de Biblioteca USM.

"Observa constantemente que todo lo que acontece es el resultado de un cambio, y acostúmbrate a pensar que la naturaleza no ama nada tanto como cambiar las cosas que son y crear otras semejantes."

Marco Aurelio

"El azar (tal es el nombre que nuestra inevitable ignorancia da al tejido infinito e incalculable de causas y efectos), ha sido muy generoso conmigo."

Jorge Luis Borges

Agradecimientos

Con este manuscrito culmina uno de los desafíos más difíciles e importantes de mi vida. Un camino marcado por momentos de incertidumbre, pero también de profundo crecimiento. Un camino que, sin el apoyo incondicional de todos aquellos que creyeron en mí, jamás habría logrado recorrer. Las siguientes líneas comprenden un modesto intento por expresar la gratitud que siento en este momento.

Agradezco, en primer lugar, a toda mi familia, por el infinito amor que me entregaron, ese que me hizo sentir que todo es posible. A mis padres, por su esfuerzo permanente, que me otorgó todo lo necesario para llegar a ser la persona que soy hoy. Su confianza en mí, su orientación y su apoyo incondicional. Agradezco el haberme enseñado las ganas de aprender, el querer dar lo mejor de uno mismo y el buscar siempre hacer las cosas con amor. A mis hermanos, por ser un ejemplo a seguir, impulsándome continuamente a superarme, por alimentar mi curiosidad, por estar ahí en cualquier situación y por nunca dudar de mí. A Estefanía, por su inagotable paciencia, por su ayuda en los momentos en que más la necesité y por mostrarme una nueva forma de ver la vida.

Agradezco a todos mis amigos, quienes fueron parte fundamental de esta experiencia. Gracias por el apoyo, las risas, las enseñanzas y por acompañarme a crecer. Ustedes son la pieza que hizo de la universidad algo más que un camino académico, convirtiendo todos estos años en recuerdos imborrables.

Agradezco a mis profesores por introducirme a esta hermosa área del conocimiento, por su guía y apoyo, por darme la oportunidad de formar parte de esta investigación y por permitirme descubrir mis capacidades.

Finalmente, agradezco profundamente el financiamiento otorgado por ANID–Subdirección de Capital Humano/Beca Magíster Nacional/2025–22251015, al Programa de Incentivo a la Iniciación Científica (PIIC) de la Universidad Técnica Federico Santa María y al Departamento de Ingeniería Mecánica de la Universidad.

Gracias a todos.

Abstract

This study examines turbulent natural convection in a three-dimensional differentially heated cavity with no-slip boundary conditions using direct numerical simulation. Unlike commonly used periodic configurations, the presence of physical walls enables the development of fully three-dimensional structures that significantly alter the flow stability and turbulent dynamics. The vertical and horizontal aspect ratios are 4 and 1, respectively. Simulations are performed using the `Nek5000` spectral element solver, while scripts are written in `Python` and `MATLAB` for post-processing.

Instability onset occurs at critical Rayleigh numbers of $Ra_c \approx 2.8 \times 10^8$, substantially higher than in periodic domains, demonstrating the strong stabilizing effect of no-slip boundaries. At $Ra = 10^{10}$, the flow is turbulent but not fully developed: the boundary layers lack a logarithmic region, and spectral analysis reveals only a limited inertial subrange. Compared to periodic configurations, global heat transfer is reduced, while the mean temperature profile remains consistent, suggesting that discrepancies with experiments are more likely attributable to thermal radiation effects.

The vertical boundary layer exhibits a progression from multimodal behavior through an intermediate monoperiodic state to chaotic dynamics. The intermediate regime is dominated by a frequency approximately four times higher than that of Tollmien–Schlichting waves. Turbulence is concentrated in the detachment region, where shear production dominates and buoyancy plays a secondary role. The PDFs of the velocity-gradient invariants exhibit the characteristic teardrop shape, indicating a predominance of tube-like vortex stretching and rare but intense biaxial strain events. Coherent structures originate in the boundary layer, are advected upward, and are intermittently ejected into the stratified core, where they dissipate and excite internal gravity waves at the Brunt–Väisälä frequency.

These results provide insight into the mechanisms governing turbulent natural convection, highlight the critical role of confinement and wall boundary conditions in shaping transition and turbulence in buoyancy-driven flows, and establish a reference dataset for the validation of turbulence models in non-periodic geometries.

Contents

List of Figures

List of Tables

Chapter 1

Introduction

1.1 Motivation and Background

The investigation of the mechanisms governing natural convection phenomena within a Differentially Heated Cavity (DHC) has been the focal point of numerous research works in recent years. Given the significant industrial relevance in applications such as air-conditioning [1], electronic equipment cooling [2], double-paned windows [3], solar collectors [4], and heat exchangers, understanding and intentionally manipulating the heat transfer is crucial for energy conservation, addressing one of the most important challenges in the modern era. However, flows within a DHC are inherently complex, as various flow patterns can emerge, ranging from steady states to fully turbulent regimes, depending on the geometry, thermophysical properties of the fluid, temperature difference, and boundary conditions. This complexity renders both numerical and experimental investigations demanding tasks, requiring continuous contributions to the field.

Among the countless patterns nature weaves, few are as captivating and elusive as turbulence, whose hidden dynamics remind us that even within the simplest boundaries, complexity abounds. Turbulent shear flows, such as those observed in a DHC at particularly high Rayleigh numbers, are characterized by organized vortical motions that persist spatially and evolve over time, commonly referred to as coherent structures [5]. Extracting, tracking, and interpreting these structures has become a crucial pursuit in analyzing and comprehending momentum and energy transfer processes [6]. While past studies have identified instabilities, questions remain regarding the generation, dissipation, and dynamics of coherent structures. In this context, the DHC serves itself as a representative case, offering a well-defined environment to investigate how unsteadiness develops and how turbulent convection is shaped. Thus, the global and local analysis of this system is of special importance for advancing the understanding of turbulent natural convection.

The concept of a DHC was theoretically introduced by Batchelor [7]. Gill later proposed a boundary layer model for a 2D rectangular cavity with height much larger than its width and high Prandtl numbers [8]. This model was further refined by Bejan to include adiabatic boundary conditions at the horizontal walls [9]. Early direct numerical studies focused on 2D configurations under steady laminar regimes at low Rayleigh numbers for air-filled square cavities ($Pr = 0.71$), such as the benchmark proposed by de Vahl Davis [10].

Subsequent research shifted toward the transition to turbulence. As the Rayleigh number increases, beyond a critical value (Ra_c), instabilities arise and the flow becomes time dependent (periodic, chaotic and finally fully turbulent) [11]. Paolucci and Chenoweth investigated this transition across various Ra values and geometries [12]. They found that at the beginning of the transition, two frequencies of oscillation appear, the lower one associated with the stratified core region (related to the Brunt–Väisälä frequency) and the higher one originating in the boundary layer (associated with Tollmien–Schlichting waves).

Janssen et al. [13] studied steady and time-periodic air flow in a 3D cubical cavity, suggesting that the instability mechanisms responsible for the bifurcation are analogous to those in the 2D case. Le Quéré and Behnia [14] analyzed the three values $Ra = 6.4 \times 10^8$, $Ra = 2 \times 10^8$ and $Ra = 10^{10}$, noting for the first periodic oscillations of the isotherms in the downstream part of the boundary layer, which corresponds to the primary instability, in the form of Tollmien–Schlichting waves. As the cavity boundary layer thins with increasing Ra, higher spatial resolution is required, making the computation more demanding.

Solutions for $Ra \leq 10^8$ in this configuration have been obtained using various methods, such as in the work of Le Quéré [15]. Among enclosure geometries, square cavities and rectangular cavities with an aspect ratio of 4:1 (height-to-width) are the most extensively studied. In the latter, the transition to turbulence is believed to begin in the boundary layer due to Tollmien–Schlichting waves that propagate and disrupt the thermally stratified core region, generating gravity waves. Hopf bifurcations (i.e. periodic oscillatory behavior) were identified in the transitional regime at $Ra = 1.03 \times 10^8$ and a chaotic behavior at $Ra = 2.3 \times 10^8$ by Le Quéré [16]. Further studies by Xin and Le Quéré [17] explored chaotic regimes up to $Ra = 10^{10}$, while Trias et al. [11] carried out simulations up to $Ra = 10^{11}$. Additionally, critical values of $Ra = 1.032 \times 10^8$ for 2D oscillatory disturbances and $Ra = 2.141 \times 10^7$ for 3D stationary disturbances were reported by Xin and Le Quéré [18].

Nonetheless, the majority of numerical studies rely on the 2D assumption or periodic boundary conditions at the front and rear walls, which can lead to inconsistent solutions. Stability in a 2D cavity differs significantly from that in a 3D cavity; however, 2D mechanisms emerge as the cavity depth increases. Gers et al. [19] investigated the three-dimensional effects induced by depth variation in a DHC of vertical aspect ratio equal to 4 at $Ra = 10^8$, where heat transfers, flow dynamics and structures were analyzed. Their findings highlighted the significant impact of the rear and front boundary conditions on the flow topology. In particular, the imposition of no-slip boundary conditions on the front and rear walls (as opposed to the commonly employed periodic conditions) introduces additional physical mechanisms that can alter the onset of instability and the organization of turbulent motions.. This investigation addresses these gaps. By examining turbulent convective flows within a 3D-DHC, this work confronts fundamental questions whose resolution promises not only practical engineering insight but also a glimpse into the hidden symmetries by which nature organizes chaos.

1.2 Objectives

The main objective of the investigation is to numerically investigate the behavior of the turbulent convective flow within a 3D-DHC using no-slip conditions in the front and rear walls. Specifically, this research aims to:

- Determine the critical value of the Rayleigh number (Ra_c), analyzing its variation along the depth of the cavity and comparing these results with benchmarks using periodic boundary conditions.
- Provide a comprehensive characterization of the turbulent flow through the calculation of key parameters, including characteristic scales (Kolmogorov and Taylor), energy spectra, boundary layer thickness, and turbulent correlations.
- Characterize the mechanisms governing the generation and dissipation of coherent structures by correlating the Brunt–Väisälä frequency in the cavity core with structure formation and verifying the role of Tollmien–Schlichting waves in the destabilization process.

Chapter 2

Differentially Heated Cavity

2.1 Problem Formulation

Consider a 3D differentially heated cavity of height H, width W and depth D. The vertical aspect ratio $A_z = \frac{H}{W}$ is set equal to 4, while the horizontal aspect ratio $A_y = \frac{D}{W}$ is set to 1 (square-based cavity). The left and right vertical walls (positioned along x-direction) are maintained at fixed temperature of T_c and T_h, respectively. The top and bottom walls are perfectly adiabatic. A Newtonian fluid, specifically air, is the working fluid, which has a kinematic viscosity of ν, thermal diffusivity α, thermal expansion coefficient β, and density ρ. To simplify the governing equations while maintaining high accuracy, all properties are evaluated at a reference temperature (i.e. $T_0 = \frac{T_h+T_c}{2}$). In addition, the fluid is assumed to be an incompressible gas. Gravity acts in the negative z-direction.

A schematic diagram of the DHC is shown in Figure 2.1. The coordinate system origin is located at the front, left, bottom corner. Initially, the fluid is at rest in a state of thermal uniformity and hydrostatic equilibrium. In this study, thermal radiation is neglected. It is worth noting that the accuracy of the results improves when simulations are expanded from 2D to 3D and when radiation transfer effects are included. Indeed, previous work [20] suggests that discrepancies between experimental results and numerical simulations arise from the omission of radiation transfer, water vapor content, or inconsistent boundary conditions. The aspect ratio of 4 was chosen because the transition to turbulence in this geometry has been extensively documented, the critical parameters and structures show similarities to the 2D case, and the configuration offers specific numerical advantages when high-order polynomials are used [17].

The fluid motion is driven by the imposed temperature gradient, which transports heat from the hot

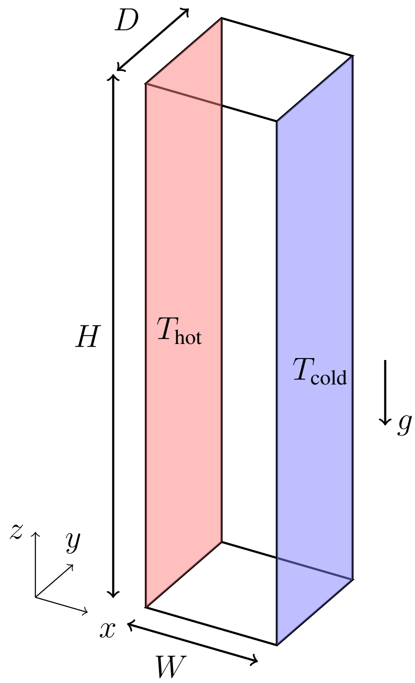

Figure 2.1: Schematic diagram of the differentially heated cavity.

wall to the cold one, and by buoyancy forces arising from gravity acting on the resulting density variations along the z-axis. When these buoyancy forces become sufficient to overcome viscous and thermal diffusive resistance, the fluid departs from the purely conductive, hydrostatic state and a steady convective circulation develops. As a fluid parcel in contact with the hot wall is heated, its density decreases and it rises due to buoyancy; conversely, fluid adjacent to the cold wall becomes denser and sinks. This motion organizes into a large recirculating cell that encloses a thermally stratified core region.

This stratification arises because convective transport, which carries warm and cold fluid between the vertical walls, is nearly balanced by thermal diffusion that smooths temperature gradients within the cavity interior. The resulting equilibrium limits mixing in the core while preserving a stable vertical temperature gradient. Simultaneously, thin thermal and velocity boundary layers develop along the heated and cooled walls, where most of the temperature and velocity variations are confined. Downstream, convective jets impinge on both the top and bottom walls, introducing localized mixing, shear, and recirculation in the interaction region between vertical and horizontal walls. As the convective motion intensifies, complex interactions emerge between the dynamic and thermal boundary layers, giving rise to instability mechanisms, internal gravity waves, and enhanced thermal stratification, marking the onset of turbulent regime. The dimensionless parameter that characterizes the relative strength of buoyancy to viscous and diffusive effects is the Rayleigh number (Ra). Larger values of Ra indicate that buoyancy forces dominate over dissipative effects, leading to increasingly vigorous and unstable convective motion.

2.2 Flow Instabilities

At low Rayleigh numbers, the flow inside the cavity remains steady, laminar, and symmetric. As the Rayleigh number increases and reaches a critical value (Ra_c), the steady solution loses stability through a supercritical Hopf bifurcation, leading to the onset of time-dependent behavior. This bifurcation can be illustrated schematically in the two–dimensional phase portrait shown in Figure 2.2, where solid lines denote stable states and dashed lines represent unstable ones. The control parameter (μ), corresponding here to the Rayleigh number, reaches a critical threshold at which the system transitions from a stationary equilibrium to a stable periodic oscillation. In this representation, r indicates the amplitude of the oscillatory motion, which can be associated with physical variables such as velocity or temperature.

Beyond this threshold, the flow exhibits a monoperiodic oscillation, characterized by a single dominant frequency. For a 2D cavity with a vertical aspect ratio 4, the critical Rayleigh number is approximately $Ra = 1.032 \times 10^8$ [18]. Tollmien–Schlichting waves traveling downstream are believed to be the primary mechanism responsible for the destabilization of the boundary layer [21]. For two-dimensional flow, the natural frequency of these waves was reported to be $\omega \approx 2.5$ [16], whereas

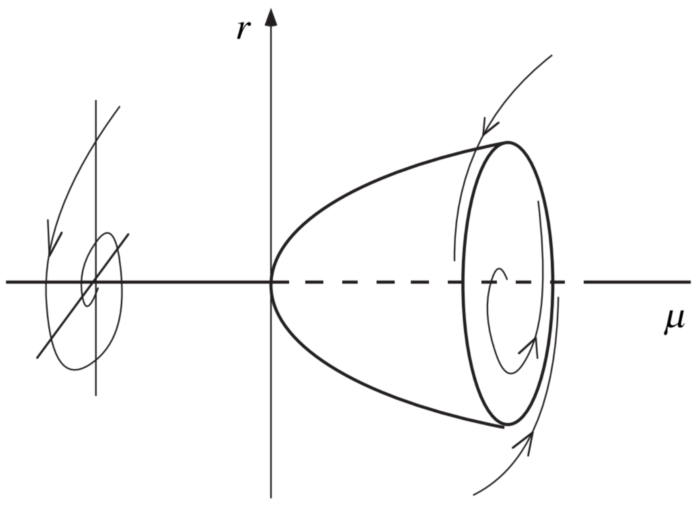

Figure 2.2: Two–dimensional diagram of a supercritical Hopf bifurcation. Reproduced from [22].

for three-dimensional flow with periodic boundary conditions in the rear and front walls, a slightly higher value of approximately $\omega \approx 2.73$ was observed [18]. The transition initially results in a two-dimensional time-dependent flow. Although weak three-dimensional stationary instabilities may appear before the onset of 2D time-dependent flow, they induce only a minor velocity component in the spanwise direction. Consequently, the transition to time dependence still occurs primarily through the emergence of traveling waves along the vertical boundary layers, as in the purely two-dimensional case [18].

A further increase in Ra introduces additional frequencies as secondary instabilities develop, giving rise to biperiodic and, subsequently, quasi-periodic regimes. With the continued growth of thermal forcing, nonlinear interactions among these oscillatory modes intensify, eventually driving the system toward a chaotic or turbulent state where coherent structures coexist with irregular temporal fluctuations. As the boundary-layer instabilities grow in amplitude with increasing Ra, they induce the ejection of larger-scale structures that interact with the stably stratified core of the cavity. The core region responds dynamically to this forcing by supporting internal gravity waves and begins to oscillate around a mean horizontal profile at the Brunt–Väisälä frequency. This characteristic frequency depends on the thermal properties of the fluid, represented by the Prandtl number (Pr), and the dimensionless vertical temperature gradient, $\partial\theta/\partial z$. In its nondimensional form, the Brunt–Väisälä frequency can be expressed as shown in Equation 2.1 [16], which quantifies the restoring force acting on a displaced fluid parcel within a stably stratified layer and governs the oscillatory behavior of the core region:

$$N = \frac{1}{2\pi}\sqrt{Pr\,\frac{\partial\theta}{\partial z}}. \tag{2.1}$$

At high Rayleigh numbers, characterizing fully turbulent regimes, significant discrepancies arise between 2D and 3D simulations [23]. In these states, the flow becomes inherently three-dimensional due to the breakdown of symmetry and the development of spanwise fluctuations. Consequently, three-dimensional simulations are essential to provide a more accurate representation of the flow physics and to resolve the complex vortex dynamics and heat transfer mechanisms present under such conditions.

2.3 Turbulent Flow

Turbulence is characterized as a complex state of fluid motion in which the vorticity field ($\boldsymbol{\omega} = \nabla \times \boldsymbol{u}$, where $\boldsymbol{u}$ denotes the velocity field) is continuously advected and distorted in a chaotic, non-linear manner [24]. This state emerges when inertial forces dominate over viscous effects, typically at high

Reynolds numbers (Re), leading to a cascade of energy across a wide spectrum of spatial and temporal scales. In the context of a differentially heated cavity, turbulence emerges as the buoyancy-driven flow becomes increasingly unstable with the rising Rayleigh number, eventually breaking the symmetry of the large-scale circulation and giving rise to fluctuating vortical structures. This regime is defined by inherently three-dimensional, aperiodic fluctuations in velocity, pressure, and temperature that exhibit a stochastic nature.

2.3.1 Energy Cascade

"Big whirls have little whirls that feed on their velocity, And little whirls have lesser whirls and so on to viscosity" (Lewis F. Richardson, 1922) [25]

One of the most fundamental concepts in turbulence theory is the energy cascade, which describes the nonlinear transfer of kinetic energy across a hierarchy of scales. Large-scale eddies, generated by flow instabilities or external forcing, contain most of the system's kinetic energy and set the overall dynamics of the flow. Through nonlinear inertial interactions, these large structures become unstable and fragment into progressively smaller eddies, transferring energy downward through the spectrum of scales [24]. This process continues until the smallest scales, where viscous effects dominate and

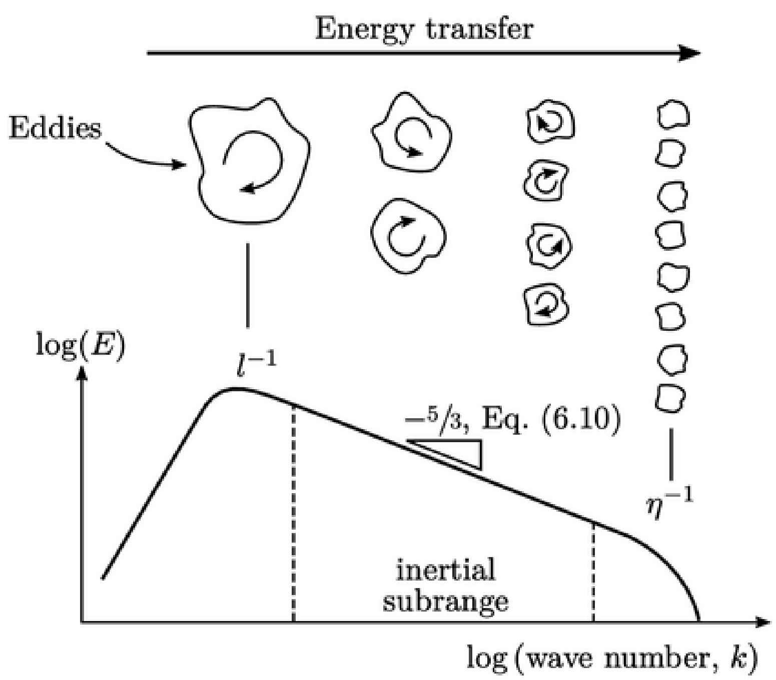

Figure 2.3: Schematic representation of the energy cascade with its corresponding energy spectrum graph. Reproduced from [27].

convert the remaining kinetic energy into heat through dissipation. The upper part of Figure 2.3 illustrates this mechanism schematically.

Kolmogorov formalized this framework by proposing that, at sufficiently high Reynolds numbers, small-scale motions in a turbulent flow become statistically universal and independent of the large-scale geometry or forcing conditions [26]. This universality holds under the assumption of homogeneous and isotropic turbulence (HIT), where statistical properties are invariant under spatial translations and rotations. Within this framework, the kinetic energy injected at the large scales cascades through intermediate scales, known as the inertial subrange. In this subrange, energy is neither produced nor dissipated but merely redistributed among scales at a constant mean transfer rate ε.

Dimensional analysis yields the characteristic $-5/3$ power law for the energy spectrum:

$$E(k) \sim \varepsilon^{2/3} k^{-5/3} \tag{2.2}$$

as shown in Figure 2.3, where k is the wavenumber ($k \propto l^{-1}$). Large structures correspond to small wavenumbers and contain the most energy, while small, low-energy eddies correspond to high wavenumbers. At the smallest scales, where viscous effects dominate, the energy spectrum exhibits an exponential decay. In contrast, the dissipation spectrum, defined as:

$$D(k) = 2\nu k^2 E(k) \tag{2.3}$$

identifies the contribution of each wavenumber to the total energy dissipation, with the peak occurring near the Kolmogorov scale. In the case of two-dimensional turbulence, the mechanism differs fundamentally and an inverse cascade is observed, where energy flows from smaller to larger scales, leading to the formation of large-scale coherent vortices [30].

Three characteristic length scales that describe the cascade process can be determined:

- The **integral scale** l, associated with the largest energy-containing eddies. At this scale, energy is injected into the system, and the flow retains strong anisotropy and high dependence on boundary conditions;
- The **Taylor microscale** λ, is an intermediate length scale that bridges the gap between the large-scale integral scale (l) and the small-scale Kolmogorov scale (η).
- The **Kolmogorov scale** η, associated with the smallest motions. At this scale, viscosity dominates, and the flow is assumed to approach local isotropy.

Table 2.1: Estimates of the length, time, and velocity scales of a fully turbulent flow, following Kolmogorov's similarity hypotheses [28], [29].

	Length	Velocity	Time	Re
Integral Scale	$l \sim \frac{e^{3/2}}{\varepsilon}$	$u_l \sim \sqrt{e}$	$\tau_l \sim \frac{e}{\varepsilon}$	$Re_l \sim \frac{u_l l}{\nu}$
Taylor Scale	$\lambda \sim \sqrt{10\frac{\nu e}{\varepsilon}}$	$u_\lambda \sim \sqrt{e}$	$\tau_\lambda \sim \frac{\lambda}{u_\lambda}$	$Re_\lambda = \frac{u_\lambda \lambda}{\nu}$
Kolmogorov Scale	$\eta \sim \nu^{3/4}\varepsilon^{-1/4}$	$u_\eta \sim (\nu\varepsilon)^{1/4}$	$\tau_\eta \sim \sqrt{\frac{\nu}{\varepsilon}}$	$Re_\eta = \frac{u_\eta \eta}{\nu} \sim 1$

These scales form a hierarchy that reflects the structure of the turbulent cascade. Estimates for the characteristic length, time, and velocity scales within a fully turbulent flow are summarized in Table 5.3. In this context,, $e = \frac{1}{2}\overline{u_i' u_i'}$ represents the turbulent kinetic energy per unit mass (TKE), where u_i' denotes the i–th ($i = 1, 2, 3$) component of the velocity fluctuations defined via the Reynolds decomposition:

$$\boldsymbol{u}(\boldsymbol{x}, t) = \overline{\boldsymbol{u}(\boldsymbol{x}, t)} + \boldsymbol{u}'(\boldsymbol{x}, t). \tag{2.4}$$

The separation between these scales increases with the Reynolds number. Specifically, according to Kolmogorov's similarity hypotheses, $l/\eta \sim Re_l^{3/4}$ and $\lambda/\eta \sim Re_l^{1/4}$, illustrating how high Reynolds numbers facilitate a broad inertial subrange where nonlinear interactions dominate energy transfer. Kolmogorov's theory remains a definitive milestone in the development of a general framework for turbulence, accounting for an impressive degree of realistic quantitative and qualitative behavior. Still, a substantial body of experimental and numerical work accumulated over the years makes it clear that the theory is not exact, even within the idealized framework of homogeneous isotropic turbulence [30].

In convective flows, structures within the temperature field also play an important role in the overall dynamics. The size of the smallest thermal structures, where molecular diffusion dominates over turbulent stirring, is defined by a characteristic thermal microscale. This scale is often compared to the Kolmogorov microscale. For fluids with $Pr \leq 1$ (such as air), the smallest scale is the Corrsin temperature microscale (η_T), which is defined as:

$$\eta_T = \left(\frac{\alpha^3}{\varepsilon}\right)^{1/4} = \frac{\eta}{\mathrm{Pr}^{3/4}}, \tag{2.5}$$

In this regime, the thermal diffusivity is comparable to or greater than the kinematic viscosity, meaning that temperature fluctuations are smoothed out by molecular diffusion at scales slightly larger than or equal to the smallest velocity structures. Consequently, for air, the temperature field remains relatively well-resolved if the velocity field satisfies the Kolmogorov criteria. For fluids with $Pr \gg 1$ (such as water or oils), molecular diffusivity is low, allowing for temperature fluctuations to persist down to the much smaller Batchelor microscale (η_B)

$$\eta_B = \left(\frac{\nu\alpha^2}{\bar{\varepsilon}}\right)^{1/4} = \frac{\eta}{\mathrm{Pr}^{1/2}}, \tag{2.6}$$

which is significantly smaller than η [31]. In such cases, the computational requirements for resolving the thermal field are considerably more demanding than those for the velocity field. However, for the present study using air ($Pr = 0.71$), the thermal and velocity scales are of the same order, simplifying the resolution requirements.

It is important to note that the assumptions of homogeneity and isotropy underlying Kolmogorov's theory are not strictly satisfied in buoyancy-driven, wall-bounded flows such as a differentially heated cavity. In this configuration, turbulence is inherently anisotropic at large and intermediate scales due to the presence of gravity, mean shear within the vertical boundary layers, and the formation of coherent structures. These mechanisms introduce preferred directions and spatial inhomogeneities that strongly influence the energy-containing scales and the global flow topology. Nevertheless, both experimental and numerical evidence suggest that, at sufficiently small scales, turbulence tends toward local isotropy as nonlinear interactions dominate over the large-scale anisotropic forcing. Consequently, Kolmogorov scaling arguments remain a valid framework for a local description of the dissipative range, even though deviations from idealized homogeneous isotropic turbulence framework may persist at larger scales of the spectrum.

2.3.2 Intermittency

According to Kolmogorov's similarity hypotheses [26], under the assumptions of homogeneity and isotropy, eddies of size r within the inertial subrange ($l \gg r \gg \eta$) are unaffected by viscosity and by the large energy-containing motions. Their statistics depend only on the mean rate of energy dissipation ε and the separation distance r. Dimensional analysis then leads to the classical K41 prediction for the scaling of the nth-order longitudinal structure functions:

$$S_n(r) = \langle |u_x(\mathbf{x} + r\hat{\mathbf{e}}_x) - u_x(\mathbf{x})|^n \rangle = C_n(\varepsilon r)^{n/3}, \tag{2.7}$$

where u_x denotes the longitudinal velocity component, x is the spatial position, r is the separation distance characterizing the scale of motion. The coefficient C_n represents a flow-dependent constant [32], and n is the order of the structure function. All quantities are treated as ensemble averages, equivalent to time averages in statistically steady flows, denoted by $\langle \bullet \rangle$. This scaling relationship describes how velocity increments $\delta u(r)$ vary across the inertial subrange and serves as a fundamental building block for the phenomenological description of the turbulent cascade. Specifically, one can define the normalized n-th order structure functions:

$$\sigma_n(r) = \frac{S_n(r)}{S_2(r)^{n/2}}, \tag{2.8}$$

which allow for the assessment of deviations from Gaussian behavior across various scales. Important statistical measures include:

- Standard deviation (σ_2): Characterizes the typical magnitude of the velocity differences at a given scale.
- Skewness (σ_3): Quantifies the asymmetry of the velocity increment probability distribution. In the context of the energy cascade, a non-zero skewness (specifically a negative value for longitudinal increments) is a hallmark of the energy transfer process. A value of zero corresponds to a perfectly symmetric distribution, such as a Gaussian.
- Kurtosis (σ_4): Often referred to as the flatness factor, it measures the tailedness of the velocity increment distribution. The value of 3 corresponds to a Gaussian distribution; values significantly greater than 3 indicate an intermittent signal with frequent high-amplitude fluctuations (heavy tails).

A direct implication of Kolmogorov's similarity hypotheses is that the statistics of velocity increments δu, including the probability density functions (PDFs) of the longitudinal velocity gradients $\partial u_x/\partial x$, which represent velocity differences across the viscous scale η, should be universal. In this idealized framework, the normalized structure functions would exhibit behavior independent of the Reynolds number. However, it has been demonstrated that this is not the case [33]: velocity-gradients become increasingly intermittent, with PDFs that develop progressively heavier tails as the Reynolds number increases ($\sigma_4(r) > 3$), as illustrated in Figure 2.4.

This reflects a signal in which $\partial u_x/\partial x$ remains near zero for the majority of the time, interrupted by rare and intense bursts associated with strong localized dissipation. Moreover, these intense gradients develop gradually throughout the inertial cascade. As depicted in Figure 2.5a, while velocity differ-

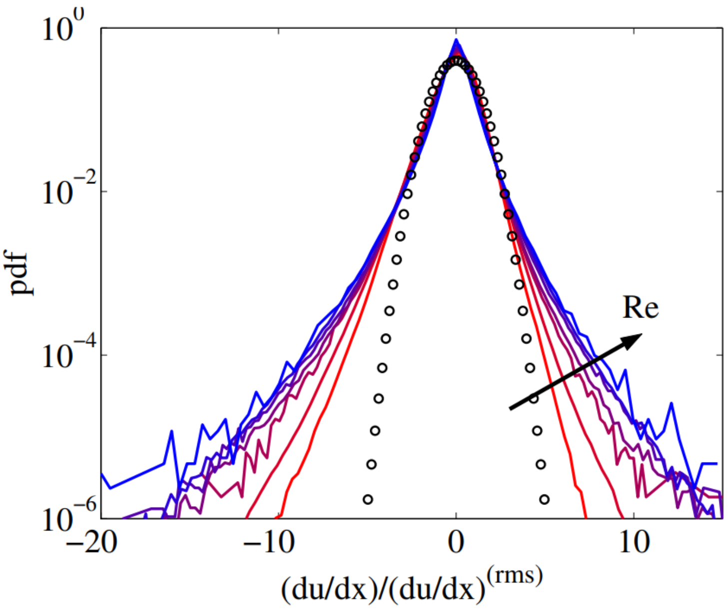

Figure 2.4: PDFs of the longitudinal velocity-gradient for several Reynolds numbers, increasing in the direction of the arrow. All curves are normalized by their standard deviation. Reynolds numbers span $Re_L = 260$ to 3.5×10^6. Symbols indicate a Gaussian distribution for reference. Reproduced from [34].

ences across separations comparable to the integral scale ($r \sim l$) are approximately Gaussian, their distribution becomes markedly non-Gaussian as the separation decreases well below ($r \ll l$). In this regime, the flatness factor significantly exceeds the value of 3, indicating the presence of small-scale intermittency. Simultaneously, the skewness remains negative, reflecting the asymmetry of the velocity increment distribution induced by the forward energy cascade and the physical mechanisms of vortex stretching.

The velocity difference between two points separated by a distance r can be decomposed into the sum of increments over smaller subintervals. A direct application of the central limit theorem would suggest that the resulting PDF should approach a Gaussian distribution, provided these increments are sufficiently independent and possess comparable finite variances. While the independence assumption is reasonable when r is above the viscous cutoff, the requirement of comparable variances is generally violated in turbulent flows.

The observed non-Gaussianity indicates the presence of rare but intense velocity jumps. Within the dissipative range, these extreme events have been traced to thin, locally linear vortex structures(often referred to as worms) where the highest velocity gradients are concentrated [35, 36].

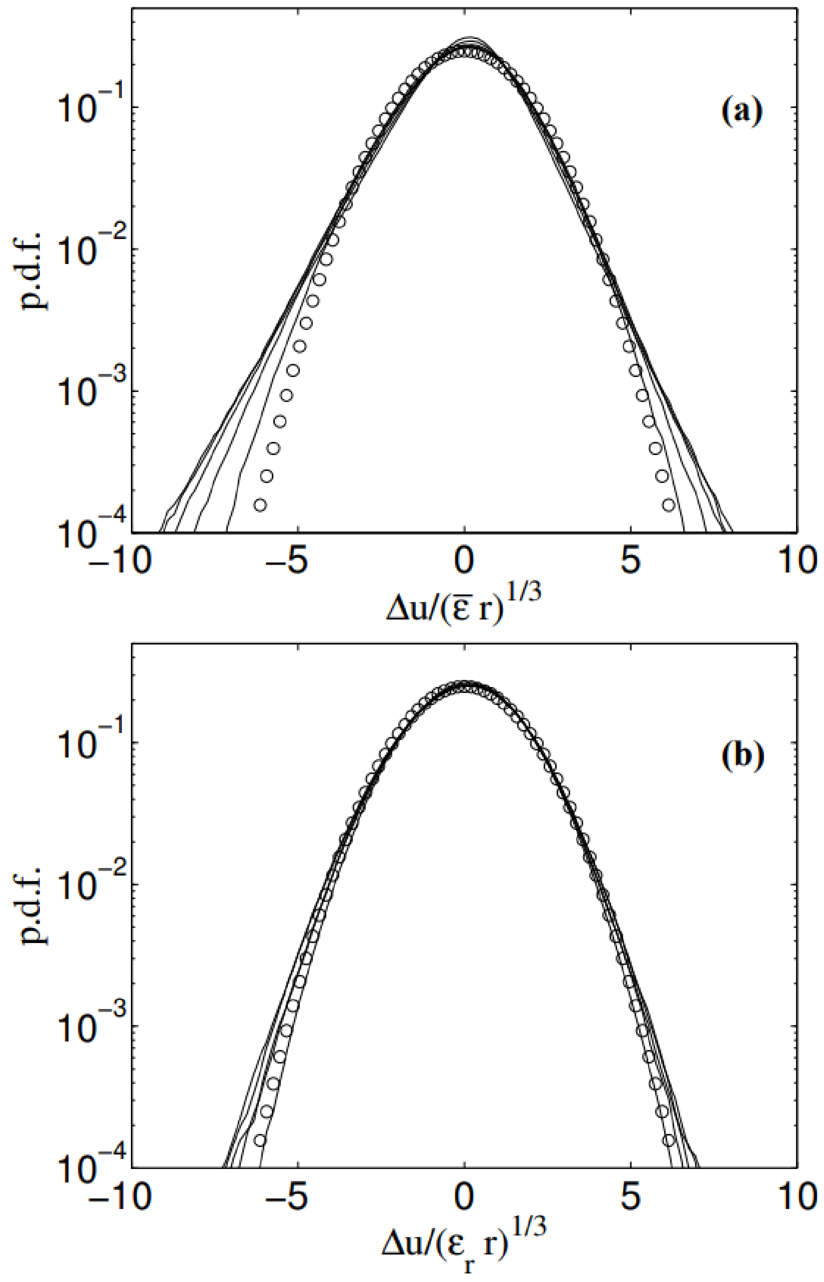

Figure 2.5: P.d.f.s of the velocity differences along the separation direction for scales within the inertial range. Separations range from $r/l = 0.02$ to 0.36, increasing by factors of 2, corresponding to $r/\eta = 180$ to 3000. The turbulence is nominally isotropic at a Reynolds number $Re_l = 10^5$. In the top panel, Δu is normalized by the global energy dissipation rate ε; distributions become broader as the separation decreases. In the bottom panel, Δu is scaled by the locally averaged dissipation over the separation interval. Reproduced from [34].

Consequently, the spatial distribution of velocity gradients is highly inhomogeneous. Enstrophy, defined as $\mathcal{E} = \frac{1}{2}|\boldsymbol{\omega}|^2$ (where $\boldsymbol{\omega}$ is the vorticity vector), tends to concentrate in small, intense regions that are sparsely distributed throughout the flow volume [37]. Moreover, the degree of this spatial intermittency increases with the Reynolds number, as the vorticity field becomes progressively more fragmented into localized, high-energy structures.

In addition, the classical formulation has conceptual limitations. The structure functions, which characterize the statistics of local velocity increments, could not consistently depend on a single global quantity such as the mean dissipation rate ε. Physically, a small separation r has no mechanism to "sense" a domain-averaged dissipation. To address this inconsistency, Kolmogorov introduced a refined similarity hypothesis (RSH) [38],

$$S_n(r) = C_n\,(\varepsilon_r\, r)^{n/3}, \tag{2.9}$$

where ε_r denotes the energy dissipation rate averaged over a volume of size $\mathcal{O}(r)$, typically taken as a ball centered at the midpoint of the interval. In this formulation, the scaling depends on the local variability of the dissipation field rather than on global mean. This refined similarity is supported by experimental data, as illustrated in Figure 2.5b.

Even under HIT conditions, the strict Kolmogorov $n/3$ scaling is not observed: measurements consistently yield $S_n(r) \sim r^{\zeta_n}$, where the anomalous exponents ζ_n deviate from the dimensional prediction $n/3$ [39]. These deviations are a direct consequence of the intermittent nature of the dissipation field ε, which exhibits strong spatial variability rather than remaining uniform. Consequently, the turbulent cascade is not a space-filling process; instead, intense dissipative events are clustered within a small fraction of the flow domain.

In a DHC, intermittency emerges naturally from the non-linear interaction between buoyancy-driven shear layers, thermal boundary layers, and the large-scale recirculation. Even when the flow is statistically stationary at the global level, localized regions can exhibit abrupt spikes in dissipation, enstrophy, or temperature gradients, highlighting the inhomogeneous distribution of turbulent activity within the cavity. Consequently, analyzing the behavior of structure functions is essential for characterizing the cascade of kinetic energy and temperature variance in a flow where buoyancy is the dominant driving mechanism. Their scale-dependent behavior reveals the degree of anisotropy, the transition towards local isotropy and the spatial distribution of coherent structures responsible for enhanced momentum and heat transport.

2.3.3 Turbulent Boundary Layer

In a DHC, the thermal and velocity boundary layers that develop along the isothermal vertical walls are regions governing global heat and momentum transport. The boundary-layer thickness, δ, is conventionally defined as the distance from the wall where the local mean temperature or velocity reaches its core value. At moderate to high Rayleigh numbers, the flow may exhibit transitional behavior, where laminar-like and turbulent boundary layers coexist along the vertical walls [40]. In the turbulent regime, both the thermal (δ_T) and velocity (δ_v) boundary layers undergo significant thinning as the Rayleigh number increases. This reduction in δ reflects the intensification of convective transport and the concentration of steep gradients near the solid boundaries.

The near-wall region is characterized by an intense shear layer induced by the wall shear stress:

$$\tau_w = \mu \left. \frac{\partial \overline{u}}{\partial n} \right|_{\text{wall}}, \tag{2.10}$$

where n denotes the coordinate normal to the wall. From this, the friction velocity u_τ is defined as:

$$u_\tau = \sqrt{\frac{\tau_w}{\rho}}. \tag{2.11}$$

Using this characteristic velocity scale, the friction Reynolds number Re_τ is calculated based on the boundary-layer thickness δ_v:

$$Re_\tau = \frac{u_\tau \delta_v}{\nu}. \tag{2.12}$$

The wall-normal coordinate and the mean longitudinal velocity can then be expressed in inner (wall) units as follows:

$$y^+ = \frac{u_\tau y}{\nu}, \quad u^+ = \frac{\overline{u}}{u_\tau}. \tag{2.13}$$

These dimensionless variables facilitate a comparison between buoyancy-driven boundary layers and classical law-of-the-wall profiles, providing a robust framework to evaluate the local turbulence state and the adequacy of the near-wall grid resolution. Although these scalings originated from canonical pressure-driven shear flows, at sufficiently high Reynolds numbers they remain a useful tool for characterizing near-wall dynamics in buoyancy-driven configurations, allowing the boundary layer to be decomposed into distinct dimensionless subregions:

- **Viscous sublayer** ($y^+ < 5$): A region where viscous stresses dominate and turbulence is strongly damped by the proximity of the solid boundary. Within this layer, the mean velocity varies linearly with the distance from the wall ($u^+ = y^+$).

- **Buffer layer** ($5 < y^+ < 30$): A transition zone where both viscous and turbulent (Reynolds) stresses are significant. This region is characterized by intense turbulent activity, where the production and dissipation of turbulent kinetic energy reach their peak values.
- **Logarithmic (or inertial) region** ($y^+ > 30$): A region where viscous effects become negligible compared to turbulent transport. In canonical flows, the velocity profile follows a logarithmic law, reflecting an approximate equilibrium between the production and dissipation of turbulence.

Figure 2.6 illustrates this classical boundary-layer behavior, while Table 2.2 summarizes the characteristic subregions, including the approximate y+ ranges and the governing velocity expressions.

In buoyancy-driven flows, heat transport within the thermal boundary layer is directly linked to the

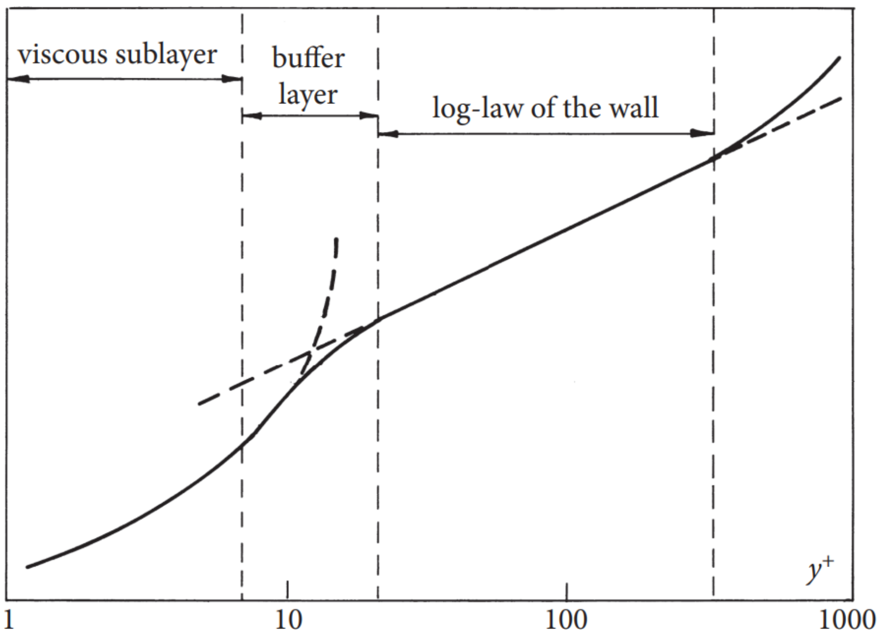

Figure 2.6: Plot of u_x/u_τ versus y^+ showing the log-law of the wall. Reproduced from [24].

Table 2.2: Main regions of the turbulent boundary layer and their characteristics [24], [41].

Region	Range in y^+	Governing Relation
Viscous sublayer	$y^+ \leq 5$	$u^+ = y^+$
Buffer layer	$5 \leq y^+ \leq 30$	No simple analytical form.
Logarithmic region	$y^+ \geq 30$	$u^+ = \frac{1}{\kappa}\ln(y^+) + B, \quad \kappa \approx 0.41, B \approx 5.0$

wall-normal temperature gradient. The local heat flux at the wall is governed by Fourier's law:

$$q_w = -k \left.\frac{\partial T}{\partial x}\right|_{\text{wall}} . \tag{2.14}$$

The local Nusselt number (Nu), representing the ratio between the actual wall heat flux and the purely conductive reference heat flux, is expressed as:

$$Nu = \frac{q_w}{\frac{k\Delta T}{W}} = -\left.\frac{\partial \bar{\theta}}{\partial x^*}\right|_{\text{wall}} , \tag{2.15}$$

where $\theta = (T - T_{\text{ref}})/\Delta T$ denotes the nondimensional temperature and $x^* = x/W$ is the nondimensional wall-normal coordinate. While heat transfer at the solid boundary is purely conductive, the gradient itself is determined by convective transport in the bulk. Consequently, buoyancy-driven convection leads to values of the Nusselt number greater than unity.

The total heat transfer across the cavity is quantified by the global Nusselt number ($\overline{Nu}$), obtained by integrating the local Nusselt number over the hot or cold walls:

$$\overline{Nu_h} = A_z \oiint_h -\left.\frac{\partial \theta}{\partial x^*}\right|_{x^*=0} ds, \tag{2.16}$$

$$\overline{Nu_c} = A_z \oiint_c -\left.\frac{\partial \theta}{\partial x^*}\right|_{x^*=\frac{1}{A_z}} ds. \tag{2.17}$$

As the Rayleigh number increases, the thermal boundary layer becomes thinner and more intermittent, leading to steeper near-wall temperature gradients and higher Nusselt numbers. Coherent structures ejected from the boundary layer play a dominant role in transporting heat into the core region, coupling the near-wall dynamics to the large-scale circulation and enhancing the overall heat transfer.

2.3.4 Coherent Structures

The turbulent flow within a DHC exhibits distinct spatial and temporal organization in the form of coherent structures. These structures play a key role in heat transfer enhancement and the modulation of local turbulence intensity. From a fundamental turbulence perspective, understanding the production mechanisms of TKE and its associated flow structures is critical [42], these processes sustain the turbulent motion against dissipative losses. The guiding principle is that randomness is not a property, but a methodological choice of what to ignore in the flow, and that a complete understanding of turbulence, including the possibility of control, requires that it be kept to a minimum [43].

Coherent structures can be defined as connected turbulent fluid mass with instantaneously phase-correlated vorticity over its spatial extent [44]. In a DHC, these structures emerge from the vertical boundary layers along the thermally active walls. Upstream of the detachment region, the flow remains laminar until periodic oscillations develop within the boundary layer, typically in the form of Tollmien–Schlichting-like waves, driven by the buoyancy-induced shear profile.. As these oscillations grow in amplitude, they trigger nonlinear interactions that lead to the breakdown of the boundary layer and the onset of turbulence.

The resulting large-scale vortical structures are ejected into the cavity core, enhancing mixing and promoting heat transfer, particularly, near the top and bottom walls. However, as the Rayleigh number increases, the kinetic energy associated with these large eddies cascades toward smaller scales, and their influence becomes confined closer to the vertical boundary layers. Furthermore, the transition point moves progressively upstream with increasing thermal forcing, reflecting the strengthening of the instability mechanisms and the thinning of the thermal and velocity boundary layers.

Although turbulence introduce non-linear interactions that disrupt structures clearly seen in laminar regimes, the organizing mechanisms responsible for their creation remain active. Consequently, these structures persist in transformed states and can be recovered through temporal averaging or by analyzing appropriate statistical correlations, such as the vertical turbulent heat flux $\overline{w'\theta'}$. An example of such structures is observed at $Ra = 10^8$ along the vertical junctions between the isothermal walls and the adiabatic rear or front faces. These edge vortices are confined to the corners and are typically attributed to Ekman- or Eckhaus-like vortices [19]. These 3D features are significant as they break the spanwise symmetry of the flow.

Chapter 3

Mathematical Model

3.1 Governing Equations

Flow inside a DHC can be described starting from the incompressible Navier–Stokes equations for velocity and temperature fields as shown in Equation 3.1.

$$
\begin{cases}
\dfrac{\partial u}{\partial x} + \dfrac{\partial v}{\partial y} + \dfrac{\partial w}{\partial z} = 0, \\
\dfrac{\partial u}{\partial t} + u\dfrac{\partial u}{\partial x} + v\dfrac{\partial u}{\partial y} + w\dfrac{\partial u}{\partial z} = -\dfrac{1}{\rho}\dfrac{\partial p}{\partial x} + \nu\left(\dfrac{\partial^2 u}{\partial x^2} + \dfrac{\partial^2 u}{\partial y^2} + \dfrac{\partial^2 u}{\partial z^2}\right), \\
\dfrac{\partial v}{\partial t} + u\dfrac{\partial v}{\partial x} + v\dfrac{\partial v}{\partial y} + w\dfrac{\partial v}{\partial z} = -\dfrac{1}{\rho}\dfrac{\partial p}{\partial y} + \nu\left(\dfrac{\partial^2 v}{\partial x^2} + \dfrac{\partial^2 v}{\partial y^2} + \dfrac{\partial^2 v}{\partial z^2}\right), \\
\dfrac{\partial w}{\partial t} + u\dfrac{\partial w}{\partial x} + v\dfrac{\partial w}{\partial y} + w\dfrac{\partial w}{\partial z} = -\dfrac{1}{\rho}\dfrac{\partial p}{\partial z} + \nu\left(\dfrac{\partial^2 w}{\partial x^2} + \dfrac{\partial^2 w}{\partial y^2} + \dfrac{\partial^2 w}{\partial z^2}\right) - g, \\
\dfrac{\partial T}{\partial t} + u\dfrac{\partial T}{\partial x} + v\dfrac{\partial T}{\partial y} + w\dfrac{\partial T}{\partial z} = \alpha\left(\dfrac{\partial^2 T}{\partial x^2} + \dfrac{\partial^2 T}{\partial y^2} + \dfrac{\partial^2 T}{\partial z^2}\right)
\end{cases}
\tag{3.1}
$$

These are the continuity, momentum, and energy equations, where u, v, and w represent the x-, y-, and z-components of the velocity field, respectively, and p and T denote the pressure and temperature fields. However, these elliptic partial differential equations are coupled together, highly nonlinear, and therefore extremely complex. Hence, approximations are used to simplify the problem. One of the main challenges in solving these equations arises from the spatial variation of fluid density caused by temperature or concentration gradients, as commonly occurs in natural convection. It is in this context that the Oberbeck-Boussinesq hypothesis is used.

3.1.1 The Oberbeck-Boussinesq Approximation

This approximation first neglects density variations except when they directly cause buoyant forces. Secondly, thermophysical properties are considered constant. Finally, heat from viscous dissipation is assumed negligible [45]. The density differences driving buoyancy, and thus the flow, are attributed primarily to temperature variations, so the influence of pressure on density (i.e. compressibility effects) is neglected. Furthermore, since these variations are assumed to be small, density is modeled as varying linearly with temperature:

$$\rho(T) = \rho_0 \left[1 - \beta(T - T_0)\right], \tag{3.2}$$

where ρ_0 is the reference density, i.e. the fluid density evaluated at the reference temperature, and β is the coefficient of volumetric thermal expansion at constant pressure $\beta = -\frac{1}{\rho}\left(\frac{\partial \rho}{\partial T}\right)_P$. Consequently, density variations are disregarded in the continuity and inertial terms, while their effect is retained exclusively in the gravitational body force term (i.e. when multiplied by g). The result is shown in Equation 3.3.

$$\begin{cases} \dfrac{\partial u}{\partial x} + \dfrac{\partial v}{\partial y} + \dfrac{\partial w}{\partial z} = 0, \\ \dfrac{\partial u}{\partial t} + u\dfrac{\partial u}{\partial x} + v\dfrac{\partial u}{\partial y} + w\dfrac{\partial u}{\partial z} = -\dfrac{1}{\rho_0}\dfrac{\partial p}{\partial x} + \nu\left(\dfrac{\partial^2 u}{\partial x^2} + \dfrac{\partial^2 u}{\partial y^2} + \dfrac{\partial^2 u}{\partial z^2}\right), \\ \dfrac{\partial v}{\partial t} + u\dfrac{\partial v}{\partial x} + v\dfrac{\partial v}{\partial y} + w\dfrac{\partial v}{\partial z} = -\dfrac{1}{\rho_0}\dfrac{\partial p}{\partial y} + \nu\left(\dfrac{\partial^2 v}{\partial x^2} + \dfrac{\partial^2 v}{\partial y^2} + \dfrac{\partial^2 v}{\partial z^2}\right), \\ \dfrac{\partial w}{\partial t} + u\dfrac{\partial w}{\partial x} + v\dfrac{\partial w}{\partial y} + w\dfrac{\partial w}{\partial z} = -\dfrac{1}{\rho_0}\dfrac{\partial}{\partial z}(p - \rho_0 g z) + \nu\left(\dfrac{\partial^2 w}{\partial x^2} + \dfrac{\partial^2 w}{\partial y^2} + \dfrac{\partial^2 w}{\partial z^2}\right) + \beta g(T - T_0), \\ \dfrac{\partial T}{\partial t} + u\dfrac{\partial T}{\partial x} + v\dfrac{\partial T}{\partial y} + w\dfrac{\partial T}{\partial z} = \alpha\left(\dfrac{\partial^2 T}{\partial x^2} + \dfrac{\partial^2 T}{\partial y^2} + \dfrac{\partial^2 T}{\partial z^2}\right) \end{cases} \tag{3.3}$$

It is useful to express the first term on the right-hand side of the z-momentum equation in this form when decomposing the pressure field into a dynamic component (associated with fluid motion) and a hydrostatic component (the pressure of the fluid at rest associated with height z)

$$p = p_s + p_d, \tag{3.4}$$

where the hydrostatic pressure is defined as

$$p_s = \rho_0 g z. \tag{3.5}$$

Substituting this decomposition into Equation 3.3, the expression can be reformulated as

$$\begin{cases} \dfrac{\partial u}{\partial x} + \dfrac{\partial v}{\partial y} + \dfrac{\partial w}{\partial z} = 0, \\ \dfrac{\partial u}{\partial t} + u\dfrac{\partial u}{\partial x} + v\dfrac{\partial u}{\partial y} + w\dfrac{\partial u}{\partial z} = -\dfrac{1}{\rho_0}\dfrac{\partial p_d}{\partial x} + \nu\left(\dfrac{\partial^2 u}{\partial x^2} + \dfrac{\partial^2 u}{\partial y^2} + \dfrac{\partial^2 u}{\partial z^2}\right), \\ \dfrac{\partial v}{\partial t} + u\dfrac{\partial v}{\partial x} + v\dfrac{\partial v}{\partial y} + w\dfrac{\partial v}{\partial z} = -\dfrac{1}{\rho_0}\dfrac{\partial p_d}{\partial y} + \nu\left(\dfrac{\partial^2 v}{\partial x^2} + \dfrac{\partial^2 v}{\partial y^2} + \dfrac{\partial^2 v}{\partial z^2}\right), \\ \dfrac{\partial w}{\partial t} + u\dfrac{\partial w}{\partial x} + v\dfrac{\partial w}{\partial y} + w\dfrac{\partial w}{\partial z} = -\dfrac{1}{\rho_0}\dfrac{\partial p_d}{\partial z} + \nu\left(\dfrac{\partial^2 w}{\partial x^2} + \dfrac{\partial^2 w}{\partial y^2} + \dfrac{\partial^2 w}{\partial z^2}\right) + \beta g(T - T_0), \\ \dfrac{\partial T}{\partial t} + u\dfrac{\partial T}{\partial x} + v\dfrac{\partial T}{\partial y} + w\dfrac{\partial T}{\partial z} = \alpha\left(\dfrac{\partial^2 T}{\partial x^2} + \dfrac{\partial^2 T}{\partial y^2} + \dfrac{\partial^2 T}{\partial z^2}\right). \end{cases} \tag{3.6}$$

Flow transition in square cavities has also been studied without the Boussinesq approximation [46]. these studies indicate that significant discrepancies in solutions appear in turbulent statistics and at elevated Ra. To ensure the validity of the approximation, the criterion $\beta(T - T_0) \ll 1$ must be satisfied. When this variation is no longer negligible, the standard Boussinesq approximations cease to be valid, and the full compressible Navier–Stokes equations must be considered [47].

This limitation becomes particularly restrictive in experimental studies, where it is necessary to increase the physical dimensions (H) in order to raise the Rayleigh number $\left(Ra = \frac{g\beta\Delta T H^3}{\alpha\nu}\right)$ and to maintain a sufficiently small thermal gradient (ΔT). As a result, only very small temperature gradients can be applied. In contrast, this restriction is easily bypassed in numerical studies by employing non-dimensional formulations.

3.1.2 Nondimensionalization

The equations can be non-dimensionalized to highlight the fundamental parameters that characterize the flow. The reference scales employed are summarized in Table 3.1. In particular, the convective velocity is obtained following Bejan's scale analysis for transient heating from the side [48].

Based on these, the corresponding nondimensional variables are defined as follows:

$$\begin{aligned} x^* &= \frac{x}{L_{\text{ref}}}, & y^* &= \frac{y}{L_{\text{ref}}}, & z^* &= \frac{z}{L_{\text{ref}}} \\ u^* &= \frac{u}{u_{\text{ref}}}, & v^* &= \frac{v}{u_{\text{ref}}}, & w^* &= \frac{w}{u_{\text{ref}}} \\ \theta &= \frac{T - T_0}{T_{\text{ref}}}, & p^* &= \frac{p_d}{p_{\text{ref}}}, & t^* &= \frac{t}{t_{\text{ref}}} \end{aligned} \tag{3.7}$$

Table 3.1: Reference quantities used for nondimensionalization.

Quantity	Symbol	Reference Scale	Expression
Length	L_{ref}	Cavity height	H
Temperature	T_{ref}	Temperature difference	ΔT
Velocity	u_{ref}	Convective velocity	$\dfrac{\alpha\sqrt{Ra}}{H}$
Time	t_{ref}	Convection time	$\dfrac{H^2}{\alpha\sqrt{Ra}}$
Pressure	p_{ref}	Based on u_{ref}	ρu_{ref}^2

Where $T_0 = \frac{T_h+T_c}{2}$ is the mean temperature in the cavity. Finally, substituting this into (3.6), the governing equations become:

$$\begin{cases} \dfrac{\partial u^*}{\partial x^*} + \dfrac{\partial v^*}{\partial y^*} + \dfrac{\partial w^*}{\partial z^*} = 0, \\ \dfrac{\partial u^*}{\partial t^*} + u^*\dfrac{\partial u^*}{\partial x^*} + v^*\dfrac{\partial u^*}{\partial y^*} + w^*\dfrac{\partial u^*}{\partial z^*} = -\dfrac{\partial p^*}{\partial x^*} + \dfrac{Pr}{\sqrt{Ra}}\left(\dfrac{\partial^2 u^*}{\partial x^{*2}} + \dfrac{\partial^2 u^*}{\partial y^{*2}} + \dfrac{\partial^2 u^*}{\partial z^{*2}}\right), \\ \dfrac{\partial v^*}{\partial t^*} + u^*\dfrac{\partial v^*}{\partial x^*} + v^*\dfrac{\partial v^*}{\partial y^*} + w^*\dfrac{\partial v^*}{\partial z^*} = -\dfrac{\partial p^*}{\partial y^*} + \dfrac{Pr}{\sqrt{Ra}}\left(\dfrac{\partial^2 v^*}{\partial x^{*2}} + \dfrac{\partial^2 v^*}{\partial y^{*2}} + \dfrac{\partial^2 v^*}{\partial z^{*2}}\right), \\ \dfrac{\partial w^*}{\partial t^*} + u^*\dfrac{\partial w^*}{\partial x^*} + v^*\dfrac{\partial w^*}{\partial y^*} + w^*\dfrac{\partial w^*}{\partial z^*} = -\dfrac{\partial p^*}{\partial z^*} + \dfrac{Pr}{\sqrt{Ra}}\left(\dfrac{\partial^2 w^*}{\partial x^{*2}} + \dfrac{\partial^2 w^*}{\partial y^{*2}} + \dfrac{\partial^2 w^*}{\partial z^{*2}}\right) + Pr\theta, \\ \dfrac{\partial \theta}{\partial t^*} + u^*\dfrac{\partial \theta}{\partial x^*} + v^*\dfrac{\partial \theta}{\partial y^*} + w^*\dfrac{\partial \theta}{\partial z^*} = \dfrac{1}{\sqrt{Ra}}\left(\dfrac{\partial^2 \theta}{\partial x^{*2}} + \dfrac{\partial^2 \theta}{\partial y^{*2}} + \dfrac{\partial^2 \theta}{\partial z^{*2}}\right), \end{cases} \tag{3.8}$$

The Prandtl number is defined as $Pr = \frac{\nu}{\alpha}$, and the Rayleigh number based on the cavity height is given by $Ra = \frac{g\beta\Delta T H^3}{\alpha\nu}$. The Prandtl number represents the ratio of momentum diffusivity (kinematic viscosity) to thermal diffusivity. Meanwhile, the Rayleigh number characterizes the relative importance of buoyancy-driven flow compared to viscous damping (Grashof number), scaled by the ratio between momentum and thermal diffusivity (Prandtl number). The solution of the governing equations depends only on the values of Ra and Pr. In this study, air is assumed to have $Pr = 0.71$, while Ra is the primary parameter varied. For brevity, the dimensionless variables x^*, y^*, z^*, u^*, v^*, w^*, and p^* will hereafter be written without the superscript asterisk, unless otherwise specified.

3.1.3 Boundary Conditions

The boundary conditions consist of uniform temperatures in the vertical isothermal walls

$$\theta(x=0,y,z)=\theta_h=0.5, \qquad \theta\left(x=\frac{1}{A_z},y,z\right)=\theta_c=-0.5 \tag{3.9}$$

and adiabatic (Neumann) boundary conditions for the top, bottom, front and rear adiabatic walls ($z=0$, $z=1$, $y=0$, and $y=\frac{A_y}{4}$, respectively)

$$\frac{\partial\theta}{\partial n}=0, \tag{3.10}$$

No-slip conditions are imposed on all six walls:

$$u=v=w=0. \tag{3.11}$$

The initial conditions consist of a linear conduction profile for temperature in the x-direction:

$$\theta(x,y,z)=\theta_h+\frac{\theta_c-\theta_h}{A_z}x=0.5-4x, \tag{3.12}$$

and zero velocity components in all directions.

$$u=v=w=0. \tag{3.13}$$

3.2 Turbulent Kinetic Energy

The average kinetic energy of the flow per unit mass can be expressed as

$$\frac{1}{2}\overline{u_i u_i}=\frac{1}{2}\overline{u_i}\,\overline{u_i}+\frac{1}{2}\overline{u_i' u_i'}=\overline{E}+e, \tag{3.14}$$

where $\overline{u_i}$ and u_i' are the mean and fluctuating velocity components in indicial notation, respectively. The first term on the right-hand side of Equation 3.14, $\overline{E}$, represents the energy of the mean flow. The second term, e, corresponds to the TKE and is an important measure of the intensity of turbulence:

$$e=\frac{1}{2}\overline{u_i' u_i'}=\frac{1}{2}\left[\overline{(u')^2}+\overline{(v')^2}+\overline{(w')^2}\right]. \tag{3.15}$$

Analyzing TKE is essential for understanding how turbulence extracts, transports, and dissipates energy within a flow. As a measure of the energy contained in velocity fluctuations, TKE characterizes the intensity of turbulent motions, highlighting regions where turbulence is generated by shear or buoyancy and where it decays through viscous dissipation. Investigating TKE provides insight into the multiscale structure of turbulence, linking large-scale coherent motions to small-scale dissipation via the energy cascade. Furthermore, TKE underpins many turbulence closure models and predictive frameworks. For an incompressible Newtonian fluid, the governing transport equation can be derived from the momentum equation (see Equation 3.8) written in indicial notation:

$$\frac{\partial u_i}{\partial t} + u_j \frac{\partial u_i}{\partial x_j} = -\frac{\partial p}{\partial x_i} + \frac{Pr}{\sqrt{Ra}} \frac{\partial^2 u_i}{\partial x_j \partial x_j} + Pr\theta\delta_{i3}, \tag{3.16}$$

where δ_{i3} is the Kronecker delta. Applying the Reynolds decomposition to separate mean and fluctuating parts (see Equation 2.4):

$$\frac{\partial(\overline{u_i} + u_i')}{\partial t} + (\overline{u_j} + u_j') \frac{\partial(\overline{u_i} + u_i')}{\partial x_j} = -\frac{\partial(\overline{p} + p')}{\partial x_i} + \frac{Pr}{\sqrt{Ra}} \frac{\partial^2(\overline{u_i} + u_i')}{\partial x_j \partial x_j} + Pr(\overline{\theta} + \theta')\delta_{i3}, \tag{3.17}$$

Subtracting the mean of Equation 3.16 and rearranging yields:

$$\frac{\partial u_i'}{\partial t} + \overline{u_j} \frac{\partial u_i'}{\partial x_j} + u_j' \frac{\partial \overline{u_i}}{\partial x_j} + u_j' \frac{\partial u_i'}{\partial x_j} = -\frac{\partial p'}{\partial x_i} + \frac{Pr}{\sqrt{Ra}} \frac{\partial^2 u_i'}{\partial x_j \partial x_j} + Pr\theta'\delta_{i3}, \tag{3.18}$$

By multiplying by u_i', averaging, and applying the incompressibility condition ($\partial u_i / \partial x_i = 0$), and rearranging, the non-dimensional TKE transport equation under the Boussinesq hypothesis is obtained:

$$\frac{\partial e}{\partial t} + \underbrace{\overline{u_j} \frac{\partial e}{\partial x_j}}_{\mathcal{C}} = \underbrace{-\overline{u_i' u_j'} \frac{\partial \overline{u_i}}{\partial x_j}}_{\mathcal{P}} - \underbrace{\frac{1}{2} \frac{\partial \overline{u_i' u_i' u_j'}}{\partial x_j}}_{\mathcal{T}} - \underbrace{\frac{\partial \overline{p' u_j'}}{\partial x_j}}_{\Pi} + \underbrace{\frac{Pr}{\sqrt{Ra}} \frac{\partial^2 e}{\partial x_j \partial x_j}}_{\mathcal{D}} - \underbrace{\frac{Pr}{\sqrt{Ra}} \overline{\frac{\partial u_i'}{\partial x_j} \frac{\partial u_i'}{\partial x_j}}}_{\varepsilon} + \underbrace{Pr\overline{u_i' \theta'}\delta_{i3}}_{\mathcal{G}}. \tag{3.19}$$

The local rate of change of TKE is governed by the combined contribution of all seven terms in the transport equation: $\mathcal{C}$ is the convection of TKE by the mean flow; $\mathcal{P}$ is the production of TKE by the mean shear; $\mathcal{T}$ represents turbulent transport; Π is the pressure diffusion; $\mathcal{D}$ is the viscous diffusion; ε is the viscous dissipation (conversion of TKE into heat at small scales); and $\mathcal{G}$ is the generation of TKE by buoyancy. Equation 3.19 can be reexpressed by grouping the transport terms (using incompressibility):

$$\frac{\partial e}{\partial t} = -\overline{u_i' u_j'}\frac{\partial \overline{u_i}}{\partial x_k} \underbrace{- \frac{\partial}{\partial x_j}\left[e\,\overline{u_j} + \underbrace{\overline{u_j'}\big(e + \overline{p'}\big) - \frac{\mathrm{Pr}}{\sqrt{Ra}}\frac{\partial e}{\partial x_j}}_{\text{Diffusion}}\right]}_{\text{Transfer of TKE}} - \frac{Pr}{\sqrt{Ra}}\overline{\frac{\partial u_i'}{\partial x_j}\frac{\partial u_i'}{\partial x_j}} + Pr\overline{u_i'\theta'}\delta_{i3}, \quad (3.20)$$

which can be symbolically written as:

$$\frac{\partial e}{\partial t} = \mathcal{P} + \mathcal{F} - \varepsilon + \mathcal{G}. \quad (3.21)$$

Where $\mathcal{F}$ is the total flux or transfer of TKE as shown in Equation 3.20. For homogeneous isotropic turbulence (HIT), the flow is statistically uniform in space, meaning spatial transport is negligible and the divergence of transport terms vanishes. Consequently, $\mathcal{F} = 0$. Moreover, if buoyancy is also neglected, only production ($\mathcal{P}$) and dissipation (ε) remain as the dominant source and sink terms. Under these conditions, Equation 3.20 reduces to

$$\frac{\partial e}{\partial t} = \mathcal{P} - \varepsilon. \quad (3.22)$$

Equation 3.22 is useful for local energy budgets (e.g., homogeneous shear flows, temporal evolution of homogeneous turbulence, or region-averaged budgets). However, if spatial transport, pressure–velocity correlation and buoyancy effects are significant (for example, in boundary layers, wakes, or strongly inhomogeneous flows), the full transport equation (3.21) must be retained.

3.3 Vorticity and Enstrophy Transport

The dynamics of small-scale turbulence are governed by the evolution of vorticity, $\boldsymbol{\omega} = \nabla \times \mathbf{u}$. Taking the curl of the nondimensional incompressible Navier–Stokes equations under the Boussinesq hypothesis yields the vorticity transport equation

$$\frac{D\boldsymbol{\omega}}{Dt} = (\boldsymbol{\omega}\cdot\nabla)\mathbf{u} + \frac{Pr}{\sqrt{Ra}}\nabla^2\boldsymbol{\omega} + Pr(\nabla\theta \times \hat{\boldsymbol{k}}), \quad (3.23)$$

The first term on the right-hand side of the equation represents the intensification (or diminution) of vorticity through the stretching (compression) of material elements. The second term corresponds to the viscous diffusion of vorticity due to molecular viscosity. The third term is the buoyancy-induced vorticity production term.

The velocity-gradient tensor $\mathbf{A} = \nabla \mathbf{u}$ can be split into a symmetric and a skew-symmetric component,

$$A_{ij} = \frac{\partial u_i}{\partial x_j} = \frac{1}{2}\left(\frac{\partial u_i}{\partial x_j} + \frac{\partial u_j}{\partial x_i}\right) + \frac{1}{2}\left(\frac{\partial u_i}{\partial x_j} - \frac{\partial u_j}{\partial x_i}\right) = S_{ij} + W_{ij} = S_{ij} + \frac{1}{2}\varepsilon_{ijk}\omega_k \tag{3.24}$$

where $\mathbf{S}$ is the rate-of-strain, $\mathbf{W}$ is the rate-of-rotation tensor, and ε_{ijk} is the Levi-Civita symbol. Multiplying the vorticity equation by the vorticity and dividing by two, gives the enstrophy transport equation:

$$\frac{D}{Dt}\left(\frac{1}{2}\omega^2\right) = \omega_i\omega_j S_{ij} + \frac{Pr}{\sqrt{Ra}}\omega_i \nabla^2 \omega_i + Pr\omega_i\varepsilon_{ijk}\partial_j\theta\delta_{k3}. \tag{3.25}$$

Here, the first term on the right-hand side is the production of enstrophy by vortex stretching and the second is the viscous contribution. Part of the essential dynamics of 3D turbulence is contained in the interaction between vorticity and the rate of strain tensor [29]. The viscous term can be rewritten as

$$\frac{Pr}{\sqrt{Ra}}\omega_i \nabla^2 \omega_i = \frac{Pr}{\sqrt{Ra}}\nabla^2\left(\frac{1}{2}\omega^2\right) - \frac{Pr}{\sqrt{Ra}}(\nabla\omega_i)\cdot(\nabla\omega_i) = \frac{Pr}{\sqrt{Ra}}\nabla^2\left(\frac{1}{2}\omega^2\right) - \frac{Pr}{\sqrt{Ra}}|\nabla\boldsymbol{\omega}|^2, \tag{3.26}$$

where $\frac{Pr}{\sqrt{Ra}}\nabla^2(\frac{1}{2}\omega^2)$ represents the diffusion of enstrophy (redistribution) and $-\nu|\nabla\boldsymbol{\omega}|^2$ the viscous destruction (irreversible sink).

Enstrophy is amplified when the production term is positive, which occurs when vorticity aligns with extensional strain (vortex stretching). While negative values of the production term are possible locally, its spatial average in 3D turbulence is positive, implying a net production of enstrophy. Although, compression may locally reduce ω^2, only viscosity provides irreversible dissipation. This balance explains the formation of thin, intense vortex tubes in turbulence, where stretching intensifies vorticity and viscous effects ultimately limit growth at the smallest scales. This mechanism is fundamental to the forward energy cascade, as vortex stretching enhances velocity gradients and promotes the transfer of kinetic energy toward smaller scales where viscous dissipation becomes effective. In contrast, in two-dimensional turbulence the production term vanishes identically because vorticity is normal to the velocity plane. As a result, enstrophy cannot be generated dynamically and is only dissipated by viscosity, a constraint that underlies the possibility of an inverse energy cascade in two-dimensional flows.

3.4 Velocity-Gradient Invariants

Flow invariants can be used to classify individual points within a flow field. By analyzing these invariants, it becomes possible to distinguish between regions dominated by intense rotational motion (vorticity-dominated) and regions dominated by deformation or stretching (strain-dominated) [24]. This classification provides a more precise and objective characterization of the local flow topology, allowing one to identify coherent structures, vortical cores, and high-strain layers, which are crucial for understanding turbulence dynamics and energy transfer mechanisms.

Considering again the decomposition of the velocity-gradient tensor A_{ij} into a symmetric and a skew-symmetric component, the rate-of-strain tensor can be diagonalized by aligning the axis coordinates to the principal strain axes:

$$A_{ij} = S_{ij} + W_{ij} = \begin{pmatrix} a & 0 & 0 \\ 0 & b & 0 \\ 0 & 0 & c \end{pmatrix} + \frac{1}{2}\begin{pmatrix} 0 & -\omega_c & \omega_b \\ \omega_c & 0 & -\omega_a \\ -\omega_b & \omega_a & 0 \end{pmatrix} \tag{3.27}$$

where a, b and c are the three principal rates of strain and ω_a, ω_b and ω_c are the components of the vorticity $\boldsymbol{\omega}$ along the principal axes. For a second-order tensor, there are 3 invariants directly related to its eigenvalues. If λ_1, λ_2 and λ_3 are the eigenvalues of $\mathbf{A}$, then

$$[\mathbf{A} - \lambda I]\,\mathbf{x} = 0, \tag{3.28}$$

where $\mathbf{x}$ is the eigenvector. The eigenvalues can be determined by solving the characteristic equation

$$\det[\mathbf{A} - \lambda I] = 0, \tag{3.29}$$

which gives rise to the equation

$$\begin{aligned} &\lambda^3 - \left(\frac{\partial u}{\partial x} + \frac{\partial v}{\partial y} + \frac{\partial w}{\partial z}\right)\lambda^2 + \left(\frac{\partial u}{\partial x}\frac{\partial v}{\partial y} + \frac{\partial u}{\partial x}\frac{\partial w}{\partial z} + \frac{\partial v}{\partial y}\frac{\partial w}{\partial z} - \frac{\partial v}{\partial z}\frac{\partial w}{\partial y} - \frac{\partial u}{\partial z}\frac{\partial w}{\partial x} - \frac{\partial v}{\partial x}\frac{\partial u}{\partial y}\right)\lambda \\ &+ \left(\frac{\partial u}{\partial x}\frac{\partial v}{\partial z}\frac{\partial w}{\partial y} + \frac{\partial u}{\partial z}\frac{\partial v}{\partial y}\frac{\partial w}{\partial x} + \frac{\partial u}{\partial y}\frac{\partial v}{\partial x}\frac{\partial w}{\partial z} - \frac{\partial u}{\partial x}\frac{\partial v}{\partial y}\frac{\partial w}{\partial z} - \frac{\partial u}{\partial y}\frac{\partial v}{\partial z}\frac{\partial w}{\partial x} - \frac{\partial u}{\partial z}\frac{\partial v}{\partial x}\frac{\partial w}{\partial y}\right) = 0, \end{aligned} \tag{3.30}$$

or

$$\lambda^3 + P\lambda^2 + Q\lambda + R = 0. \tag{3.31}$$

Since the eigenvalues are independent of the coordinate system, the coefficients P, Q and R are also invariants, referred to respectively as first, second, and third invariants of the velocity gradient. The properties of the roots of a cubic equation, along with elementary eigenvalue theory, tell us that if the eigenvalues are real then

$$\begin{cases} P = -\left(\lambda_1 + \lambda_2 + \lambda_3\right) = -\text{Trace}(A_{ij}) = -A_{ii} = -S_{ii} \\ Q = \lambda_1\lambda_2 + \lambda_2\lambda_3 + \lambda_3\lambda_1 = \frac{1}{2}P^2 - \frac{1}{2}A_{ij}A_{ji} \\ R = -\left(\lambda_1\lambda_2\lambda_3\right) = -\det(A_{ij}) = -\frac{1}{3}A_{ij}A_{jk}A_{ki}. \end{cases} \tag{3.32}$$

For incompressible flows, continuity enforces that

$$P = -A_{ii} = -S_{ii} = -\left(\frac{\partial u}{\partial x} + \frac{\partial v}{\partial y} + \frac{\partial w}{\partial z}\right) = 0, \tag{3.33}$$

Consequently, the remaining invariants can be expressed in terms of the strain and rotation decomposition as:

$$Q = -\frac{1}{2}A_{ij}A_{ji} = -\frac{1}{2}S_{ij}S_{ij} + \frac{1}{4}\omega_i\omega_i, \tag{3.34}$$

$$R = -\frac{1}{3}A_{ij}A_{jk}A_{ki} = -\frac{1}{3}\left(S_{ij}S_{jk}S_{ki} + \frac{3}{4}\omega_i\omega_j S_{ij}\right). \tag{3.35}$$

If the vorticity is locally zero, the invariants reduce to:

$$Q_S = -\frac{1}{2}S_{ij}S_{ji} \tag{3.36}$$

$$R_S = -\frac{1}{3}S_{ij}S_{jk}S_{ki}. \tag{3.37}$$

Conversely, when the strain is locally zero, the invariants reduce to:

$$Q_W = \frac{1}{4}\omega_i\omega_i \tag{3.38}$$

$$R_W = 0. \tag{3.39}$$

The second invariant, $Q = Q_S + Q_W$, measures the relative intensity between strain (S) and vorticity (W). Large negative values ($Q < 0$) indicate regions of strong strain and viscous dissipation, while large positive values ($Q > 0$) mark regions of intense enstrophy. In isotropic turbulence, intense values of viscous dissipation tend to be concentrated in structures with the form of sheets or ribbons. Conversely, regions of intense enstrophy tend to be concentrated in tubelike structures in many turbulent flows such as isotropic turbulence, mixing layers and jets.

On the other hand, $R_S = -\dfrac{1}{3}S_{ij}S_{jk}S_{ki}$, is proportional to the strain production $S_{ij}S_{jk}S_{ki}$. A positive value of R_S is associated with the production of strain product and thus of viscous dissipation (sheet-like structures), whereas $R_S < 0$ implies a destruction of strain product (tube-like structures). The invariants can also be expressed using the principal rates of strain (the eigenvalues of S):

$$Q = \frac{1}{4}\omega_i\omega_i - \frac{1}{2}(a^2 + b^2 + c^2) \tag{3.40}$$

$$R = -\left(\frac{1}{4}\omega_i\omega_j S_{ij} + abc\right). \tag{3.41}$$

Where $a > b > c$. Consider first the case where Q is large and positive. This requires the enstrophy term $\frac{1}{4}\omega_i\omega_i$ to dominate, implying that rotation is locally strong and the strain magnitude $(a^2+b^2+c^2)$ is weak. In this limit, the cubic product abc is small compared with $\frac{1}{4}\omega_i\omega_j S_{ij}$, so the latter term controls the sign of R. A negative R then corresponds to generation of enstrophy by local vortex stretching ("worm" structures), whereas a positive R corresponds to vortex compression. If instead Q is large and negative, the strain term $-\frac{1}{2}(a^2 + b^2 + c^2)$ dominates, indicating a strain-dominated region. In this case, the rotational contribution $\frac{1}{4}\omega_i\omega_j S_{ij}$ becomes negligible compared with the cubic product abc, so $R \approx abc$. Because the strain-rate tensor is traceless $(a + b + c = 0)$, the sign of abc distinguishes two different strain topologies. A positive abc (resulting in a negative R) occurs when one eigenvalue is positive and the other two are negative, which corresponds to axial strain (one extensional direction and two compressive directions). Conversely, a negative abc (positive R) implies two positive eigenvalues and one negative eigenvalue, corresponding to biaxial strain (two extensional directions and one compressive direction).

A compact and widely used representation of the local flow topology is obtained by considering the joint distribution of the second and third invariants of the velocity-gradient tensor in the so-called Q–R plane. In many turbulent flows, the joint probability density function (PDF) of Q and R exhibits a characteristic asymmetric "teardrop" shape, as shown in Figure 3.1 for Rayleigh-Bénard convection. This distribution has been observed consistently across experiments and direct numerical simulations [50], reflecting the preferential organization of the velocity-gradient tensor into specific flow topologies rather than a uniform distribution of strain and rotation.

The distribution is skewed toward the quadrant where $Q > 0$ and $R < 0$, indicating a predominance of rotational structures undergoing vortex stretching, which is a fundamental mechanism sustaining turbulence. The elongated tail of the distribution, extending into the quadrant where $Q < 0$ and

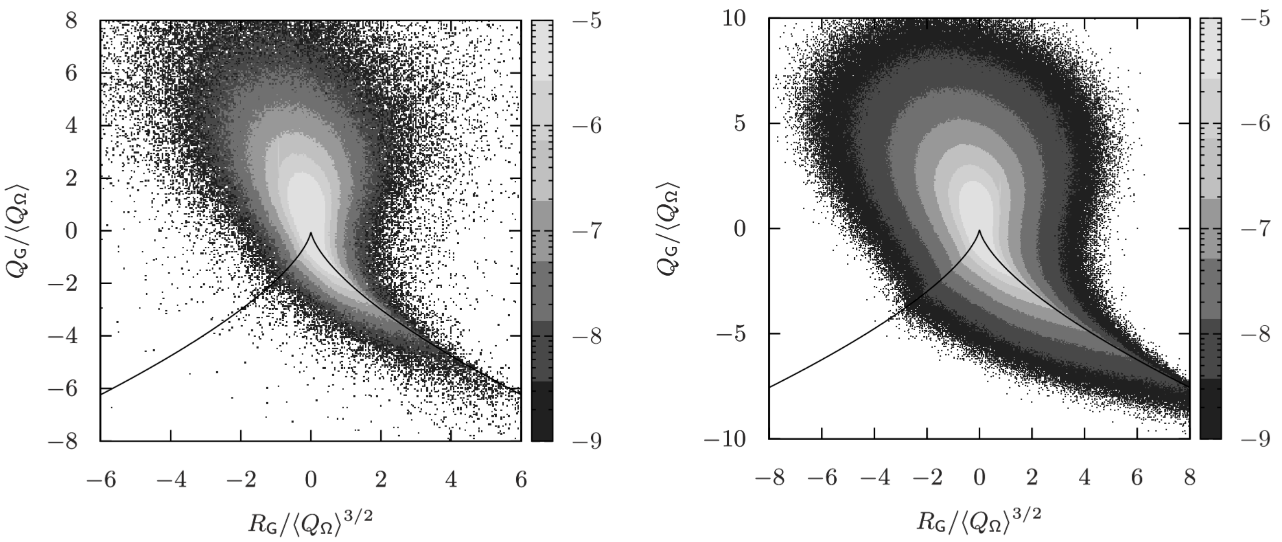

Figure 3.1: Joint probability density function (PDF) of the Q and R invariants (denoted as Q_G and R_G in the figure) normalized by Q_w (denoted as Q_Ω in the figure) on a logarithmic scale for Rayleigh-Bénard convection. Panels show results through the bulk at (a) $Ra = 10^8$ and (b) $Ra = 10^{10}$. The solid black line indicates the null-discriminant curve, $D = (27/4)R^2 + Q^3 = 0$. Reproduced from [49].

$R > 0$, corresponds to rare but intense strain-dominated events associated with sheet-like dissipative structures (biaxial strain). Although these regions occupy a small fraction of the flow volume, they contribute significantly to viscous dissipation, reflecting the intermittent nature of turbulence. The discriminant of the characteristic polynomial $D = (27/4)R^2 + Q^3$, separates regions with three real eigenvalues $(D < 0)$ from regions with one real and a pair of complex-conjugate eigenvalues $(D > 0)$, also distinguishing between pure straining motion and locally spiraling (vortical) motion, respectively.

It is important to note that these invariants not only classify the local flow topology but also admit a geometrical interpretation linked to vorticity–strain interactions. In particular, the enstrophy production term corresponds to the projection of the vorticity vector onto the vortex-stretching vector $\mathbf{S}\omega$

$$\omega_i \omega_j S_{ij} = \boldsymbol{\omega} \cdot \mathbf{S}\boldsymbol{\omega} = \omega^2 \sum_{i=1}^{3} \lambda_i \cos^2(\boldsymbol{\omega}, \boldsymbol{e}_i), \tag{3.42}$$

where λ_i are the eigenvalues of the rate-of-strain tensor and $\boldsymbol{e}_i$ are its corresponding eigenvectors (the principal strain axes). It follows that enstrophy production depends explicitly on the alignment between vorticity and the strain eigenframe, as well as on the relative magnitudes of the strain eigenvalues. Such geometrical features are fundamental to three-dimensional turbulence, where preferential alignment with extensional strain governs vortex stretching and underpins the small-scale amplification processes reflected in the observed Q–R statistics.

Chapter 4

Simulation Methodology

4.1 Nek5000: Spectral Element Code

The computational fluid dynamics open-source program `Nek5000` is used to solve the governing equations. Developed and maintained by Fischer et al. [51] at the Argonne National Laboratory, `Nek5000` is a Navier–Stokes solver based on the spectral element method (SEM) originally by Patera [52]. This method merges the advantages of high-order spectral methods with finite element methods, offering known accuracy, favourable dispersion properties, and efficient parallelization.

The computational domain is partitioned into $E_x \times E_y \times E_z$ non-overlapping hexahedral spectral elements. In the streamwise and spanwise directions, a uniform element distribution is chosen. Conversely, near the isothermal walls, the elements in the wall-normal direction (x) are clustered using a hyperbolic tangent function:

$$(E_x)_j = \frac{1}{8}\left(1 + \frac{\tanh\left[\gamma_x \frac{2(j-1)}{E_x} - 1\right]}{\tanh \gamma_x}\right), \tag{4.1}$$

with γ_x is the concentration parameter, fixed at 4.5. This clustering ensures that the high-gradient regions and turbulent structures near the walls are well resolved.

The governing equations are reformulated in the weak form using a Galerkin projection for discretization for every spectral element, with test and trial functions selected from distinct polynomial spaces. Specifically, a $P_N - P_{N-2}$ formulation is utilized: the velocity and temperature fields are approximated using Nth-degree Lagrange interpolants defined at Gauss–Lobatto–Legendre (GLL) quadrature points, while the pressure field is approximated with $(N-2)$th-degree Lagrange interpolants defined at Gauss–Legendre quadrature points. Time-derivative terms are discretized via the third-order backward differentiation formula. Nonlinear convective terms are calculated explicitly using a third-order extrapolation scheme, while linear terms are treated implicitly. This high-order splitting approach results in a Poisson equation for pressure and Helmholtz equations for temperature and velocity components. The resulting linear systems are solved using the generalized minimal residual method (GMRES) with a convergence tolerance set to 10^{-8}. A detailed description of the numerical method is provided in Appendix A.

The computations are performed on four workstations, each equipped with 44 processors and 256 GB of RAM. Remote access to the computational resources is provided through the Secure Shell (SSH) protocol and a VPN connection. The simulations, carried out using the spectral element code `Nek5000`, achieve exponential convergence in space and third-order accuracy in time at a relatively low computational cost. In addition, the use of previously computed solutions as initial conditions significantly reduces the overall computation time by accelerating convergence. Typical simulations at Rayleigh numbers of order $Ra \approx 10^8$ require approximately two weeks of computation, while fully turbulent cases demand up to two months of runtime.

4.2 Simulation Parameters

Table 4.1 summarizes the simulation parameters, for the transitional and turbulent cases, including the number of spectral elements E in each direction, the order of the polynomials N, the time step Δt, and the time used to average properties and the total simulation time.

Figure 4.1 shows the top portion of the mesh, colored by the time-averaged temperature on the plane $y = 0.125$, where the distribution of elements is clearly visible, with a higher concentration near the walls. The time step of the simulations is fixed in order to resolve all the scales of the flow, while respecting the Courant-Friedrichs-Lewy condition. In particular, a CFL of 0.25 is used to ensure stability during the simulation until the flow reaches the converged (statistically steady) state. For computationally intensive simulations, initial conditions are mapped from a previous state at a lower

Table 4.1: Physical and simulation parameters.

Case	Ra	E_x	E_y	E_z	N	Δt	Average time	Total time
A	10^8	20	20	50	10	10^{-3}	50	150
B	10^{10}	28	28	100	10	5×10^{-4}	200	300

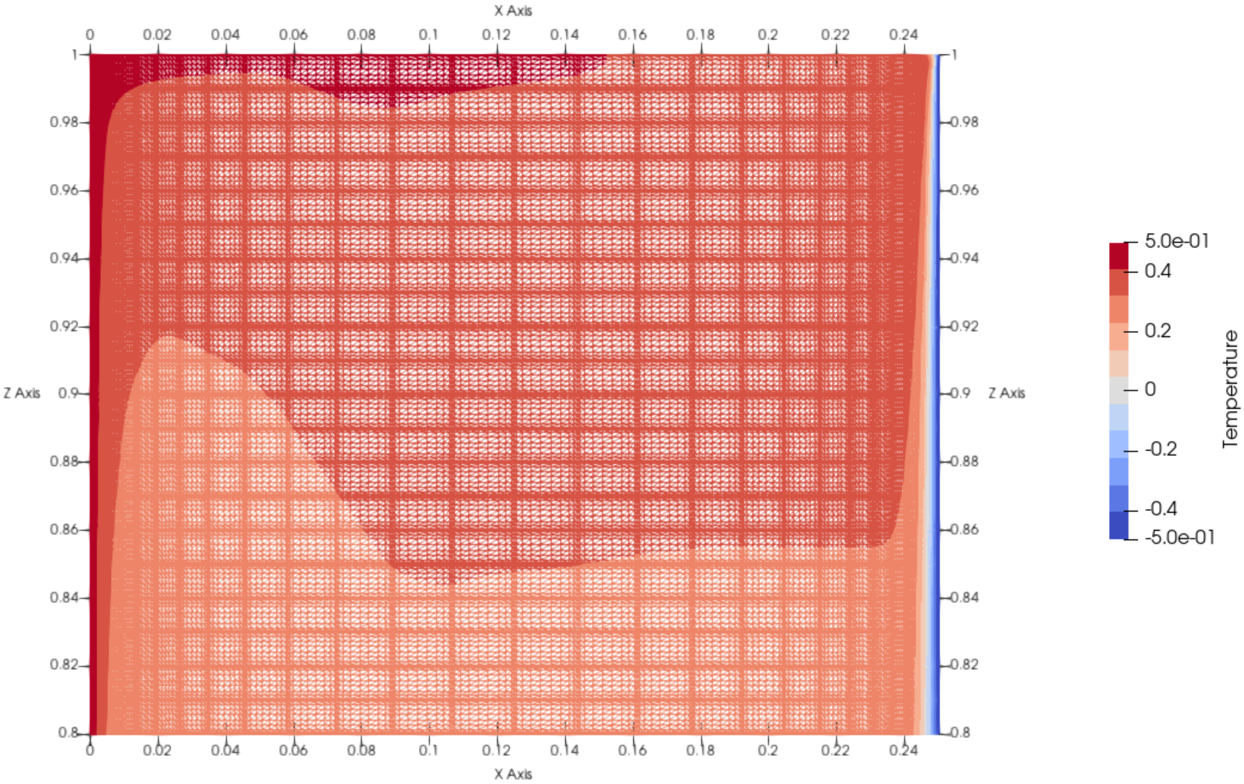

Figure 4.1: Top portion ($z \leq 0.8$) of the computational mesh, colored by the time-average temperature field on the plane $y = 0.125$.

Rayleigh number.

In turbulent regions, since $Pr < 1$, the temperature microscale is larger than the velocity microscale; thus, the smallest resolved length scale is required to be the Kolmogorov length scale η. Given that $\eta = \left(\frac{\nu^3}{\varepsilon}\right)^{1/4}$, this length scale becomes smaller with increasing dissipation and increasing Ra. As expected, with Δx representing the spacing between mesh points, $\frac{\Delta x}{\eta}$ peaks along z are observed in the shear layer zone where ε values are highest. Furthermore, to accurately resolve the near-wall region, the first off-wall grid point must be placed sufficiently close to the wall to resolve the steep velocity gradients characteristic of the viscous sublayer, ensuring $\Delta y_w^+ \lesssim 1$. This is achieved by placing at least 2 points inside the sublayer. Moreover, a sufficient number of points must be clustered within the buffer layer ($y^+ \leq 50$), the most anisotropic zone of wall-bounded turbulence and the location of intense turbulent activity. This clustering is achieved through hyperbolic-tangent mapping of the spectral elements. In the outer region, where turbulence approaches local isotropy, the grid spacing scales with the local Kolmogorov length scale to ensure that the smallest dynamically relevant eddies are resolved. These criteria collectively ensure that the mesh captures the full multiscale nature

Table 4.2: Maximum and minimum mesh spacing and their locations.

Direction	$\Delta_{\max}$	Location	$\Delta_{\min}$	Location
x	3.342×10^{-3}	$x = 0.1267$	6.904×10^{-5}	$x = 0.2484$
y	1.653×10^{-3}	$y = 0.1958$	4.023×10^{-4}	$y = 0.1300$
z	1.836×10^{-3}	$z = 0.3509$	4.470×10^{-4}	$z = 0.3778$

of near-wall turbulence with sufficient fidelity for DNS [53]. Table 4.2 presents the minimum and maximum grid spacings, along with their corresponding locations within the mesh, for the $Ra = 10^{10}$ case.

On the other hand, to ensure that the temporal resolution accurately captures the smallest dynamical features of the flow, the sampling frequency must exceed twice the highest physical frequency present, by analogy with the Nyquist criterion. In turbulent flows, this upper bound is associated with the Kolmogorov or viscous time scale, which dictates the fastest fluctuations in the system. Consequently, the numerical time step must correspond to a sampling frequency substantially larger than this limit. In practice, it is advisable to operate at more than two times the Kolmogorov frequency to guarantee adequate temporal resolution, minimize aliasing, and ensure that the numerical scheme can reconstruct the relevant flow dynamics without loss of information.

To analyze the temporal dynamics of the flow, a set of monitoring points is employed to record the time evolution of the temperature and velocity components at every time step. These probes allow for a detailed examination of local signals within and near the boundary layer adjacent to the hot wall. At each selected location, the three velocity components and temperature are sampled. Monitoring points are defined as all possible combinations of the coordinate values presented in Table 4.3.

4.3 Validation

Validation of the mesh was previously performed by Gers et al. for the non-turbulent cases [19]. The spatial resolution was selected using the mesh reported by Trias et al. [11] as a guideline. A mesh

Table 4.3: Definition of monitoring point coordinates.

Coordinate	Minimum	Maximum	Spacing
x	0.0005	0.125	0.0005
y	0.125	0.1875	0.0625
z	0.05	0.95	0.1

convergence study was performed to determine the polynomial order, resulting in higher resolution than that of Trias et al. [11]. For the turbulent case, an a posteriori verification is carried out by examining the boundary-layer resolution and confirming that both the viscous sublayer and the Kolmogorov scale are adequately captured. The physical consistency of the results is further assessed by exploiting the inherent symmetries of the DHC flow fields, which provide a robust qualitative validation criterion. In this context, the dominant frequencies of the flow can be analyzed to verify whether the spectral content aligns with the expected dynamical behavior.

4.4 Data Analysis

4.4.1 Critical Rayleigh Determination

Since the system undergoes a supercritical Hopf bifurcation, the critical Rayleigh number (Ra_c) can be determined using the linear relationship between the amplitude (A) of the monoperiodic fluctuating fields and the Rayleigh number (Ra) [54]:

$$A \propto \sqrt{Ra - Ra_c}, \quad Ra > Ra_c. \tag{4.2}$$

A linear relationship is obtained by squaring the amplitude:

$$A^2 \propto Ra - Ra_c, \quad Ra > Ra_c. \tag{4.3}$$

The temperature field is selected for this analysis, thus the amplitude of the fluctuating field is proportional to the temperature variance:

$$A^2(\theta) \propto \overline{(\theta - \overline{\theta})^2} = \overline{\theta'\theta'} \propto Ra - Ra_c, \quad Ra > Ra_c. \tag{4.4}$$

Simulations are first conducted starting at $Ra = 1 \times 10^8$, and the Rayleigh number is gradually increased until significant temperature variance, $\overline{\theta'\theta'}$, is observed. The region of maximum fluctuations is identified by visualizing the temperature field, and the signal from the closest monitoring point is examined. Next, the variance of the signal is calculated after it reaches a stable monoperiodic state. This procedure is repeated for various Rayleigh numbers, and the corresponding signal amplitudes are recorded. A plot of temperature variance versus Rayleigh number is then used to demonstrate the linear dependence, allowing for extrapolation to determine the transitional Rayleigh number Ra_c.

4.4.2 Spectral Analysis of Monoperiodic Signals

The frequency spectrum of temperature or velocity signals at a single monitoring point is analyzed to gain insight into the dominant dynamical mechanisms of the flow. For each Rayleigh number, a two-column data file is processed, where the first column corresponds to time t and the second column to the measured signal $s(t)$. To avoid contamination by initial transients and to focus on the established oscillatory dynamics, the analysis is performed over a prescribed time interval $t \in [t_{\min}, t_{\max}]$ (see Table 4.1). The sampling interval is denoted by Δt, the corresponding sampling frequency by $F_s = 1/\Delta t$, and the total number of samples within the selected time window by N. The discrete Fourier transform (DFT) of the signal is computed using the fast Fourier transform (FFT) to obtain its frequency spectrum:

$$S_k = \sum_{n=0}^{N-1} s_n \exp\left(-i2\pi \frac{kn}{N}\right), \qquad k = 0, \ldots, N-1. \tag{4.5}$$

The corresponding frequency grid is given by

$$f_k = \frac{k}{N} F_s. \tag{4.6}$$

The analysis is restricted to the one-sided spectrum ($0 \leq f \leq F_s/2$). The dominant frequency of the signal, which in the monoperiodic regime corresponds to the natural oscillation frequency, is identified as the spectral peak with the maximum magnitude excluding the zero-frequency component,

$$k^\star = \arg\max_{k \geq 1} |S_k|. \tag{4.7}$$

Since the FFT provides spectral values on a discrete frequency grid with resolution $\Delta f = F_s/N$, the peak location is refined using parabolic interpolation based on the three spectral magnitudes surrounding the maximum, namely $|S_{k^\star-1}|$, $|S_{k^\star}|$, and $|S_{k^\star+1}|$. Defining

$$\alpha = |S_{k^\star-1}|, \qquad \beta = |S_{k^\star}|, \qquad \gamma = |S_{k^\star+1}|, \tag{4.8}$$

the fractional-bin shift p is estimated as

$$p = \frac{1}{2} \frac{\alpha - \gamma}{\alpha - 2\beta + \gamma}, \tag{4.9}$$

which yields the refined dominant frequency:

$$f_{\mathrm{nat}} \approx (k^{\star} + p)\,\frac{F_s}{N}. \tag{4.10}$$

Finally, the corresponding angular frequency is computed as $\omega_{\mathrm{nat}} = 2\pi f_{\mathrm{nat}}$.

4.4.3 Turbulent Boundary Layer

Since the vertical boundary layer constitutes the primary region where turbulence mechanisms develop within the DHC, its associated parameters are essential for understanding the flow dynamics. First, the friction velocity w_τ is computed from the wall-normal gradient of the tangential velocity at the wall. Next, the velocity boundary layer thickness is analyzed using three characteristic definitions:

- δ_1: The wall-normal distance at which the vertical velocity reaches its maximum value.
- δ_2: An integral thickness defined as [59]

$$\delta_3 = \int_0^{\infty} \frac{\overline{w}}{\overline{w}_{\max}}\,dx. \tag{4.11}$$

- δ_3: The wall-normal distance at which the vertical velocity changes sign [60].

The friction Reynolds number Re_τ is then evaluated for each boundary-layer thickness definition. Finally, the normalized velocity w^+ and the normalized wall-normal coordinate x^+ are analyzed to verify that the viscous sublayer ($x^+ < 1$) is adequately resolved, with at least two grid points located within this region.

4.4.4 Heat Transfer

Heat transfer in the DHC is analyzed through the terms present in the energy equation (see Equation 3.8). The advective term $\mathbf{u} \cdot \nabla\theta$ represents the convective transport of thermal energy, which can be interpreted as the divergence of the enthalpy flux $\mathbf{u}\theta$. Conversely, the diffusive term $\frac{1}{\sqrt{Ra}}\nabla^2\theta$ accounts for conductive heat transfer driven by temperature gradients. The total nondimensional heat flux within the fluid domain can thus be expressed as

$$\mathbf{q} = \mathbf{u}\theta - \frac{1}{\sqrt{Ra}}\nabla\theta, \tag{4.12}$$

reflecting the combined action of convective enthalpy transport in the bulk and conductive diffusion throughout the domain. At the thermally active walls, the no-slip and impermeability conditions suppress convective transport, such that heat transfer occurs purely by conduction. However, convective transport within the cavity bulk strongly influences the near-wall temperature gradients, thereby enhancing the wall heat flux and leading to Nusselt numbers greater than unity.

4.4.5 Turbulent Statistics

Turbulent statistical quantities are evaluated at fixed intervals of 50 nondimensional time units to characterize the mean turbulent behavior of the flow. The analysis is performed using a toolbox developed by Vinuesa et al. [55] for high-fidelity spectral-element simulations. At each sampling instant, the velocity and temperature fields are used to compute the corresponding averaged statistics, including the mean velocity components and the Reynolds-stress tensor, as well as turbulent kinetic energy and Reynolds-stress budgets. Finally, a post-processing tool is utilized to average all files and to obtain more complete fields.

Additional routines are implemented to compute the mean fields, temperature gradients and variance, correlations between the velocity components and temperature, and the mean Nusselt number with its associated variance.

4.4.6 Velocity-Gradient Invariants

To identify coherent structures and analyze their dynamics, an approach based on the invariants of the velocity-gradient tensor is employed. A region of interest (ROI) is first defined based on the turbulent statistics of the flow. Within this region, the velocity-gradient tensor is computed at every grid point and stored every 100 time steps. The resulting data are post-processed to obtain the symmetric $\mathbf{S}$ (strain-rate) and antisymmetric $\mathbf{W}$ (rotation-rate) components of the tensor, as well as the corresponding invariants P, Q, R, Q_S, Q_W, and R_S. The statistical behavior of these invariants is examined through their joint probability density function (PDF). The normalization proposed by Ooi et al. [56] is adopted, allowing direct comparison with canonical results reported in the literature. The structure of the PDF provides insight into the local flow topology and the balance between strain-dominated and rotation-dominated dynamics. In addition, the alignment between vorticity and the vortex-stretching vector is analyzed. Finally, several vortex identification criteria are evaluated to further characterize coherent structures within the flow [5].

Enstrophy measures the intensity of rotational motion and is primarily associated with small-scale turbulent activity:

$$\mathcal{E} = \frac{1}{2}|\boldsymbol{\omega}|^2 = \frac{1}{2}|\nabla \times \mathbf{u}|^2. \tag{4.13}$$

The Q-criterion separates zones where rotation dominates over strain, which are therefore associated with vortical structures:

$$Q = \frac{1}{2}\left(|\mathbf{W}|^2 - |\mathbf{S}|^2\right). \tag{4.14}$$

The λ_2 criterion identifies vortical regions as those where negative values of the second-largest eigenvalue of the tensor M are found:

$$\mathbf{M} = \mathbf{S}^2 + \mathbf{W}^2. \tag{4.15}$$

Finally, the Ω-criterion provides a normalized measure of the relative importance of rotation with respect to strain [57]:

$$\Omega = \frac{|\mathbf{W}|}{|\mathbf{W}| + |\mathbf{S}| + \varepsilon}, \tag{4.16}$$

where ε is a small positive value used to avoid numerical noise.

4.4.7 Statistical Analysis of Turbulence

An open-source package developed by Fuchs et al. [58] is employed to carry out the statistical analysis of turbulence. The software, implemented in MATLAB, provides routines for estimating a wide range of canonical turbulence metrics, including spectral density, turbulence intensity, integral length scale, Taylor microscale, Kolmogorov scale, and dissipation rate. It also enables the computation of velocity increments, structure functions of various orders, and their corresponding scaling exponents.

From the vertical component of the momentum equation (Equation 3.8), it is evident that temperature fluctuations act directly on vertical velocity fluctuations through the buoyancy term. Consequently, turbulent kinetic energy is injected preferentially into the vertical velocity component, making $\overline{w'w'}$ the most influential contribution to the development of turbulent motion in the DHC. For this reason, the vertical component of the turbulent kinetic energy is employed as the diagnostic quantity to identify regions of intense turbulent activity. In particular, $\overline{w'w'}$ is inspected on the $y = 0.125$ and $y = 0.1875$ planes to locate zones exhibiting the highest velocity fluctuations. In addition, the center of the cavity is analyzed separately, as it represents the stratified core region where buoyancy-driven turbulence redistributes energy and where anisotropic effects are most prominent.

Chapter 5

Results and Analysis

5.1 Flow Instabilities and Transition to Turbulence

5.1.1 Fluctuations Analysis

Figure 5.1 shows the time-averaged temperature variance for $Ra = 2.75 \times 10^8$, $Ra = 2.85 \times 10^8$, and $Ra = 3.2 \times 10^8$. Only the region $z > 0.7$ is shown, given the symmetry of the flow field and the negligible fluctuations in the central region of the cavity. The largest fluctuations occur near the monitoring point $A(x, y, z) = (0.025,\ 0.125,\ 0.95)$, which is used for a detailed analysis of the temperature signal. The point $B(x, y, z) = (0.025,\ 0.1875,\ 0.95)$ is also utilized to highlight depth-induced differences. Although the location of maximum fluctuations is expected to shift upstream as Ra increases, the range of Rayleigh numbers considered here is sufficiently narrow that no discernible displacement is observed across the values analyzed. Therefore, the same monitoring points are maintained for all cases.

It is also important to note that the temperature variance plotted corresponds to an average over the entire simulation time. As such, it includes strong fluctuations generated during the initial transient stage, which are not representative of the fully developed monoperiodic state. Consequently, the reported variance does not reflect the intrinsic steady-state values. Nevertheless, by examining only the converged portion of the simulation, it was verified that the spatial distribution of the temperature variance remains unchanged and that only its magnitude varies.

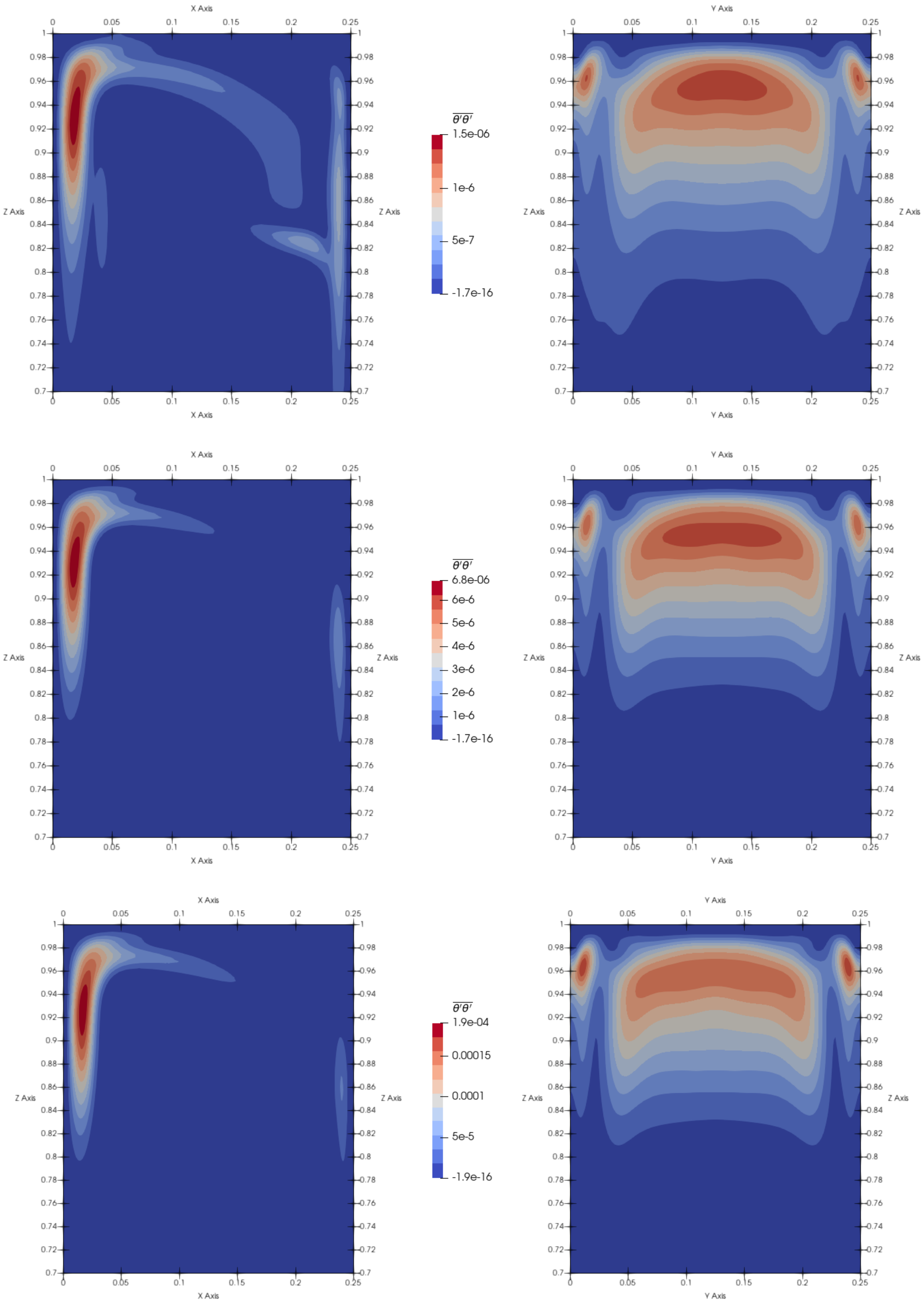

Figure 5.1: Slices of time-averaged temperature variance, from top to bottom $Ra = 2.75 \times 10^8$, 2.85×10^8, and 3.2×10^8. Left slices correspond to $y = 0.125$ and right slices to $x = 0.025$ (only $z \geq 0.7$ is shown).

Furthermore, although some cases, such as $Ra = 2.75 \times 10^8$, exhibit non-negligible temperature variance and the signal at point A appears monoperiodic after the initial transient state, the fluctuations continue to decay over time, reducing the signal amplitude. This behavior is shown in Figure 5.2, where the temporal evolution of the temperature at point A is displayed for various cases. In addition, localized fluctuations are observed in the upper region of the cold wall, which are absent in cases with higher Rayleigh numbers. Under these conditions, the flow is still considered steady rather than truly monoperiodic; these cases are therefore excluded from the linear fit analysis.

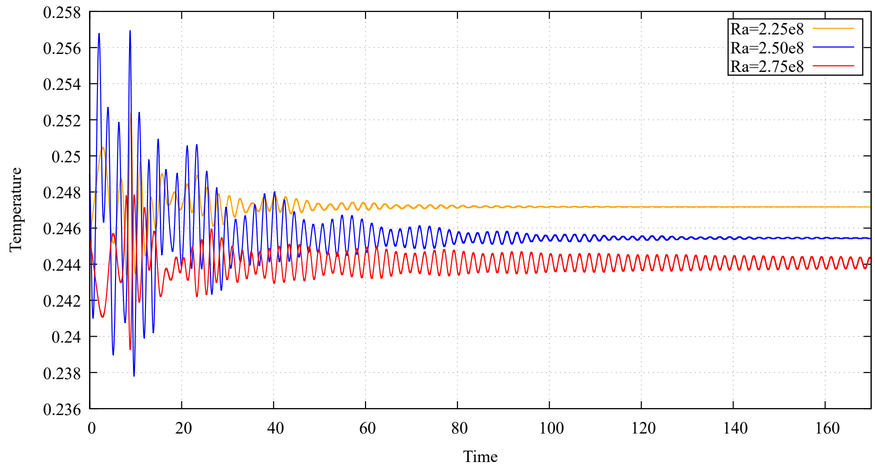

(a)

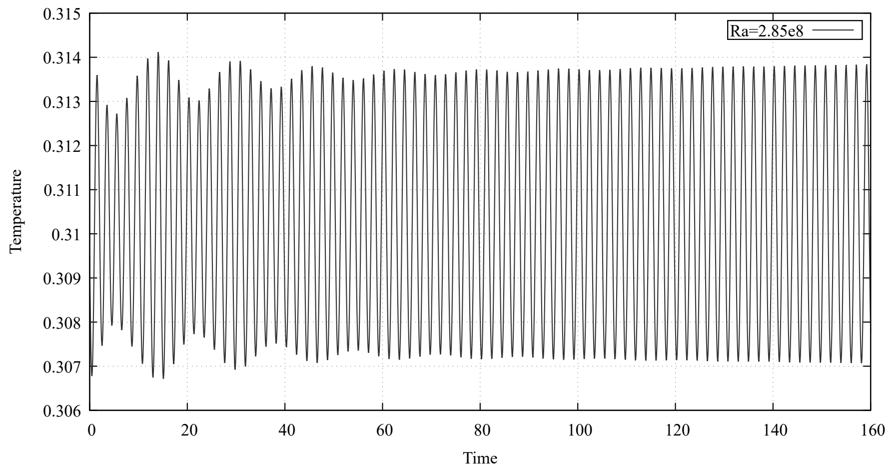

(b)

Figure 5.2: Temperature time series at monitoring point A. (a) $Ra = 2.25 \times 10^8$, 2.55×10^8, and 2.75×10^8: temperature fluctuations remain negligible or decay over time. (b) $Ra = 2.85 \times 10^8$: a stable monoperiodic oscillatory regime is observed.

A sustained monoperiodic regime is first observed near $Ra = 2.85 \times 10^8$, where the fluctuations reach significantly larger values compared to lower Rayleigh numbers and remain stable over time. The oscillatory motion exhibits a nondimensional frequency of $f = 0.479$ for both points, corresponding to an angular frequency of $\omega = 3.011$, for the cases analyzed. This value is close to the nondimensional angular frequency $\omega = 2.5$ reported by [16] for the two-dimensional case, and to $\omega = 2.73$ reported by [18] at the onset of time-dependent three-dimensional flow under periodic boundary conditions, although it is noticeably higher. The difference may be attributed to the influence of the front and rear no-slip walls, which enhance three-dimensional effects and modify the boundary-layer structure where the travelling-wave instability develops, thereby affecting the oscillation frequency.

5.1.2 Critical Rayleigh Number Calculation

Table 5.1 presents the simulated cases along with the time-averaged temperature variance at points A and B, computed over the final 50 time units of the simulation, as well as the dominant frequency of the temperature signal at each point for the fully developed monoperiodic states. It can be seen that the temperature fluctuations at the mid-depth location are generally larger than those measured at the quarter-depth location. The only exception is the case $Ra = 3.2 \times 10^8$, where point B exhibits a slightly higher temperature variance than point A.

This behavior is consistent with Figure 5.1, which illustrates that the region of maximum fluctuations broadens in the y-direction with increasing Ra, allowing elevated variance levels to extend toward the walls. This suggests that, beyond $Ra = 3.1 \times 10^8$, the Rayleigh number begins to influence

Table 5.1: Temperature variance of point A and B for the simulated cases.

Case	$\overline{\theta'\theta'}_A$	$\overline{\theta'\theta'}_B$	f_a	f_b	State
1.0×10^8	-	-	-	-	Steady
2.0×10^8	-	-	-	-	Steady
2.25×10^8	-	-	-	-	Steady
2.5×10^8	-	-	-	-	Steady
2.75×10^8	-	-	-	-	Steady
2.85×10^8	$5.52368472 \times 10^{-6}$	$4.93252371 \times 10^{-6}$	0.4793	0.4793	Monoperiodic
2.9×10^8	$1.85612390 \times 10^{-5}$	$1.80788559 \times 10^{-5}$	0.4792	0.4788	Monoperiodic
2.95×10^8	$5.83514577 \times 10^{-5}$	$5.48225917 \times 10^{-5}$	0.4793	0.4793	Monoperiodic
3.0×10^8	$7.71985670 \times 10^{-5}$	$7.38314592 \times 10^{-5}$	0.4793	0.4793	Monoperiodic
3.1×10^8	$1.18474466 \times 10^{-4}$	$1.17228490 \times 10^{-4}$	0.4795	0.4795	Monoperiodic
3.2×10^8	$1.52329470 \times 10^{-4}$	$1.54877552 \times 10^{-4}$	0.4795	0.4795	Monoperiodic

the distribution of fluctuation maxima in the y-direction. In contrast, no comparable redistribution is observed in the vertical (z-direction), where the dynamics are strongly constrained by buoyancy and boundary-layer mechanisms.

Using the linear relationship given in Equation 4.4, the data for $Ra \geq 2.85 \times 10^8$ were fitted to determine the critical Rayleigh number. The results are presented in Figure 5.3, where critical of $Ra_{c,A} = 2.834 \times 10^8$ and $Ra_{c,B} = 2.840 \times 10^8$ are identified for points A and B, respectively. The critical values obtained here are significantly higher than those reported by Xin and Le Quéré [18], who found $Ra = 1.032 \times 10^8$ for two-dimensional oscillatory disturbances in a DHC with periodic boundary conditions. This discrepancy is readily explained by the no-slip boundary conditions employed in the present configuration: the solid walls act as dissipative layers that damp disturbances, requiring stronger gradients to trigger the first bifurcation.

Furthermore, the fact that a slightly lower critical value is found at the mid-depth location compared to the quarter-depth location should be interpreted with caution, given that the difference between the estimated values is minimal. Additionally, the dominant frequency extracted from the signals at points A and B is the same for all cases, with the exception of $Ra = 2.9 \times 10^8$. This case slightly departs from the general trend, likely due to residual transient contamination wich, given the small signal amplitude, makes it particularly sensitive to perturbations. Such uniformity indicates that spatial location affects only the amplitude of the response rather than the temporal dynamics. This behavior is consistent with a global instability governed by a single bifurcation parameter.

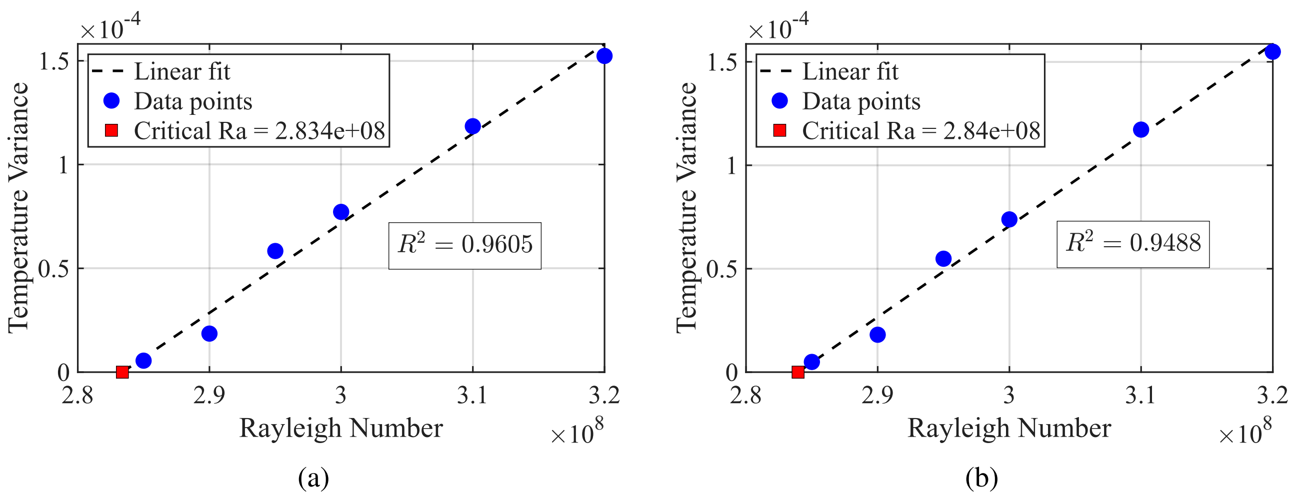

Figure 5.3: Linear fit for the data and critical Rayleigh calculation. Left is for monitoring point A and right for point B.

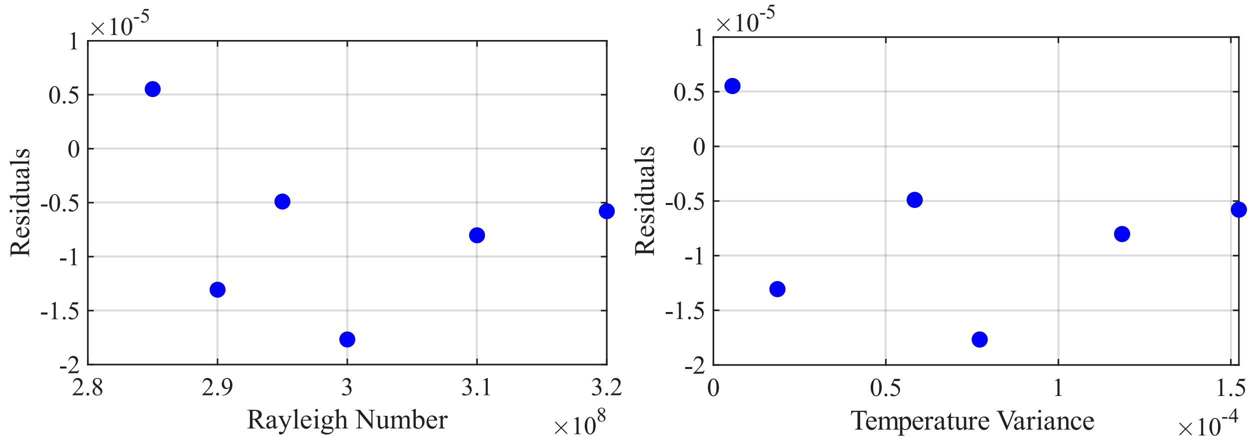

(a) (b)

Figure 5.4: Residuals of the linear fit as a function of (a) the Rayleigh number and (b) the temperature variance for monitoring point A.

The validity of the linear fit is assessed through a residual analysis. The coefficient of determination, $R^2 = 0.9605$ for monitoring point A, indicates that the linear model captures the dominant trend of the data with high accuracy. More importantly, the residuals shown in Figure 5.4 are distributed around zero and exhibit no discernible trend, curvature, or systematic structure, which confirms the adequacy of the linear approximation within the fitted range. Since the Rayleigh number and the oscillation amplitude are linearly related in this regime, the residual distributions obtained using either variable are expected to be equivalent; both representations therefore display the same qualitative behavior. Although a slight negative bias is observed, no systematic dependence is detected. This bias can be reasonably attributed to finite sampling effects, sensitivity to the chosen initial conditions, or residual transient contributions.

Calculation Using Vertical Velocity

The critical Rayleigh number can also be estimated from the vertical velocity (w) signals. As shown in Figure 5.5, a linear extrapolation of the corresponding amplitudes yields critical values of $Ra_{c,A} = 2.823 \times 10^8$ for point A and $Ra_{c,B} = 2.840 \times 10^8$ for point B. These values are consistent with those obtained from the temperature signals and again indicate a slightly lower Ra_c for the mid-depth location compared to the quarter-depth location. This behavior highlights the intrinsic coupling between the vertical velocity component and the temperature field at the onset of oscillatory convection. Notably, although the critical parameter is identified at mid-depth, it is interesting to note that the amplitude of the fluctuations is lower at point A than at point B, indicating that the detection of the

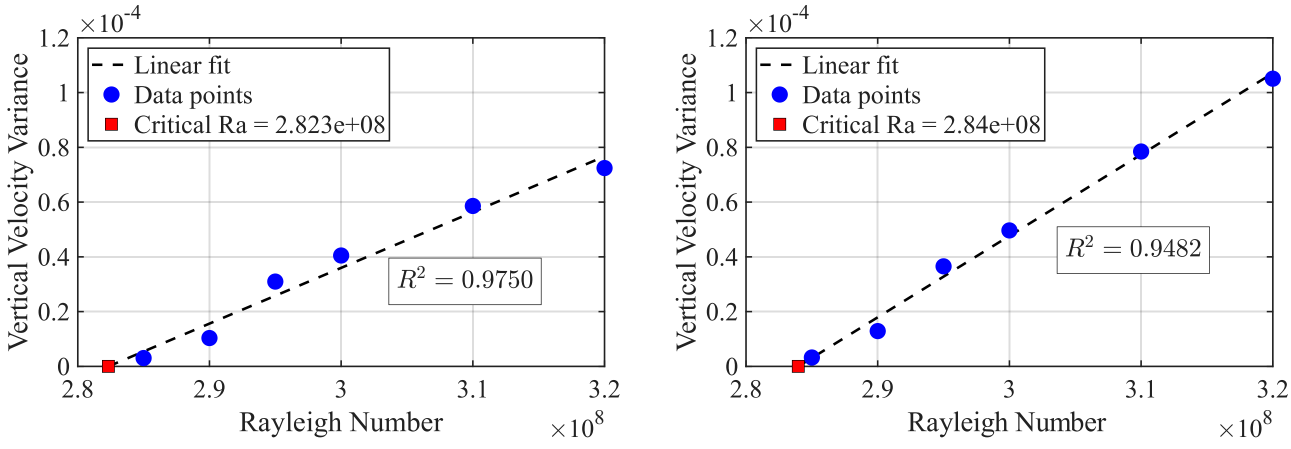

Figure 5.5: Linear fit of the data and critical Rayleigh number calculation using vertical velocity. Left is for monitoring point A and right for point B.

critical Rayleigh number is independent of the location of maximum fluctuation intensity in the depth direction.

5.2 Global Analysis of Fully Turbulent Flow

5.2.1 Time Averaged Fields

The turbulent case $Ra = 10^{10}$ is first analyzed by visualizing the time-average fields. In Figure 5.6, slices of the mean temperature are presented. The temperature field displays the canonical structure of a DHC, characterized by a thermally stratified core and very steep gradients near the isothermal walls. Figure 5.7 shows the plane-average temperature over the (x, y) planes as a function of the z-coordinate. Results reported by Trias et al. [11], obtained with periodic boundary conditions, are included for comparison.

Minimal differences are observed between the two profiles, both graphs show uniform thermal stratification in the cavity core, characterized by a vertical temperature gradient $(\partial\theta/\partial z)$ equal to unity. Consequently, since the mean stratification of the core is equivalent in both configurations, the Brunt–Väisälä frequency N is expected to take the same value regardless of the boundary conditions imposed at the front and rear walls. Additionally, this close correspondence rules out the boundary conditions imposed at the front and rear walls as a potential source of the discrepancies between numerical and experimental results regarding the thermal stratification. Furthermore, it supports the conclusion that

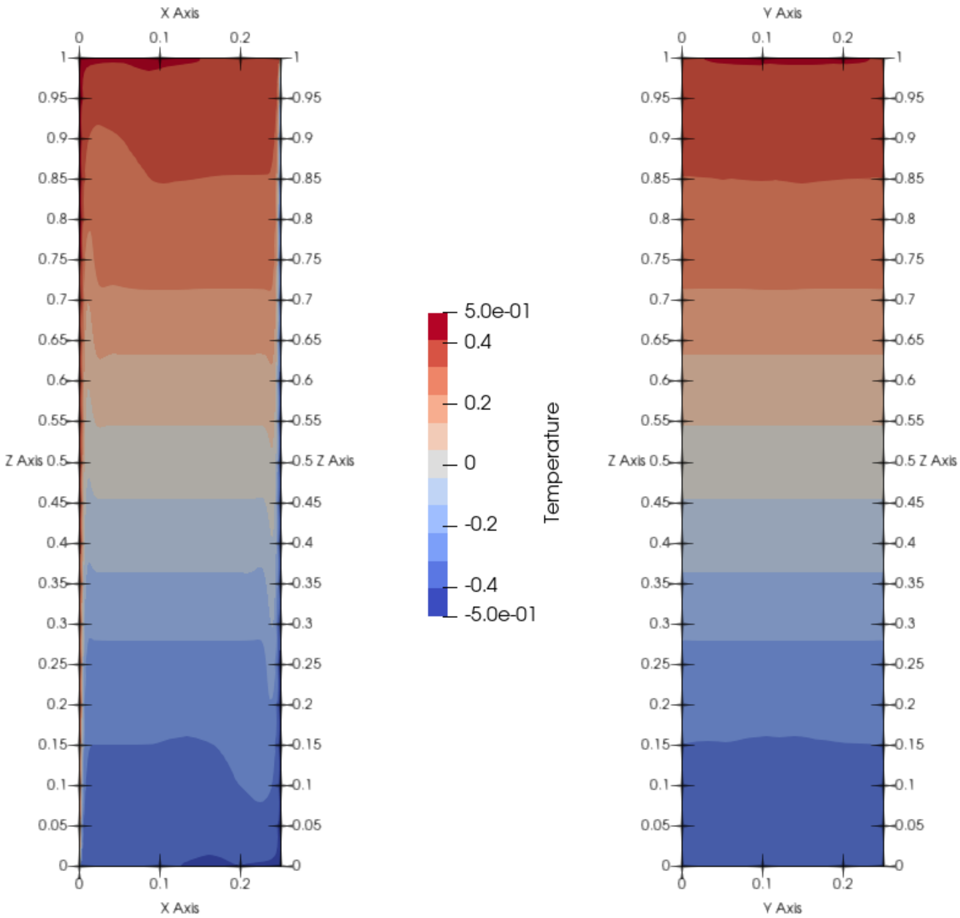

Figure 5.6: Slices of average temperature for $Ra = 10^{10}$, (left) $y = 0.125$ and (right) $x = 0.125$.

these differences arise from thermal radiation effects.

Slices of the mean magnitude of the velocity field are presented in Figure 5.8. This field, as well as the temperature field, exhibits clear point antisymmetry, which further validates the simulation. The velocity field indicates that the core remains nearly at rest, while thin boundary layers develop within the main recirculation cell. The velocity magnitude increases immediately after the fluid separates from the top and bottom walls, where the vertical boundary layers begin to form. This increase continues until the onset of boundary-layer destabilization, which ultimately leads to the ejection of large-scale structures into the core of the cavity at approximately $z = 0.8$. In Appendix B, slices of the average velocity components (Figures B.1–B.3) are also provided.

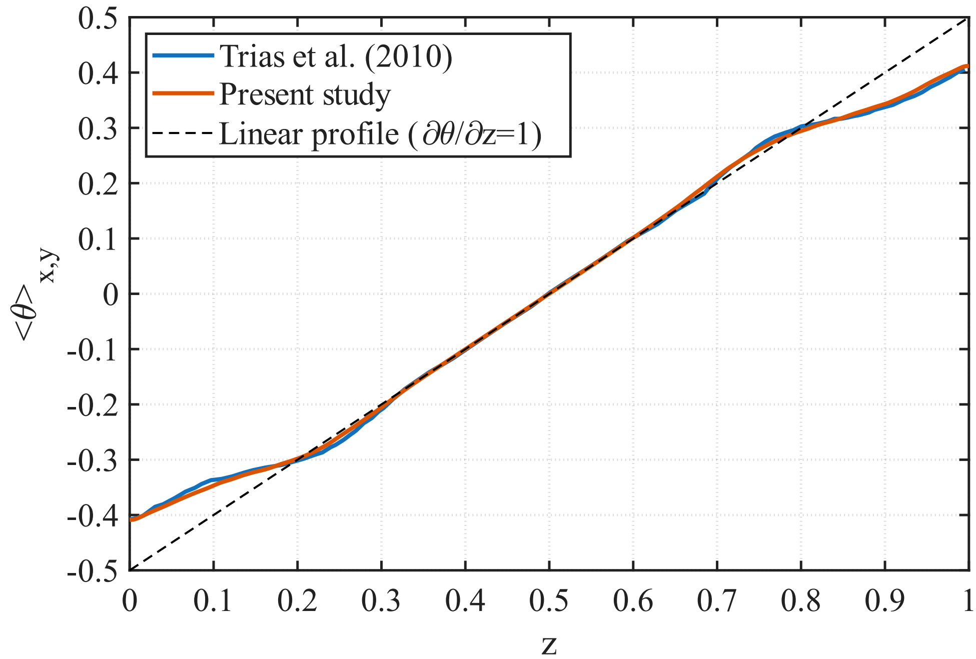

Figure 5.7: Average temperature in the $(x,\, y)$ planes for $Ra = 10^{10}$ as a function of the z-coordinate. Results adapted from [11], obtained using periodic boundary conditions, are included for comparison.

5.2.2 Boundary Layer

Based on the mean-field results, the velocity boundary layer is characterized by the friction velocity, the boundary-layer thickness, and the friction Reynolds number. Figure 5.9 shows the distribution of the vertical friction velocity as a function of y and z at the hot wall ($x = 0$). The largest values occur near the bottom of the cavity, where the thermal gradients are strongest. These enhanced gradients intensify the buoyancy-driven flow, leading to larger velocity gradients at the wall and, consequently, higher friction velocity. As z increases, the thermal and velocity gradients progressively weaken, and the friction velocity decreases until it approaches zero at the top of the cavity.

The boundary-layer thickness measures introduced in Subsection 4.4.3, namely δ_1, δ_2, and δ_3, are displayed in the top panels of Figure 5.10 as functions of y and z at the hot wall ($x = 0$). Their corresponding friction Reynolds numbers are presented in the bottom panels. As expected, the location of the maximum vertical velocity, δ_1, increases with increasing z, reflecting the progressive thickening of the boundary layer. A similar behavior is observed for the integral thickness δ_2 defined in Equation 4.11. The maximum thickness occurs around $z \approx 0.85$, which is consistent with the region where the boundary layer becomes most unstable.

However, this trend is not evident when considering the zero crossing of the vertical velocity, δ_3. After

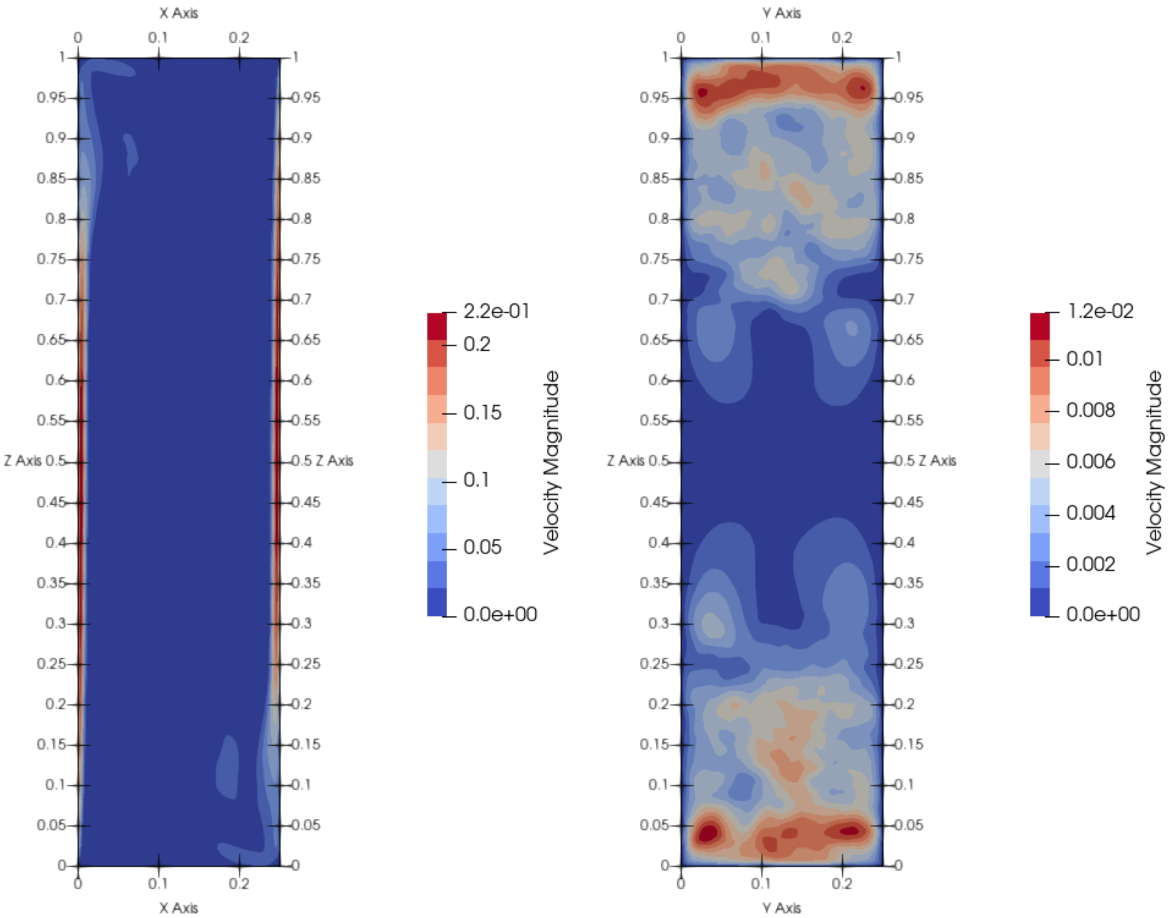

Figure 5.8: Slices of average velocity magnitude for $Ra = 10^{10}$, (left) $y = 0.125$ and (right) $x = 0.125$.

a region of very large values within $0 \lesssim z \lesssim 0.3$, produced by jets impinging from the bottom wall onto the vertical hot wall, δ_3 decreases until approximately $z \approx 0.6$, after which it begins to increase. A sudden jump appears near $z \approx 0.8$, where the maximum values are observed. This behavior can be attributed to the influence of the top wall. Jets impinging on the top wall, together with flow structures ejected into the cavity core, directly affect the vertical boundary layer. A recirculation region ($w < 0$) develops just outside the boundary layer and becomes stronger as z increases, which shifts the location of the zero crossing of the vertical velocity toward the wall, leading to smaller values of δ_3.

Meanwhile, since the friction Reynolds number is directly proportional to the characteristic boundary-layer thickness for a constant value of the friction velocity, $Re_\tau(\delta_3)$ attains larger values than $Re_\tau(\delta_1)$ and $Re_\tau(\delta_2)$. A maximum value of approximately 110 is observed at $z \approx 0.8$. Such a value may appear relatively small for a fully developed turbulent boundary layer when compared with canonical

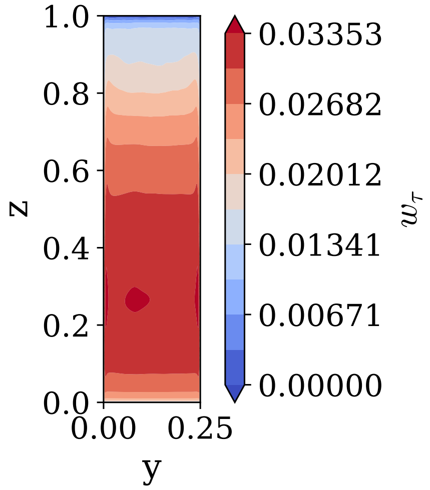

Figure 5.9: Friction velocity $w_\tau(y,z)$ at the hot wall ($x = 0$) for $Ra = 10^{10}$.

values [61]. However, if the friction Reynolds number is instead defined using a friction velocity based on the ensemble mean of the vertical velocity ($\langle w_\tau \rangle = 0.0266$) and the width of the DHC as the length scale ($W^* = W/H = 0.25$) [62], the estimated value increases to $Re_\tau \approx 937$.

The boundary layer nature is next examined through the normalization of the vertical velocity and the wall-normal components in wall units. Figure 5.11 presents profiles of the normalized vertical velocity w^+ as a function of the wall-normal coordinate x^+ at different heights. The profiles display the qualitative structure typical of vertical natural convection boundary layers; however, no well-defined logarithmic region can be identified, and a log-law fit is not supported by the data. This is also evident in Figure 5.12, where the distribution of the normalized velocity w^+ is shown against the wall normal distance in wall units x^+ for $z = 0.50, 0.55, 0.60, 0.65, 0.70, 0.75$. The top panel shows the normalization using the local friction velocity w_τ, while the bottom one uses the global friction velocity (ensemble average). The data closely follow the linear relation $w^+ = x^+$ for $x^+ < 5$, which indicates the presence of the viscous sublayer. However, when fitting a canonical log-law ($w^+ = \frac{1}{0.41} ln(x^+) + 5.0$), the data deviate significantly from this behavior. These results indicate a non-fully turbulent boundary layer, with the bulk of the flow being turbulent while the near-wall region remains laminar-like or weakly turbulent [59].

Finally, as shown in the right panels of Figure 5.11, the viscous sublayer is resolved with at minimum of two grid points in all cases. This ensures that near-wall gradients are adequately captured and further confirms the adequacy of the mesh resolution.

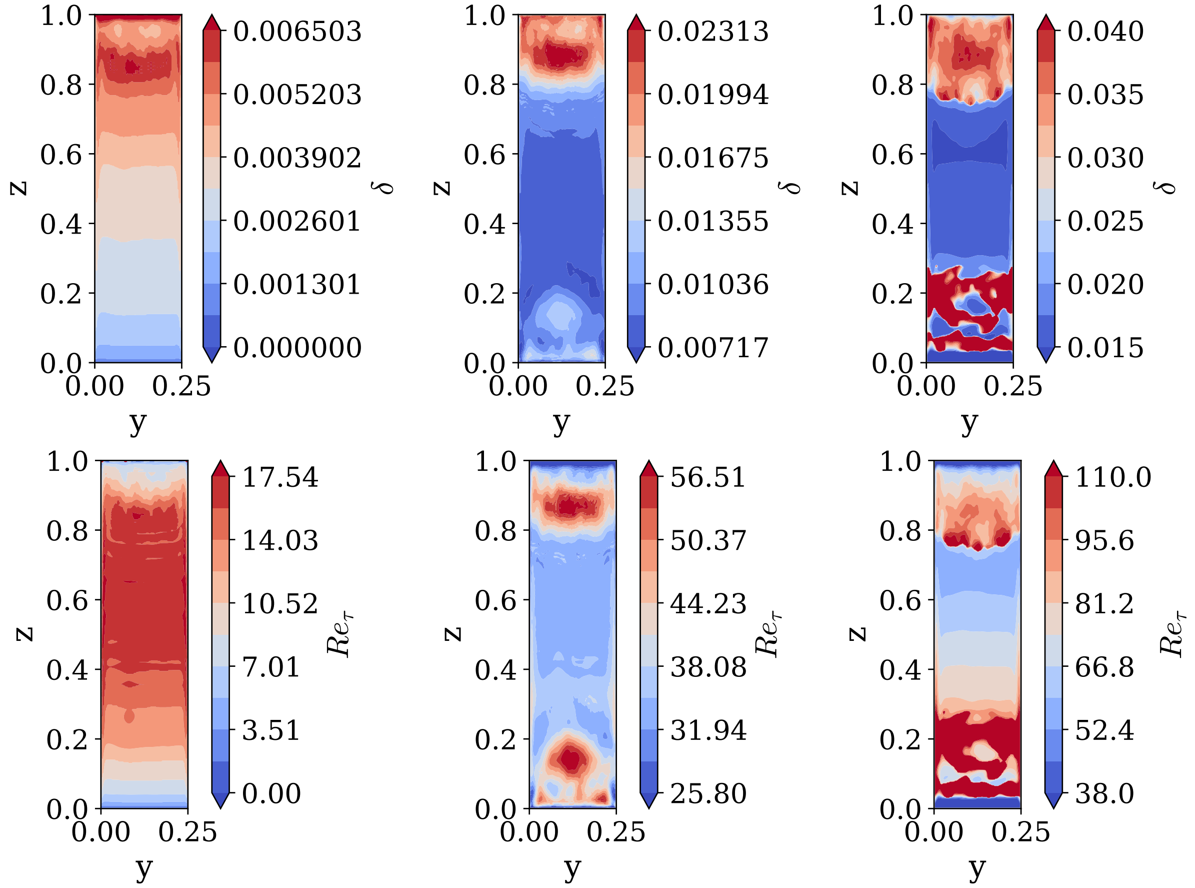

Figure 5.10: Local velocity boundary-layer thickness $\delta_v(y, z)$ at the hot wall for $Ra = 10^{10}$ (top row). From left to right: δ_1 (location of maximum vertical velocity), δ_2 (integral thickness defined in Equation 4.11), and δ_3 (first zero crossing of the vertical velocity). The corresponding friction Reynolds numbers $Re_\tau(y, z)$ are shown in the bottom row.

5.2.3 Heat Transfer

The heat transfer across the cavity is first investigated by analyzing the local Nusselt number distribution at the hot wall ($x = 0$ plane), as shown in the left panel of Figure 5.13. The maximum value of $Nu_{h,\max} = 441.329$ is clearly reached at the bottom of the wall ($z = 0$) where the largest temperature gradients occur as the cold fluid impacts the hot wall. As the air ascends along the wall, it is heated, thereby decreasing the Nusselt number as z increases until it reaches a value of $Nu_{h,\min} = 4.065$ at $z = 1$. Additionally, the spatially averaged Nusselt number at the hot wall, i.e., the global heat transfer rate, is obtained by integrating the local Nusselt number over the hot plate, yielding $\overline{Nu_h} = 100.9536$. This value is slightly lower than that reported by Trias et al., $\overline{Nu_h} = 101.94$, for a configuration employing periodic boundary conditions on the front and rear walls [11].

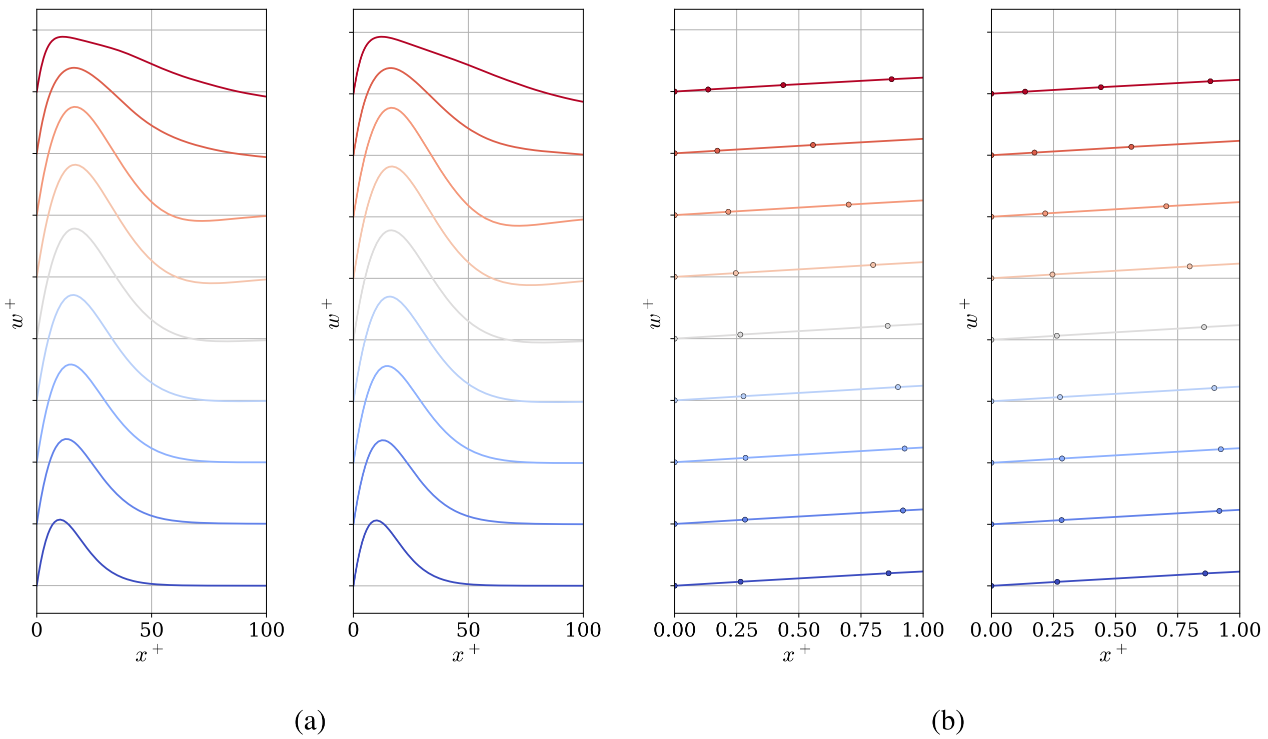

Figure 5.11: Profiles of the normalized vertical velocity w^+ versus the wall-normal coordinate x^+ at $z = 0.1, 0.2, 0.3, 0.4, 0.5, 0.6, 0.7, 0.8,$ and 0.9 (bottom to top) for $Ra = 10^{10}$. Curves are vertically offset, with each vertical subdivision representing 4 units of w^+. The left panels correspond to $y = 0.125$ and $y = 0.1875$ across the full boundary-layer range (a), while the right panels show the same spanwise locations restricted to the viscous sublayer ($x^+ \leq 1$), where markers indicate the computational mesh points (b).

The lower Nusselt number obtained when no-slip boundary conditions are imposed on the front and rear walls suggests a reduction in the overall convective heat transfer compared to the periodic configuration. This behavior arises from the additional viscous effects introduced by the solid walls. In the no-slip case, velocity gradients develop at these boundaries, forming shear layers that act as sinks of kinetic energy through viscous dissipation. Consequently, less turbulent kinetic energy is available to sustain convective motions. Moreover, the presence of solid walls alters the large-scale flow organization. While periodic boundary conditions allow coherent circulation structures to extend laterally without interruption, potentially promoting stronger bursting processes and enhanced mixing. In contrast, no-slip walls confine the flow and disrupt this lateral coherence.

The Nusselt number variance at the hot wall ($x = 0$), as shown in the right panel of Figure 5.13, presents a distinct region within $0.7 \leq z \leq 0.9$ where fluctuations are most prominent. The maximum value of 652.465 is found at $z \approx 0.83$. This location serves as an indicator of where transition occurs

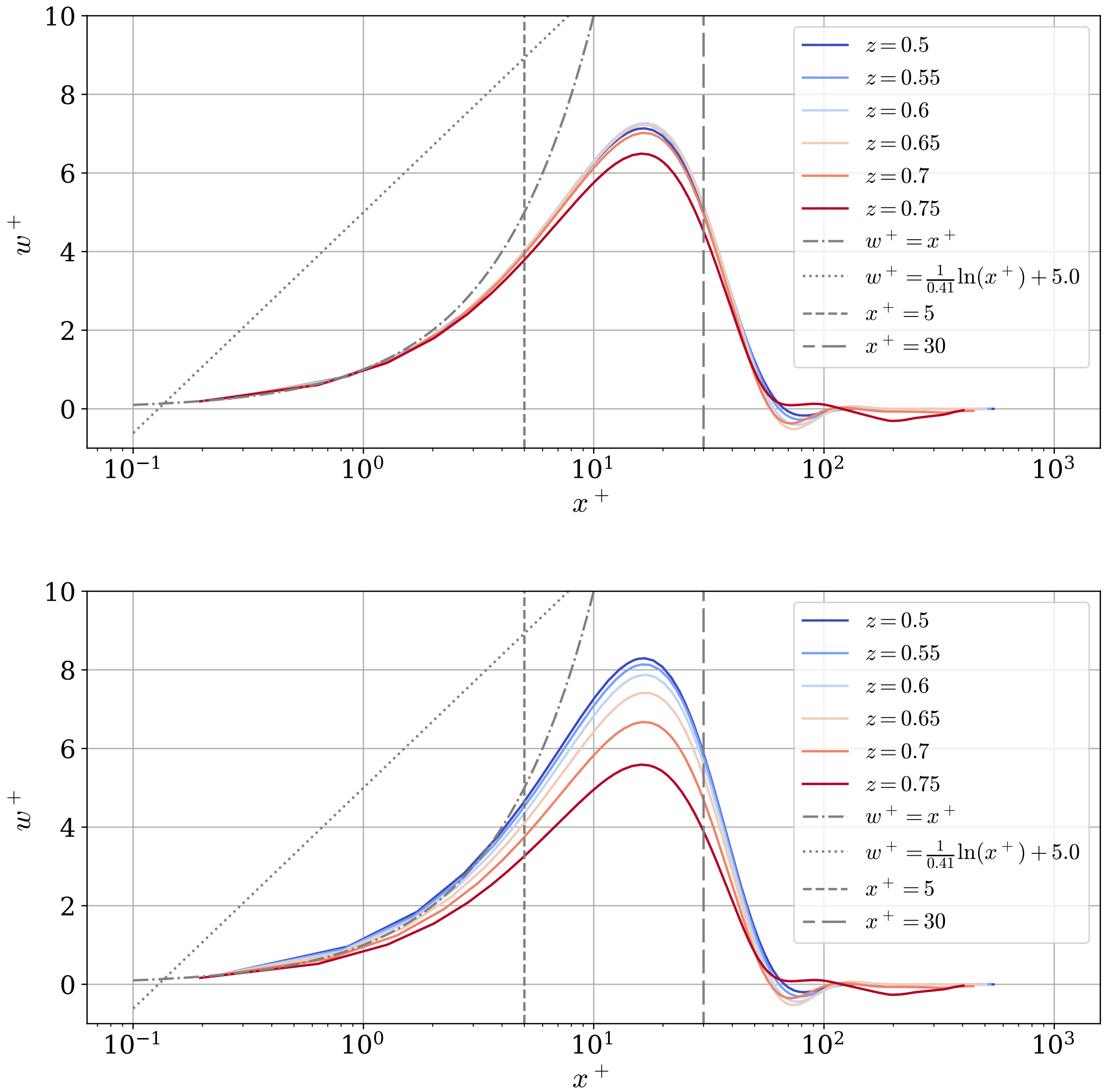

Figure 5.12: Distribution of the normalized vertical velocity w^+ versus the wall-normal distance in wall units x^+, at $y = 0.125$ and vertical locations $z = 0.5, 0.55, 0.60, 0.65, 0.70, 0.75$. The top panel shows the profiles normalized by the local friction velocity w_τ, while the bottom panel uses the global friction velocity (ensemble average). The viscous sublayer relation $w^+ = x^+$ and the logarithmic law $w^+ = \frac{1}{\kappa}\ln(x^+) + B$, with $\kappa = 0.41$ and $B = 5.0$, are included for reference to assess the boundary-layer structure.

in the vertical boundary layer [63]. This height is greater than that obtained using periodic boundary conditions in the depth direction, which occurs at $z = 0.813$. Table 5.2 summarizes the key heat transfer values discussed above. It is important to note that no averaging was performed in the depth-

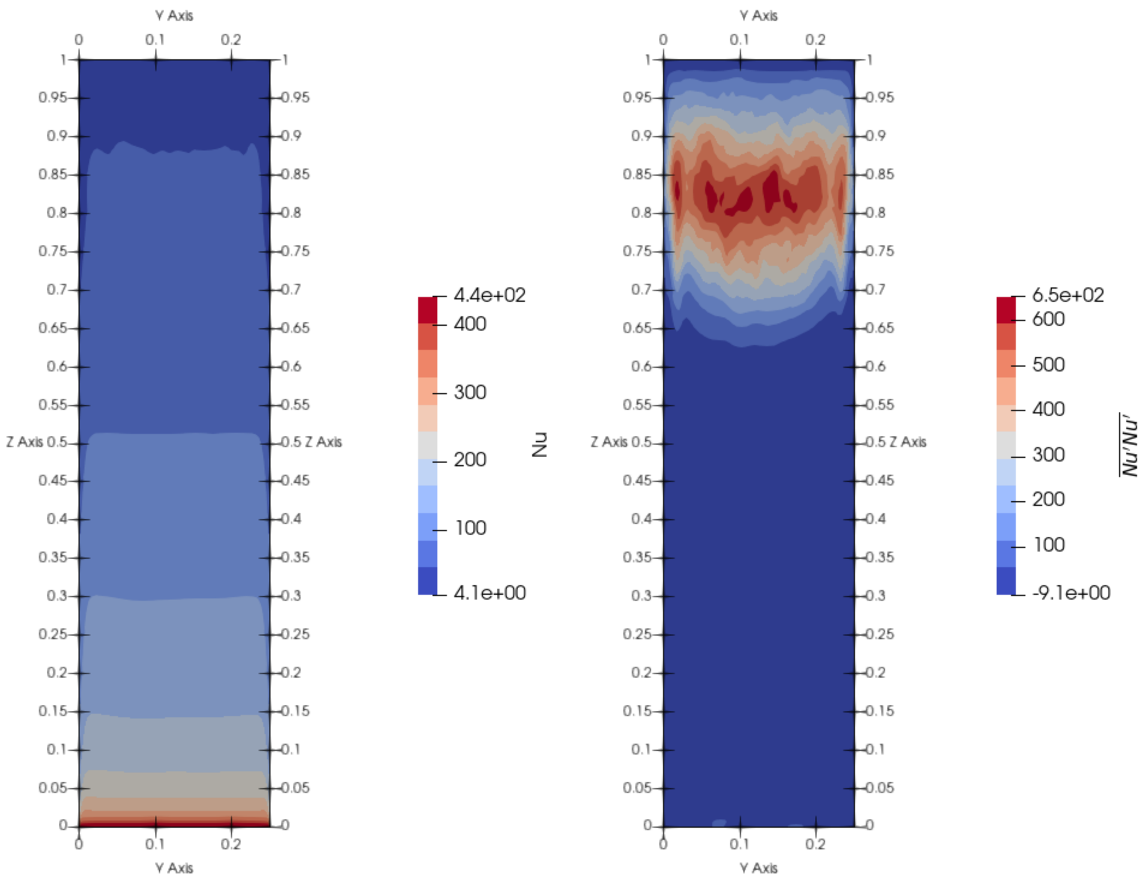

Figure 5.13: Distributions of the local Nusselt number (left) and its variance (right) at the hot wall ($x = 0$ plane) for $Ra = 10^{10}$.

Table 5.2: Global Nusselt number, maximum and minimum local Nusselt numbers, and the maximum variance of the local Nusselt number at the vertical hot wall. The corresponding z-locations are reported for the local quantities. Results from Ref. [63], obtained using periodic boundary conditions in the depth direction, are included for comparison.

Quantity	Present study	Trias et al. (2010)
$\overline{Nu_h}$	100.9536	101.94
$Nu_{\max}$	441.329	459.50
z	0	0
$Nu_{\min}$	4.065	-
z	1	-
$\overline{Nu'Nu'}$	652.465	642.623
z	0.83	0.813

wise direction in the present study.

Additionally, the alternating pattern along the y-direction reported for $Ra = 10^8$ [19] is no longer observed. The distribution is approximately uniform in the central region of the wall. Significant spatial variations along the depth appear only near the top of the cavity, where localized distortions in the Nusselt number field are observed. This region coincides with the area of strongest turbulent activity, suggesting a greater influence of turbulent fluctuations on the wall heat transfer. It is expected that averaging the Nusselt number over a longer time interval would further smooth the distribution.

Further insight into the discussed mechanisms can be obtained by analyzing the spatial distribution of the enthalpy flux, $\boldsymbol{u}\theta$. This term represents where and how strongly heat is being carried by the flow, i.e., the rate at which thermal energy is transported by fluid motion inside the cavity. At high Rayleigh numbers, convection dominates over conduction; therefore the enthalpy flux is especially informative since it governs the heat transfer. Figures 5.14-5.16 present slices of the components of the enthalpy flux. Considering the intrinsic symmetries of the fields, only the upper part of the cavity ($z > 0.5$) is shown. A strong correlation is observed between these fields and their corresponding velocity component distributions. It can be observed that the main recirculation cell associated with the boundary layers is responsible for the majority of the heat transport. Within the vertical boundary layer, as velocity and temperature increase with z, the enthalpy flux increases accordingly, until the disruption of the boundary layer leads to a significant reduction. Additionally, a region of intense heat flux is observed near the upper left corner, which weakens rapidly. In the central region, where the fluid remains quiescent on average, the enthalpy flux values decrease markedly and are governed by the spanwise (y) and vertical (z) components. The influence of the front and rear walls is also evident: the convective flux is reduced in their vicinity, which ultimately decreases the overall heat transfer capacity of the cavity.

5.2.4 Instantaneous Fields

Five snapshots of the temperature field in the $y = 0.125$ plane, taken at intervals of 25 time units, are presented in Figure 5.17. The fields display a clear thermal stratification in the core of the cavity, along with the development of coherent structures within the vertical boundary layers. These structures grow, detach from the boundary layer, and are advected along the wall by the mean circulation. Notably, when structures near the hot wall have already detached and are being transported, new structures are still forming along the cold wall. This phase shift between the two boundary layers is a key driver of the oscillatory behavior observed in the core region.

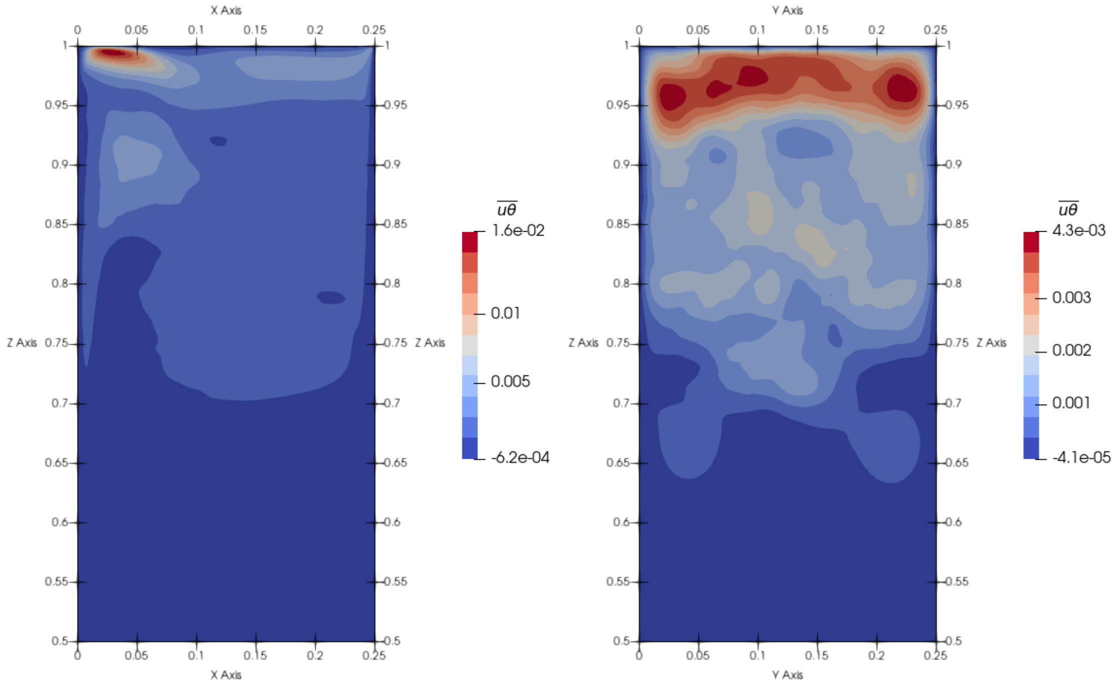

Figure 5.14: Slices of the time-averaged horizontal component of the enthalpy flux $\overline{u\theta}$ for $Ra = 10^{10}$: left, $y = 0.125$; right, $x = 0.125$. Only the upper region ($z > 0.5$) is shown.

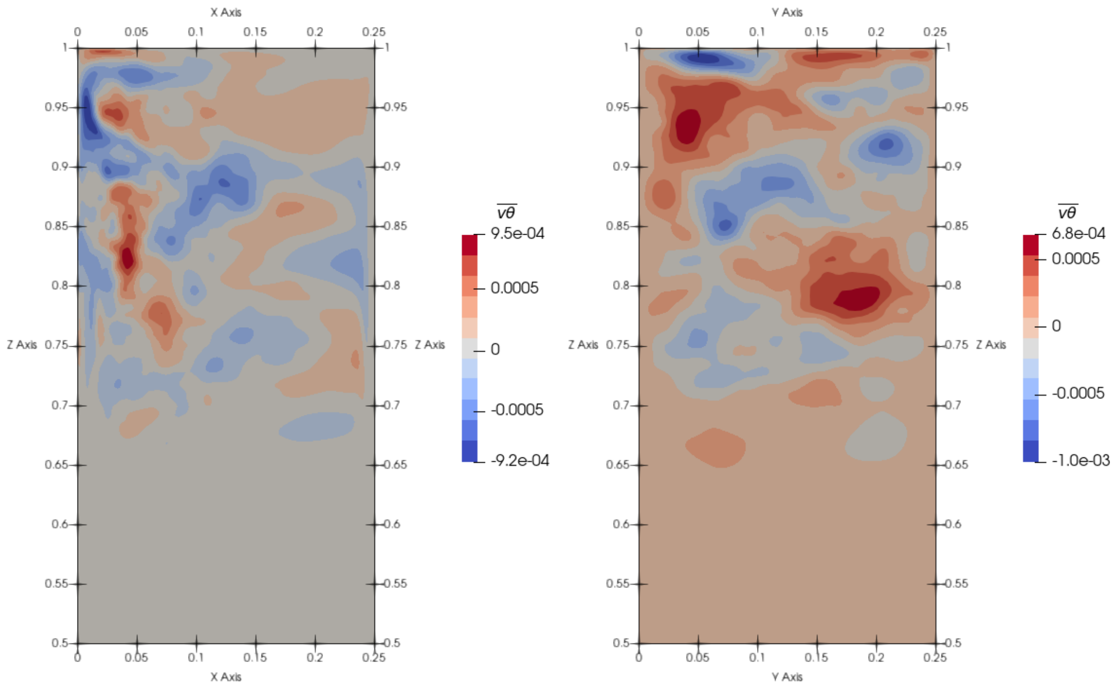

Figure 5.15: Slices of the time-averaged spanwise component of the enthalpy flux $\overline{v\theta}$ for $Ra = 10^{10}$: left, $y = 0.125$; right, $x = 0.125$. Only the upper region ($z > 0.5$) is shown.

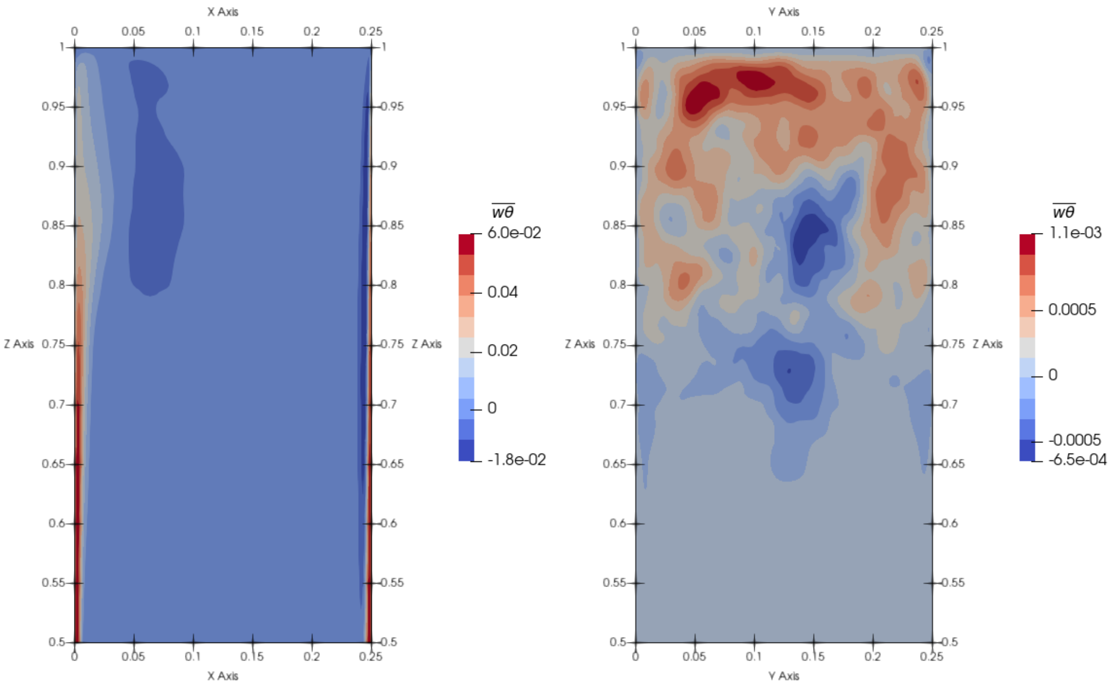

Figure 5.16: Slices of the time-averaged vertical component of the enthalpy flux $\overline{w\theta}$ for $Ra = 10^{10}$: left, $y = 0.125$; right, $x = 0.125$. Only the upper region ($z > 0.5$) is shown.

5.2.5 Second Order Statistics

The time-averaged distributions of the turbulent kinetic energy (e) and the individual contributions from the diagonal components of the Reynolds stress tensor, $\overline{u_i' u_i'}$ are shown in Figures 5.18-5.21. Additionally, the distributions of the temperature variance $\overline{\theta'\theta'}$, the viscous dissipation rate ε, the production of TKE by the mean flow $\mathcal{P}$, and the generation of TKE by buoyancy $\mathcal{G}$, derived from the TKE transport equation (see Equation 3.19), are illustrated in Figures 5.22-5.25. For each statistic, the first slice corresponds to the $y = 0.125$ plane, while the second corresponds to an x-normal plane where the largest fluctuations are observed; this allows for a detailed analysis of the depth-wise distribution. Finally, in consideration of the intrinsic symmetries of the fields, only the upper part of the cavity ($z > 0.5$) is shown.

First, as expected, turbulent kinetic energy is present almost exclusively in the downstream region of the vertical boundary layer ($z \in [0.65, 0.95]$); the upstream portion of the vertical boundary layer and the cavity core remain in a laminar state. In the depth-wise direction, maximum values are encountered near the mid-depth ($y = 0.125$). It is also observed that the spatial distribution of e closely matches that of the diagonal components of the Reynolds stress tensor, with the vertical velocity variance $\overline{w'w'}$ being the primary contributor to the turbulent kinetic energy. High values of e

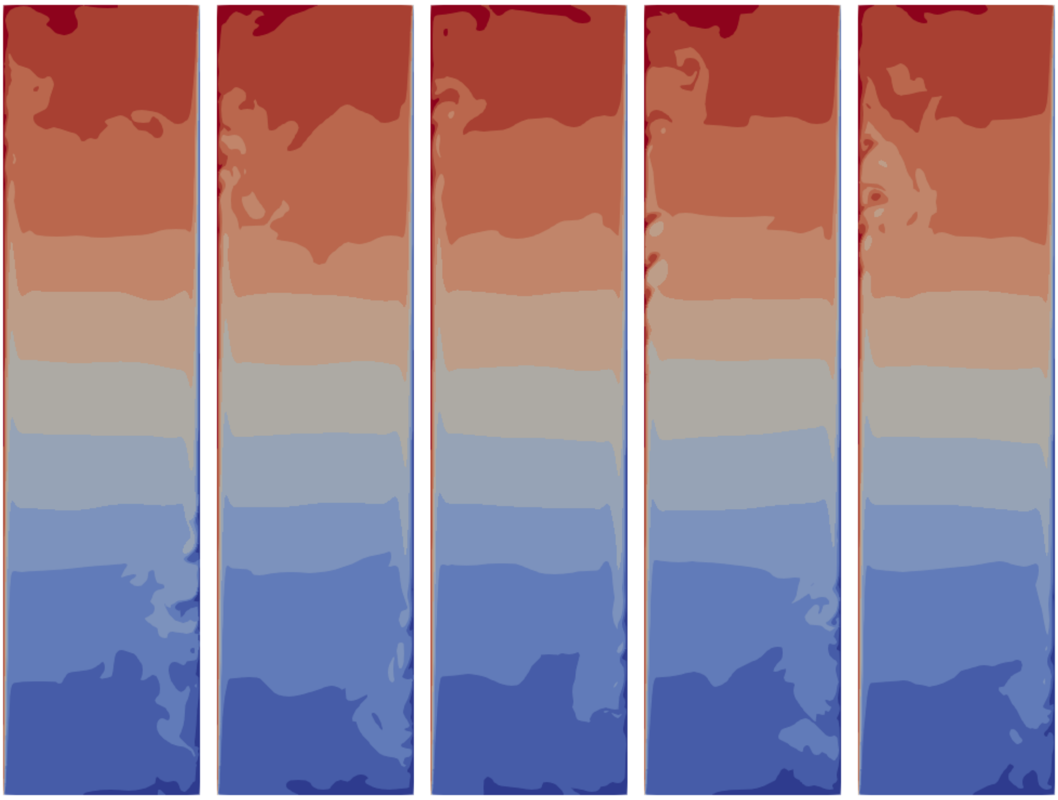

Figure 5.17: Slices of instantaneous field for $Ra = 10^{10}$ on the plane $y = 0.125$. Snapshots are taken every 25 units of time.

are not confined to the interior of the boundary layer; rather, they extend into the outer region, which is consistent with the ejection of coherent structures. Similarly, the temperature variance displays the same spatial trend, with peak values concentrated within the boundary layer, although the region of highest fluctuations is more sharply confined than its velocity counterpart.

Consistent with the findings of Trias et al. [63], a significant lack of correlation between the turbulent kinetic energy and the viscous dissipation rate is identified, thereby limiting the applicability of standard two-equation eddy-viscosity models. Near the wall, viscous dissipation is stronger due to high velocity gradients inside the boundary layer, diminishing progressively toward the core. This is readily seen in the upper panels of Figure 5.26, where the horizontal profiles of $2e$ and $(\sqrt{Ra}/Pr)\varepsilon$ at $z = 0.8$ for $y = 0.125$ and $y = 0.1875$ are shown. While the curves follow the same behavior reported by Trias et al., the viscous dissipation levels are nearly six times higher than those reported in their study [63]. Since viscous dissipation is strongly concentrated near the wall, it is highly sensitive to the spatial resolution and the averaging procedures employed. Therefore, differences in domain con-

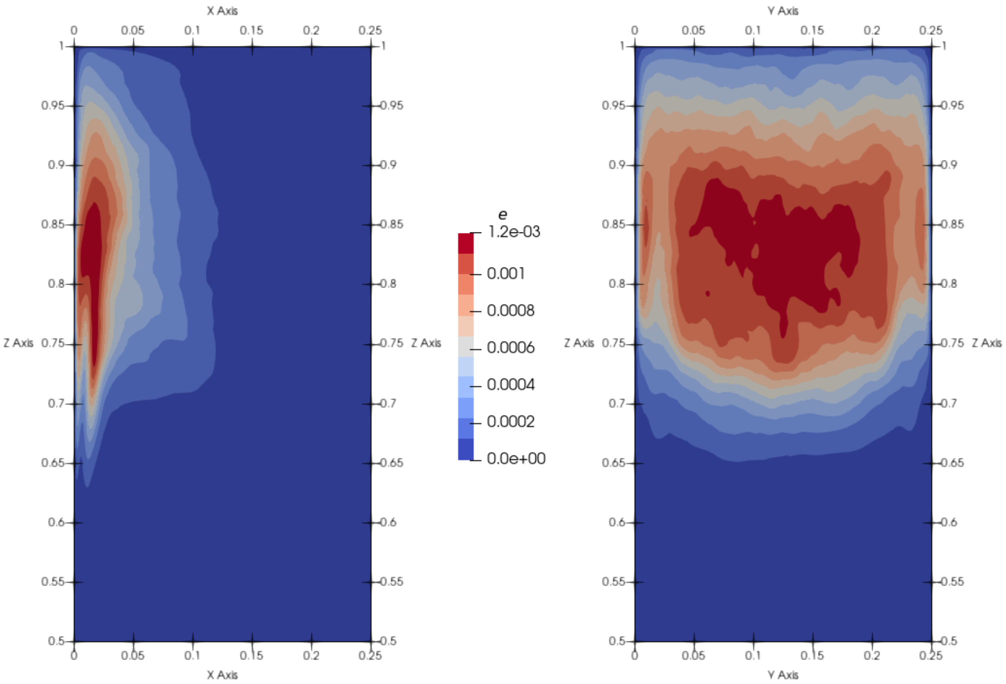

Figure 5.18: Time-averaged turbulent kinetic energy e for $Ra = 10^{10}$: left, $y = 0.125$; right, $x = 0.02$. Only the upper region ($z > 0.5$) is shown.

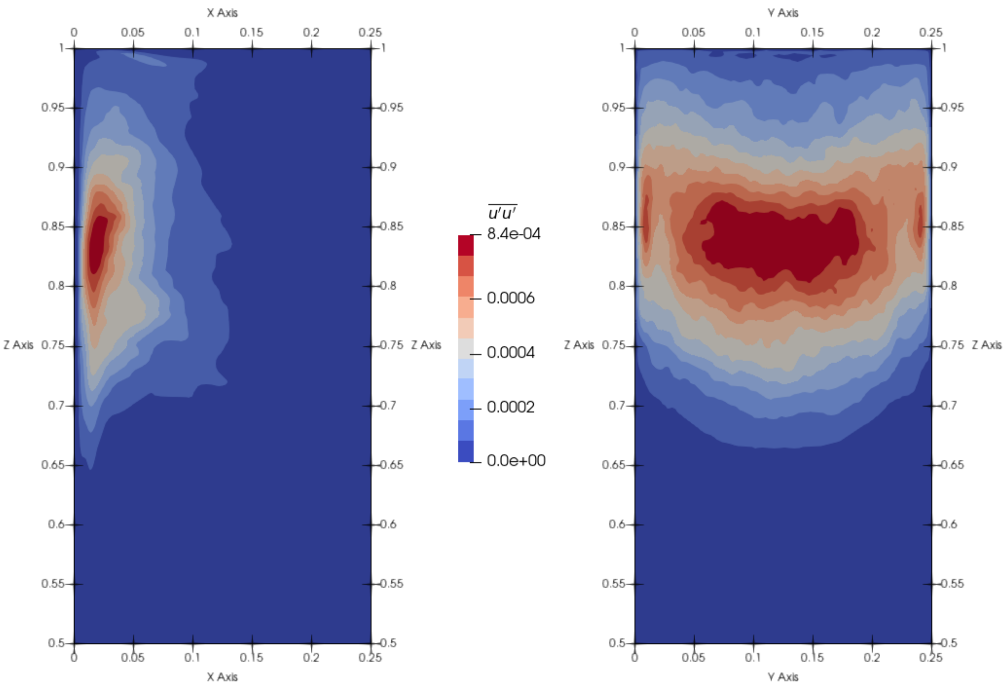

Figure 5.19: Time-averaged Reynolds stress component $\overline{u'u'}$ for $Ra = 10^{10}$: left, $y = 0.125$; right, $x = 0.02$. Only the upper region ($z > 0.5$) is shown.

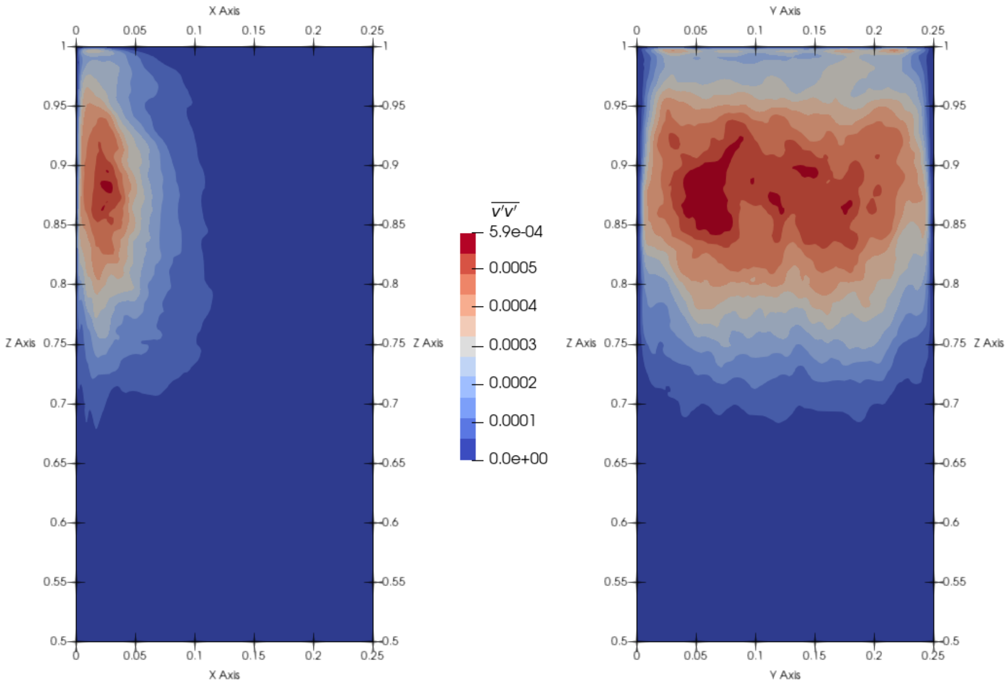

Figure 5.20: Time-averaged Reynolds stress component $\overline{v'v'}$ for $Ra = 10^{10}$: left, $y = 0.125$; right, $x = 0.02$. Only the upper region ($z > 0.5$) is shown.

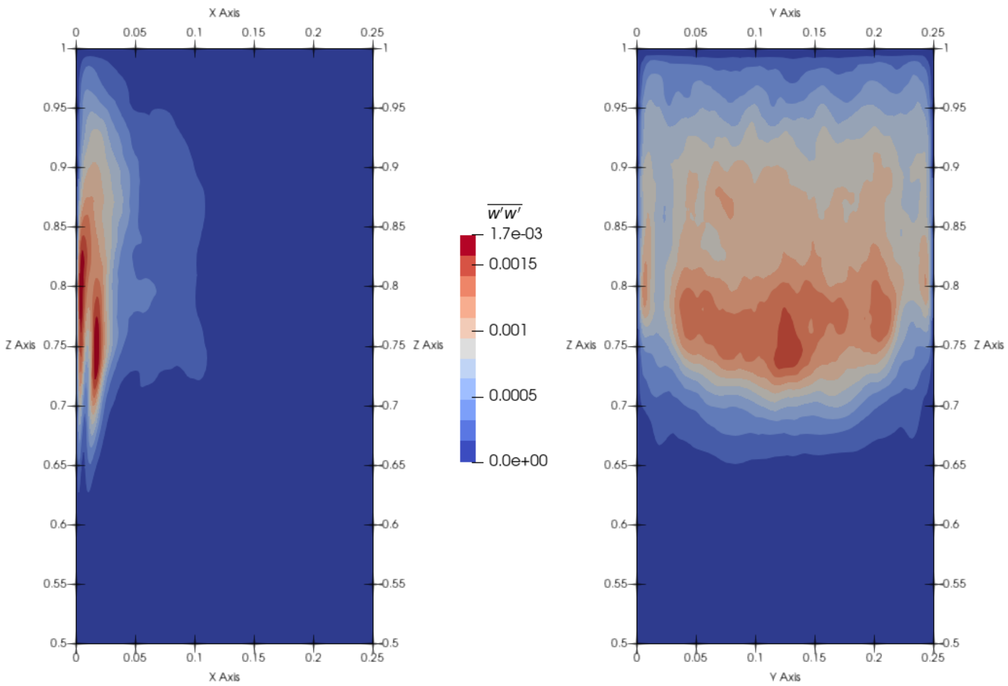

Figure 5.21: Time-averaged Reynolds stress component $\overline{w'w'}$ for $Ra = 10^{10}$: left, $y = 0.125$; right, $x = 0.02$. Only the upper region ($z > 0.5$) is shown.

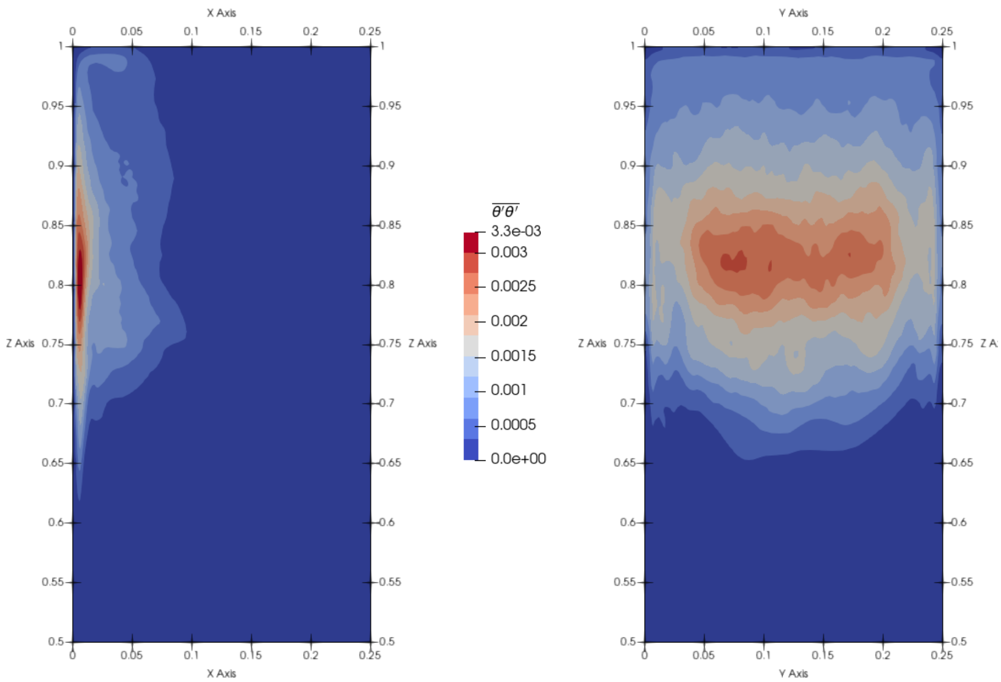

Figure 5.22: Time-averaged temperature variance $\overline{\theta'\theta'}$ for $Ra = 10^{10}$: left, $y = 0.125$; right, $x = 0.01$. Only the upper region ($z > 0.5$) is shown.

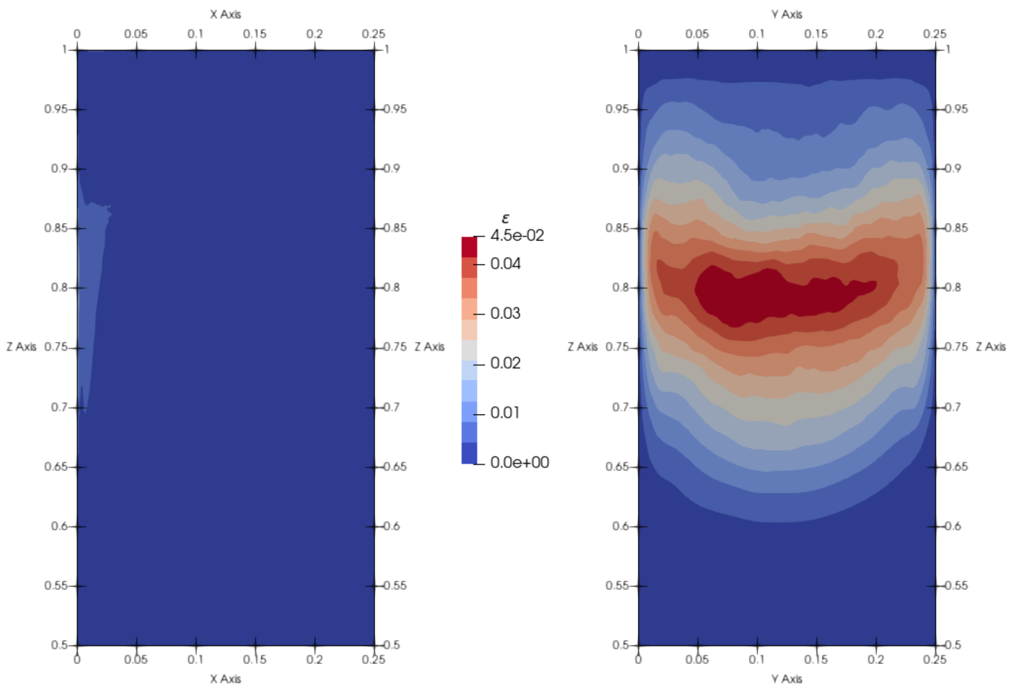

Figure 5.23: Time-averaged viscous dissipation rate ε for $Ra = 10^{10}$: left, $y = 0.125$; right, $x = 0.125$. Only the upper region ($z > 0.5$) is shown.

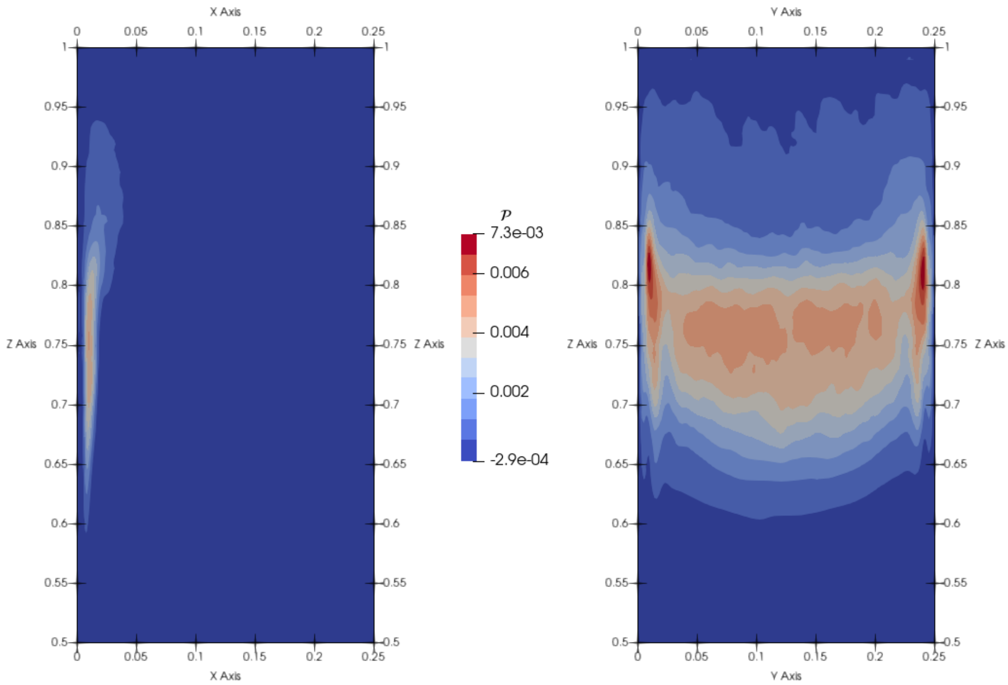

Figure 5.24: Time-averaged production of TKE by the mean flow $\mathcal{P}$ for $Ra = 10^{10}$: left, $y = 0.125$; right, $x = 0.01$. Only the upper region ($z > 0.5$) is shown.

figuration, specifically the presence of spanwise no-slip walls, likely contribute to this discrepancy in magnitude.

It can be observed that the production of turbulent kinetic energy by mean velocity gradients ($\mathcal{P}$) attains larger values than the buoyancy production ($\mathcal{G}$), with both contributions confined to a narrow region within the vertical boundary layer. Within this layer, shear production is not maximal at the wall (where $u_i = 0$) but rather in an inner region away from it, where both the mean velocity gradients and the Reynolds stresses are significant. This intermediate region therefore constitutes the primary location of TKE production. At the same time, upward motions of warm fluid within the hot boundary layer contribute positively to TKE through buoyancy, as indicated by the red regions in the figures. Conversely, intermittent downward motions of warm fluid, likely influenced by the adjacent recirculation zone, along with upward motions of cooler fluid, give rise to regions where buoyancy acts as a sink of TKE (blue regions).

The lower panels of Figure 5.26 present horizontal profiles at $z = 0.8$ for $y = 0.125$ and $y = 0.1875$ of $\mathcal{P}$ and $\mathcal{G}$, confirming that the buoyancy contribution remains significantly smaller than the production associated with mean shear at this height.

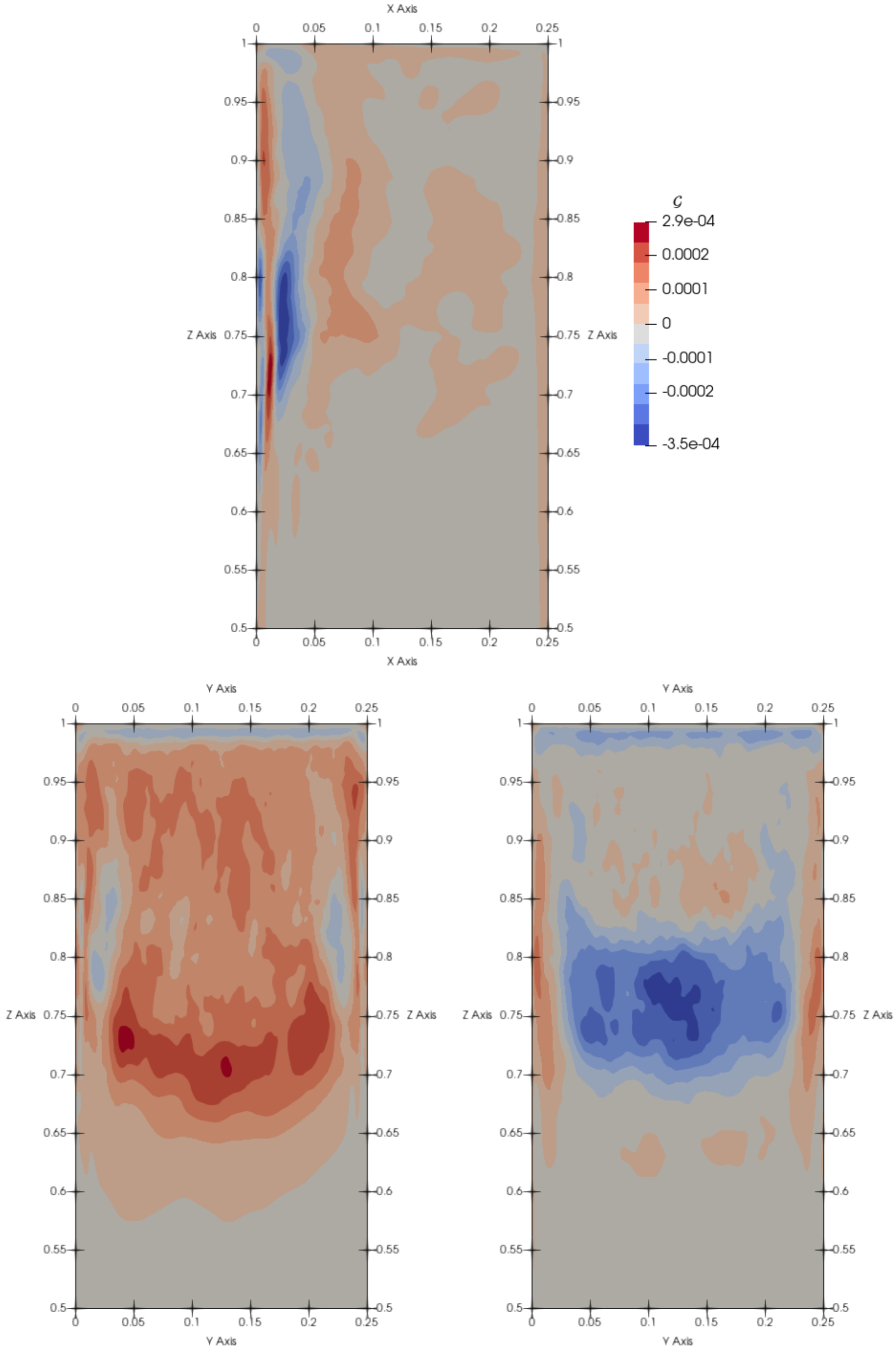

Figure 5.25: Time-averaged generation of TKE by buoyancy $\mathcal{G}$ for $Ra = 10^{10}$: up, $y = 0.125$; bottom, $x = 0.01$ (left), $x = 0.02$ (right). Only the upper region ($z > 0.5$) is shown.

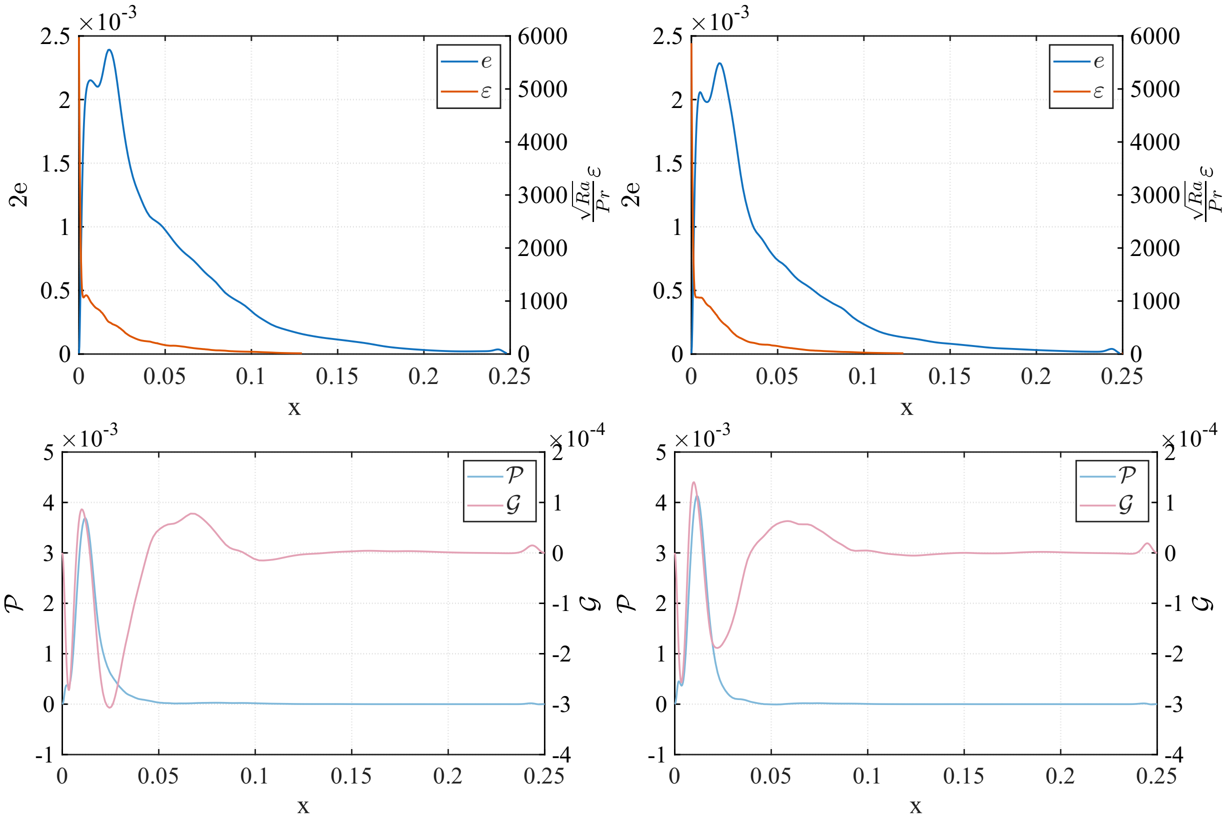

Figure 5.26: Horizontal profiles at $z = 0.8$ of the turbulent kinetic energy e scaled by 2 and its viscous dissipation rate ε scaled by $\frac{\sqrt{Ra}}{Pr}$ (top), and of the production of TKE by mean shear $\mathcal{P}$ and by buoyancy $\mathcal{G}$ (bottom). $Ra = 10^{10}$. Left panels correspond to $y = 0.125$, while the right panels correspond to $y = 0.1875$.

5.2.6 Local Flow Topology: Velocity-Gradient Invariants

The zone with the most intense turbulence statistics and where the ejection of structures occurs is analyzed using velocity-gradient invariants. This region of interest corresponds to the rectangular subdomain $\Omega_{\text{ROI}} = [0.001,\ 0.110]\times[0.005,\ 0.245]\times[0.65,\ 0.95]$. To assess the influence of the vertical wall on the local flow topology, the horizontal extent of the domain in the wall-normal direction is modified while keeping the y and z ranges fixed. In particular, the intervals $(x \in [0.001, 0.110])$ and $(x \in [0.003, 0.110])$ are examined to progressively exclude the near-wall region. A total of 500 snapshots, taken every 100 time steps, are used for the calculation of the probability density functions on a 500×500 bin discretization.

The joint probability density function of the second and third invariants $(Q,\ R)$ is shown in Figure 5.27 on a logarithmic scale for $Ra = 10^{10}$. The PDF exhibits the characteristic "teardrop" shape typical

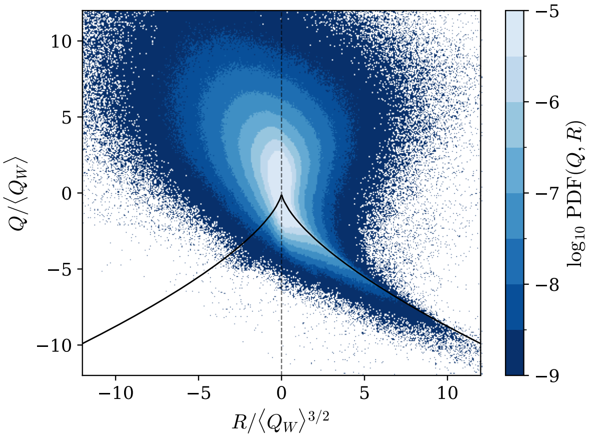

(a)

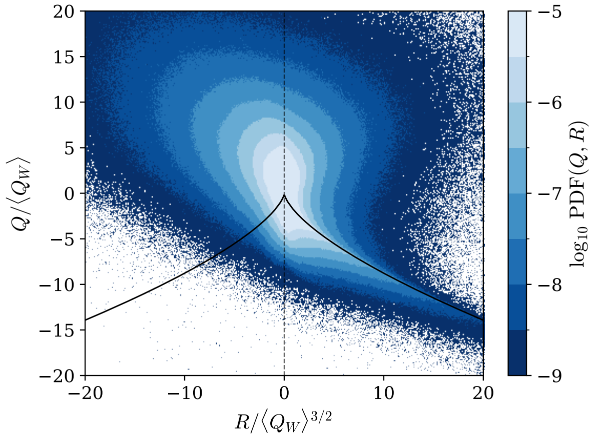

(b)

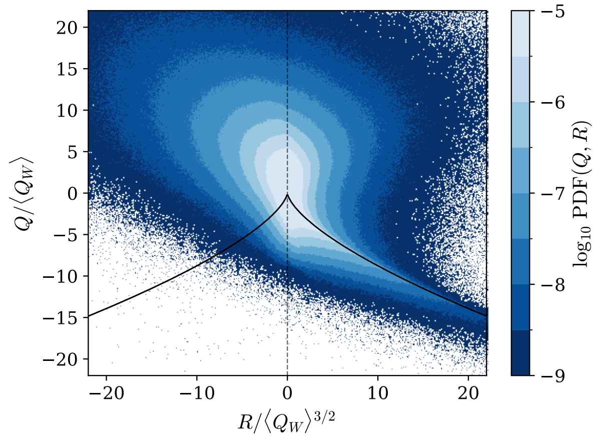

(c)

Figure 5.27: Joint PDF of Q and R invariants normalized by $\langle Q_W \rangle$ on logarithmic scale for $Ra = 10^{10}$. The regions of interest corresponds to $\Omega_{\text{ROI}} = [0.001,\, 0.110] \times [0.005,\, 0.25] \times [0.65,\, 0.95]$ (a), $[0.003,\, 0.110] \times [0.005,\, 0.25] \times [0.65,\, 0.95]$ (b), and $[0.003,\, 0.110] \times [0.005,\, 0.25] \times [0.65,\, 0.95]$ (c). The solid black line indicates the null-discriminant curve: $D = (27/4)R^2 + Q^3 = 0$.

of fully developed turbulence. The velocity-gradient statistics are strongly non-Gaussian, reflecting the intermittent nature of the flow. The predominance of events for $Q > 0$ indicates a prevalence of tube-like over sheet-like structures. Here, the teardrop is skewed toward the second quadrant ($R < 0$) relative to the first ($R > 0$), indicating that vortex stretching events are more frequent than vortex compression events. Finally, rare but intense biaxial strain events generate the heavy-tailed distribution along the right arm of the null-discriminant curve (Vieillefosse tail).

The normalization following Ooi et al. [56] using the ensemble average $\langle Q_W \rangle$, yields consistent PDFs that enable direct comparison with canonical turbulent flows. Only a slight widening of the teardrop topology toward more intermittent events is observed when the influence of the wall is removed by excluding near-wall points in the x-direction. The main differences are quantitative: the teardrop appears larger due to the normalization based on $\langle Q_W \rangle$, which decreases when the wall influence is excluded. This behavior is attributed to intense, localized vortical events near the wall, generated by strong shear, which contribute significantly to Q_W despite the predominantly strain-dominated character of the near-wall region.

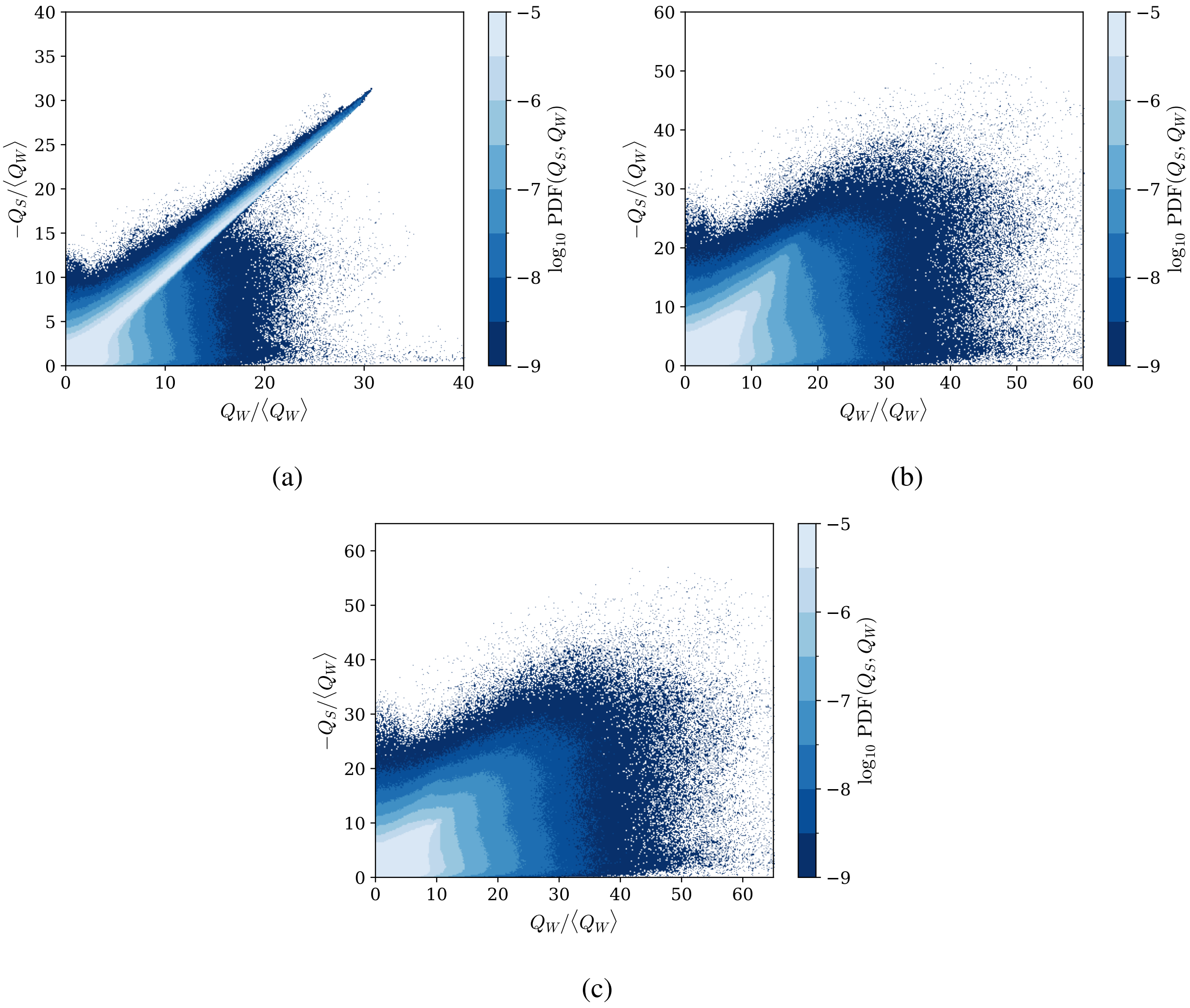

Figure 5.28: Joint PDF of $-Q_S$ and Q_W invariants normalized by $\langle Q_W \rangle$ on logarithmic scale for $Ra = 10^{10}$. The regions of interest corresponds to $\Omega_{\text{ROI}} = [0.001,\, 0.110] \times [0.005,\, 0.25] \times [0.65,\, 0.95]$ (a), $[0.003,\, 0.110] \times [0.005,\, 0.25] \times [0.65,\, 0.95]$ (b), and $[0.003,\, 0.110] \times [0.005,\, 0.25] \times [0.65,\, 0.95]$ (c).

The joint PDF of the Q_S and Q_W invariants is exhibited in Figure 5.28 on a logarithmic scale for $Ra = 10^{10}$. In this case, the influence of the wall plays a dominant role in shaping the flow topology, as evidenced by the pronounced tendency toward $-Q_S \approx Q_W$, which corresponds to a vortex sheet topology. When near-wall points are excluded in the x-direction, the flow transitions from a shear-dominated regime to a topology more consistent with canonical fully turbulent behavior. Nevertheless, a significant wall influence persists even at $x > 0.005$, indicating a stronger impact of the vertical boundary layer compared to other configurations, such as Rayleigh–Bénard convection

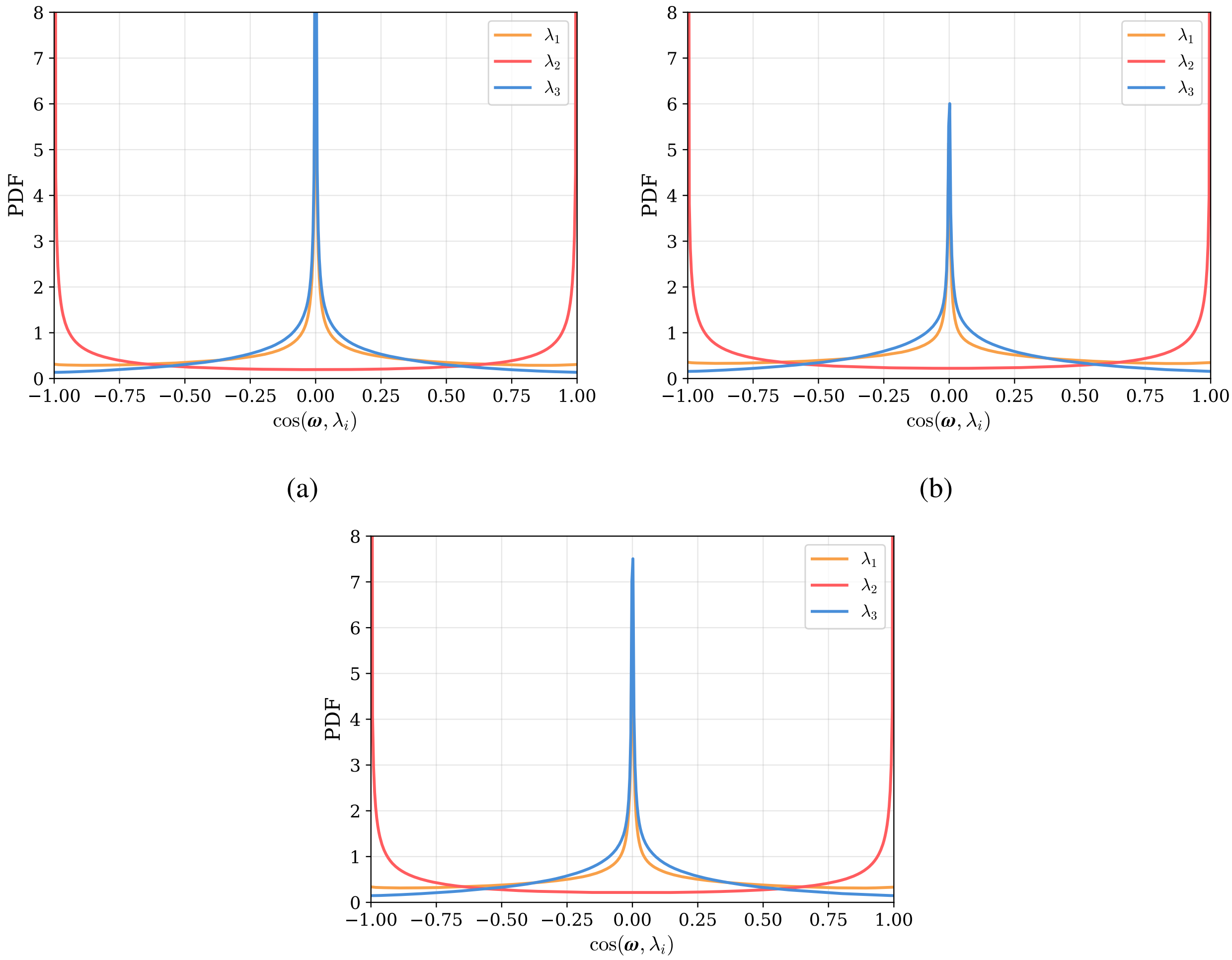

Figure 5.29: PDF of the vorticity alignment with the eigenvectors of the rate-of-strain tensor S for $Ra = 10^{10}$. The regions of interest corresponds to $\Omega_{\text{ROI}} = [0.001,\ 0.110] \times [0.005,\ 0.25] \times [0.65,\ 0.95]$ (a), $[0.003,\ 0.110] \times [0.005,\ 0.25] \times [0.65,\ 0.95]$ (b), and $[0.003,\ 0.110] \times [0.005,\ 0.25] \times [0.65,\ 0.95]$ (c).

[49]. Furthermore, regions of high Q_W and low $-Q_S$ are observed, indicating locally high enstrophy with negligible dissipation, where rotational motions dominate over strain. This further suggests a predominance of tube-like vortical structures in regions distal to the wall.

The probability density function of the vorticity alignment with the eigenvectors of the rate-of-strain tensor S is displayed in Figure 5.29 for $Ra = 10^{10}$. The well-known universal feature of three-dimensional turbulence, the preferential alignment between vorticity and the intermediate eigenvector of λ_2, is clearly observed, with sharp peaks at $\cos(\boldsymbol{\omega}, \lambda_2) = \pm 1$. As a direct geometric consequence, the most compressive eigenvector λ_3 is found to be nearly perpendicular to $\boldsymbol{\omega}$, yielding a sharp peak at $\cos(\boldsymbol{\omega}, \lambda_3) = 0$, while the most extensional eigenvector (λ_1) exhibits a slightly less perpendicular alignment. The pronounced sharpness of these distributions, compared to those reported in isotropic turbulence and Rayleigh-Bénard convection [49], is attributed to the combined effect of the near-wall flow organization and the persistent large-scale circulation inherent to the differentially heated cavity, both of which coherently orient the vorticity field and reinforce the preferential alignment throughout the domain.

Once again, since the number of samples per bin varies across the plots as different wall-normal regions are excluded, the results must be interpreted qualitatively rather than quantitatively when analyzing the influence of the wall. As expected, removing the points closest to the wall ($x < 0.003$) results in less sharp peaks at $\cos(\boldsymbol{\omega}, \boldsymbol{\lambda}_i) = 0$, confirming that the near-wall flow organization is partially responsible for the pronounced alignment. However, it should be noted that further excluding the region $0.003 \leq x < 0.005$ yields unexpectedly sharper peaks; this is likely a statistical artifact arising from the reduced number of samples in the tails of the distribution rather than a physical effect.

5.2.7 Coherent Structures Visualization

Coherent structures are fundamental elements in the study of turbulence; however, their dynamics and role in complex configurations such as the DHC remain an area of active research. For the visualization of these structures, the Q-criterion is employed. Figure 5.30 shows snapshots of isosurfaces at $Q = 40$, corresponding to regions where vorticity dominates over strain, within the region of interest $\Omega_{\text{ROI}} = [0.001, 0.110] \times [0.005, 0.25] \times [0.65, 0.95]$, colored by the vertical velocity w. The panels illustrate two distinct bursting processes: the top panels (a) and bottom panels (b) show structures being ejected from the hot vertical boundary layer into the cavity core, with a time separation of 10 time units between the two sequences. Each bursting process is shown at three consecutive instants separated by 0.5 time units (left to right).

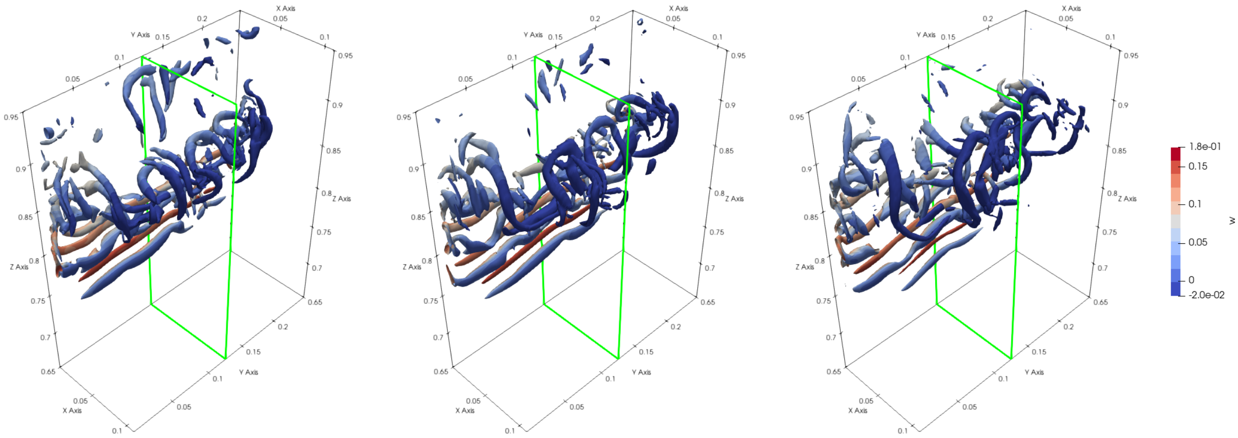

(a)

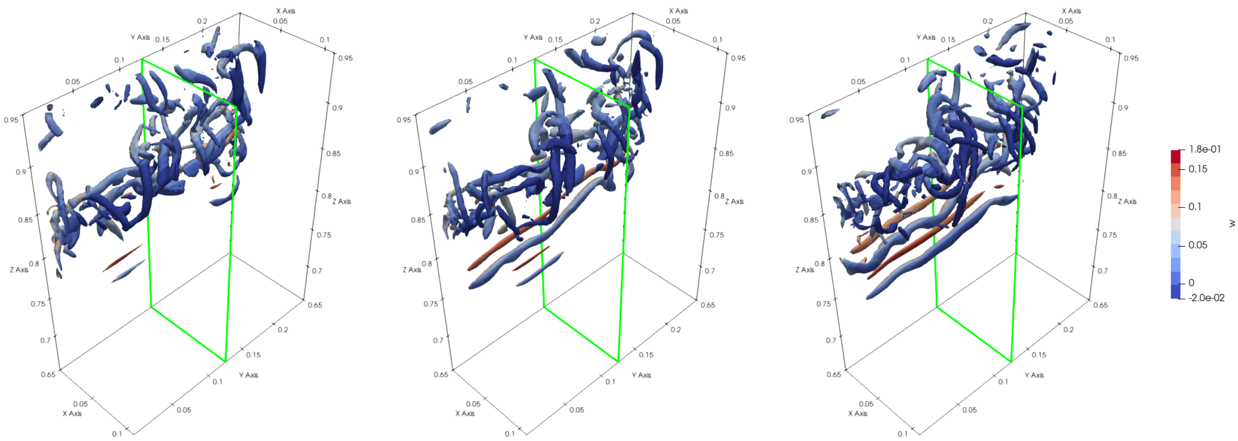

(b)

Figure 5.30: Visualization of structure ejection from the hot vertical boundary layer using Q-criterion isosurfaces at $Q = 40$ colored by the vertical velocity w. $Ra = 10^{10}$. From left to right, panels are separated by time increments of 0.5 time units, while the lower row (b) is offset from the upper row (a) by 10 time units. The region of interest is defined as $\Omega_{\text{ROI}} = [0.001, 0.110] \times [0.005, 0.25] \times [0.65, 0.95]$. The green lines delineate the boundaries of the plane $y = 0.125$.

The presence of stable tube-like vortices, which account for the skewness of the "teardrop shape" in the joint PDF of the Q–R invariants (see Figure 5.27), is clearly visible. Near the wall, very elongated tube-like structures are observed, often appearing in pairs with opposite signs of vertical velocity. However, the interpretation of near-wall structures using the Q-criterion must be treated with caution, as this method can be susceptible to contamination by strong shear [64].

Furthermore, structures resembling hairpin vortices are identified originating within the vertical boundary layer. These structures are transported upward along the wall until approximately $z = 0.85$, where they are stretched and ejected into the bulk of the cavity. Following ejection, they continue to undergo stretching until becoming sufficiently elongated, after which they are rapidly dissipated by viscous effects. This reflects a surprisingly intense dissipation activity in the bulk region immediately adjacent to the boundary layer. This ejection process is observed to occur periodically, with a recurrence time of approximately 10 time units. The robustness of these observations was validated by computing isosurfaces using the λ_2 criterion, enstrophy, and the Ω criterion, all of which yielded consistent topological results.

5.3 Local Analysis of Fully Turbulent Flow

5.3.1 Stationarity Test and Velocity PDF

The z-component of the velocity field exerts the most significant influence on the turbulence dynamics, as it contributes to the bulk of the turbulent kinetic energy. Fluctuations in this component arise directly from the mechanisms that sustain turbulence, such as Tollmien–Schlichting waves and buoyancy. Therefore, the signals of w are processed using the open-source package developed by Fuchs et al. [58] to locally investigate the turbulence inside the cavity. Two regions of interest are considered: the location of maximum fluctuations and the cavity core. Based on the distributions shown in Figure 5.18 and 5.21, the chosen monitoring points for the analysis are $C(x, y, z) = (0.125,\ 0.125,\ 0.5)$, $D(x, y, z) = (0.02,\ 0.125,\ 0.85)$, and $E(x, y, z) = (0.02,\ 0.1875,\ 0.85)$.

Although the large-scale flow in the DHC is inherently anisotropic due to the confining walls and the large-scale circulation, the application of HIT-based analysis at the selected monitoring points is partially justified by Kolmogorov's local isotropy hypothesis [26]. This hypothesis suggests that small-scale motions tend toward isotropy at sufficiently high Reynolds numbers, regardless of large-scale anisotropy. It is, however, acknowledged that the flow exhibits significant anisotropy at the large scales, as evidenced by the TKE component ratios $\overline{u'u'}/\overline{w'w'} \approx 0.6$ and $\overline{v'v'}/\overline{w'w'} \approx 0.4$, which

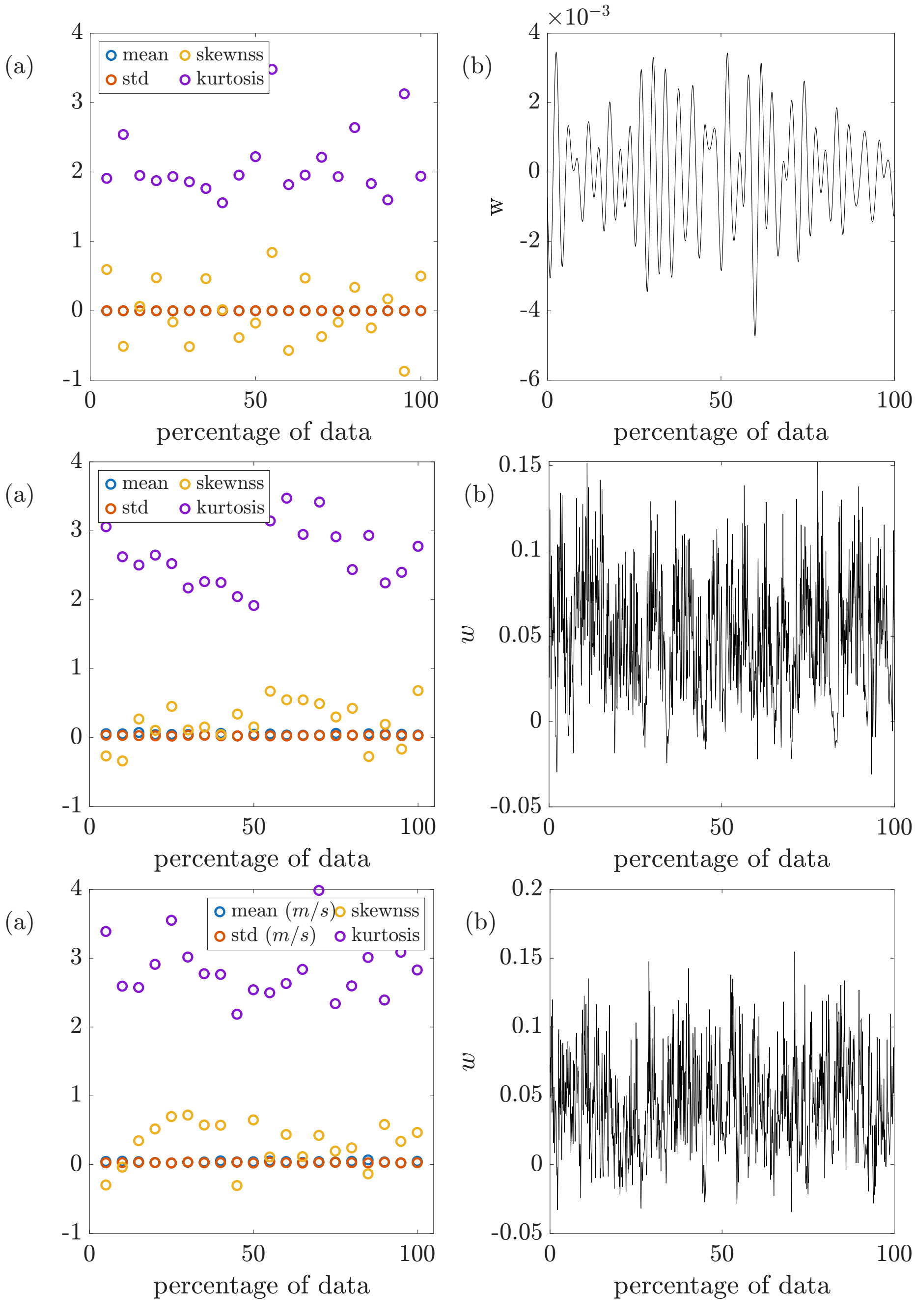

Figure 5.31: For fixed subdivisions, the mean, standard deviation, skewness, and kurtosis of the vertical velocity signals for $Ra = 10^{10}$ are plotted on the left, and the complete data itself is plotted on the right. From top to bottom: Monitoring points C, D, and E.

reflect the dominant role of the buoyancy-driven vertical velocity component. The HIT framework is therefore employed as a theoretical reference rather than an exact description of the flow, and the derived length scales should be interpreted within this context.

The signals are first tested for stationarity. The mean, standard deviation, skewness, and kurtosis are computed over fixed time subdivisions and presented in the left panels of Figure 5.31. All statistical moments remain within a consistent range of values throughout the signal, with no systematic temporal drift observed, suggesting that the flow has reached a statistically stationary state. The kurtosis, which is particularly sensitive to extreme events, exhibits slightly larger fluctuations than the lower-order moments, a common feature in turbulent signals where intermittency is present. A longer averaging window would be expected to further reduce these fluctuations.

The right panels of Figure 5.31 display the full time series of each signal, confirming the absence of outliers or anomalous events that could undermine the stationarity assumption. Furthermore, the chaotic nature of the signals of the monitoring points D and E relative to point C is clearly visible. Finally, the probability density function (PDF) of the vertical velocity is plotted for each monitoring point and compared to a Gaussian distribution with the same mean and standard deviation, as shown in Figure 5.32. The data closely follow the normal distribution, which is consistent with the near-Gaussian behavior of the velocity fluctuations expected in the bulk region of turbulent flows.

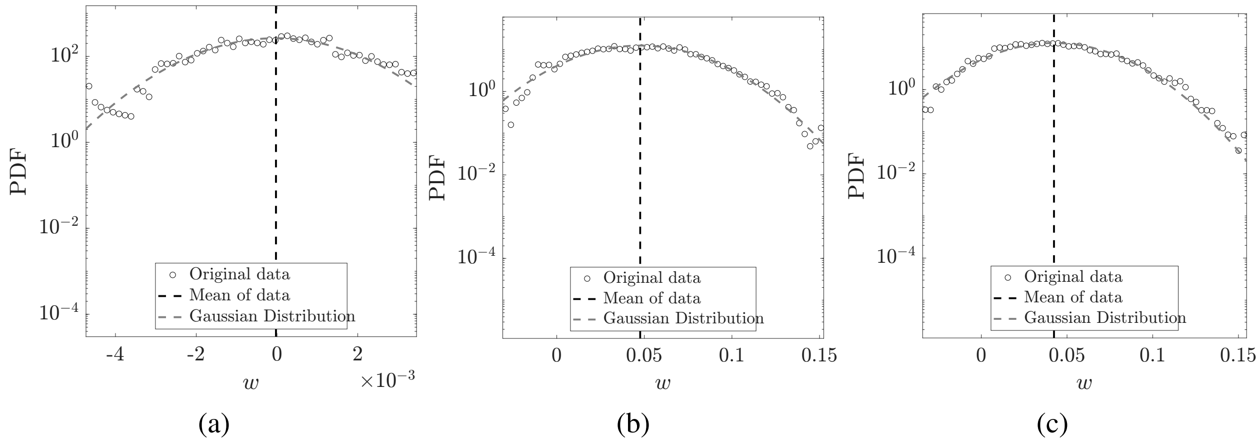

Figure 5.32: Vertical velocity probability density functions for monitoring points (a) C, (b) D, and (c) E. $Ra = 10^{10}$. The gray dashed line corresponds to a Gaussian distribution with the same standard deviation and mean value (vertical black dashed line) as the data.

5.3.2 Energy and Dissipation Spectra

The energy spectral density (ESD) is computed by first removing the mean from the signal and then applying a Fast Fourier Transform (FFT) to convert it from the time domain to the frequency domain. The squared magnitude of the FFT is then normalized by the signal length and sampling frequency to obtain the energy distribution across frequencies. Finally, only the positive frequencies are kept and scaled appropriately to account for symmetry, resulting in the one-sided ESD. Additionally, the spectrum is smoothed by grouping nearby frequency points into logarithmically spaced intervals and replacing each group with its average value. For each interval, both the frequency and the spectral energy are averaged, effectively reducing noise while preserving the overall spectral trend. The results for each monitoring point are shown in Figure 5.33.

The ESD at the cavity center (monitoring point C) is strongly dominated by frequencies in the range $0.076 \leq f \leq 0.137$, with the latter marking the energy peak, beyond which a sharp spectral cutoff is observed. This is consistent with the oscillatory behavior of the cavity core driven by the Brunt–Väisälä frequency $N = 0.134$, computed from a mean vertical temperature gradient $\partial\bar{\theta}/\partial z = 1.004$ and Prandtl number $Pr = 0.71$ (see Equation 2.1). The close agreement between the dominant spectral peak at $f = 0.137$ and N identifies the oscillation as an internal gravity wave sustained by the stable stratification of the core region, consistent with the interpretation of Trias [23]. A secondary peak (much smaller than the primary one) is also observed near $f \approx 2N$. Furthermore, the high-energy sub-peak frequencies $f < N$ present in the spectrum coincide with those associated with the periodic ejection of coherent structures from the vertical boundary layers discussed in subsec-

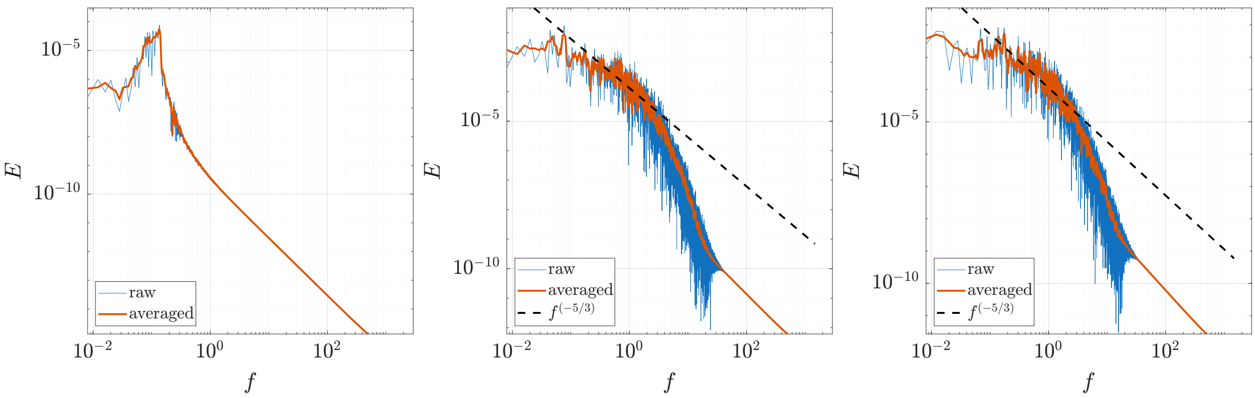

(a) (b) (c)

Figure 5.33: Energy spectral density in the frequency domain for monitoring points (a) C, (b) D, and (c) E. $Ra = 10^{10}$. The red solid line corresponds to the averaged energy spectral density in the frequency domain. The black dashed line (if present) corresponds to Kolmogorov's $f^{-5/3}$ prediction.

tion 5.2.7, suggesting that the internal wave field is forced by this boundary-layer mechanism. This aligns with the dispersion relation for internal gravity waves [65]:

$$\omega = N \cos \theta, \tag{5.1}$$

where θ is the angle between the direction of wave propagation and the vertical. This relation requires the forcing frequency to satisfy $\omega \leq N$. The sharp cutoff at $f = N$ is a direct consequence of this relation; since no real propagating solutions exist for $\omega > N$, waves with frequencies exceeding the Brunt–Väisälä frequency become evanescent and cannot propagate in the stratified medium. The internal gravity wave peak dominates the local energy budget by several orders of magnitude over the broadband turbulent background, confirming that the cavity center is isolated from the boundary-layer production regions that sustain the turbulent cascade. Nevertheless, a clear power-law decay is observed for $f \gtrsim 1$, indicating that turbulent fluctuations are present but energetically subordinate to the wave motion.

The ESDs at monitoring points D and E exhibit a more classical broadband turbulent character. A reference $f^{-5/3}$ slope is included in Figure 5.33 to identify the inertial range. Although limited in extent, a well-defined inertial range is discernible, confirming the turbulent nature of the flow at these locations. Both spectra display small peaks at frequencies consistent with those of the coherent-structure ejection events identified at the injection scales, indicating the direct imprint of the boundary-layer forcing on the bulk turbulence. Additionally, point D exhibits a secondary peak near the Brunt-Väisälä frequency $N = 0.134$, suggesting that the influence of the stratified core and its associated internal gravity wave field extend laterally beyond the cavity center.

As a precautionary measure, a low-pass filter was applied to all monitoring points using the Nyquist frequency $f_N = f/2$ as the cutoff, where f is the sampling rate; this represents the highest frequency that can be faithfully reconstructed without aliasing. Since no significant numerical noise is observed across the frequency range of interest, the filter produces no appreciable change in the spectra, verifying the quality of the DNS signal. A residual spectral tail is observed beyond $f \approx 300$, well within the dissipation range where no physical structures are expected to survive. The energy levels in this region are extremely low ($E \lesssim 10^{-13}$), several orders of magnitude below any dynamically relevant content, and are attributed to finite-precision round-off accumulation inherent to the DNS. This tail carries negligible energy and has no effect on any physically meaningful quantity derived from the spectra.

Figure 5.34 shows the energy spectral density (upper panels) and the dissipation spectral density

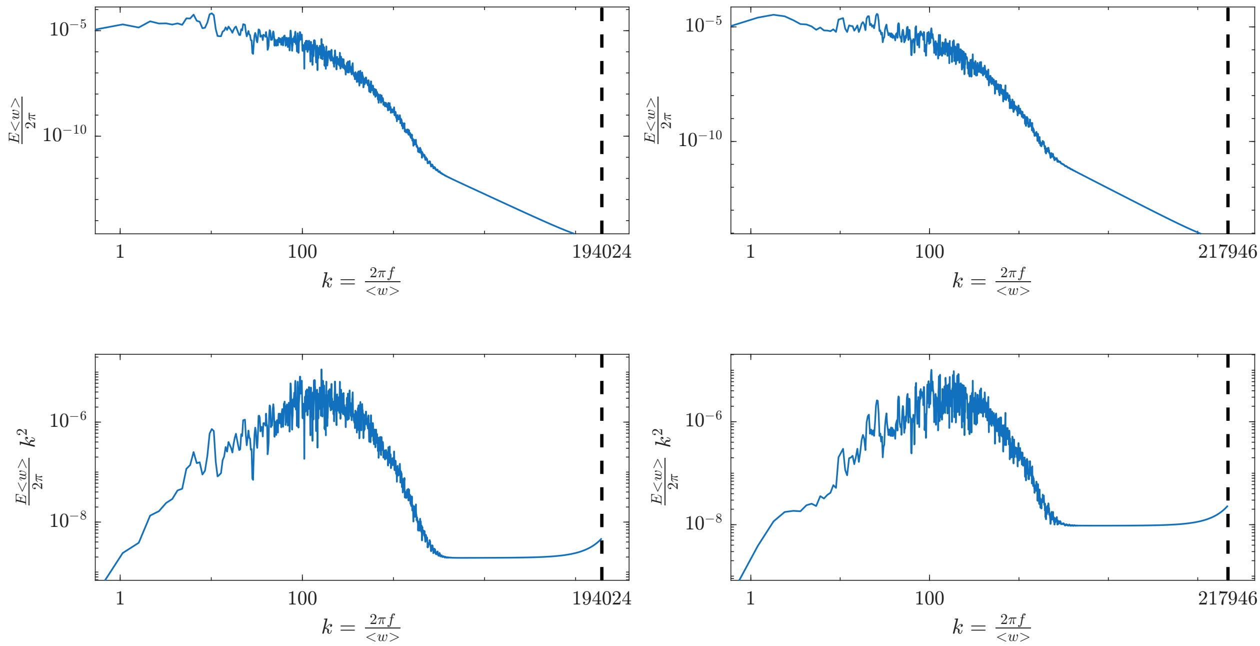

Figure 5.34: Energy spectral density (upper panels) and dissipation spectral density (lower panels) with respect to wave number k. $Ra = 10^{10}$. Left and right panels correspond to monitoring points D and E, respectively. The vertical dashed lines indicate the low-pass filter frequency (Nyquist frequency) in the wave number domain.

$k^2E(k)$ (lower panels) as functions of wavenumber k for monitoring points D and E. The conversion from frequency to wavenumber, $k = 2\pi f/\langle w\rangle$, is performed via Taylor's frozen turbulence hypothesis [66]. This conversion was not applied to monitoring point C, where the mean vertical velocity $\langle w\rangle$ is negligibly small, rendering Taylor's hypothesis invalid. The dissipation spectra exhibit well-defined peaks near $k \approx 160$ and $k \approx 105$ for monitoring points D and E, respectively. Beyond these peaks, the spectra decay rapidly and drop by several orders of magnitude well before their respective grid cutoff wavenumbers (dashed lines), demonstrating that the dissipative scales are adequately resolved by the DNS. A spurious upturn is observed in both dissipation spectra at $k \gtrsim 10^4$, which is attributed to the processing method utilized or finite-precision round-off accumulation inherent to the DNS, consistent with the spectral tail identified at energy levels $E \lesssim 10^{-13}$. As this feature carries negligible energy, it has no impact on any physically meaningful quantity derived from the spectra.

5.3.3 Characteristic Scales

Using the analytical methods offered in the open-source package [58], the characteristic length scales of turbulence are calculated for monitoring points D and E, where the requirements of the underlying

Table 5.3: Integral scale, Taylor scale, Reynolds number based on the Taylor scale, mean viscous dissipation rate, and Kolmogorov scale for monitoring points D and E. $Ra = 10^{10}$.

Monitoring point	l	λ	Re_λ	$\langle \varepsilon \rangle$	η
D	2.8×10^{-2}	7.8×10^{-3}	34.9	6.3×10^{-4}	8.7×10^{-4}
E	2.3×10^{-2}	4.9×10^{-3}	21.4	7.0×10^{-4}	8.5×10^{-4}

hypotheses are sufficiently met. The median of the values obtained is chosen as the most representative length scale; results are presented in Table 2.1. The flow exhibits a well-defined multiscale structure with adequate separation, approximately one order of magnitude, between the integral, Taylor, and Kolmogorov scales, indicating an active energy cascade. The integral scale l is observed to be of the order of the boundary layer thickness. The effect of the spanwise position between the two points is more noticeable in the Taylor microscale values. The smaller value obtained for point E may be attributed to its proximity to the rear no-slip wall, which increases the magnitude of the velocity gradients (reducing λ) and attenuates the vertical velocity fluctuations (reducing Re_λ). The Taylor-scale Reynolds numbers of 34.9 and 21.4 for monitoring points D and E, respectively, indicate that the flow is turbulent but has not reached the fully developed regime in which an inertial cascade is present but limited in extent. This is consistent with the energy spectral density plot in Figure 5.33, where the identified inertial range is indeed narrow.

The mean viscous dissipation rate is of the same order at both monitoring points, indicating a relatively uniform distribution of dissipative activity. A slightly higher value is observed near the wall (point E), consistent with the enhanced velocity gradients induced by the no-slip boundary condition. Kolmogorov microscale values (η) are found to be 8.7×10^{-4} and 8.5×10^{-4}, based on the mean dissipation rate, for monitoring points D and E, respectively. The similarity of these values suggests that the dissipative scales are largely independent of the large-scale inhomogeneity, supporting the local universality hypothesis.

These length scale estimates should be regarded as order-of-magnitude approximations. Specifically, the validity of Taylor's frozen-turbulence hypothesis is limited here: the turbulence intensity,

$$Ti = \frac{\sigma}{\langle w \rangle}, \tag{5.2}$$

where σ is the standard deviation and $\langle w \rangle$ is the mean vertical velocity, reaches values of 0.67 and 0.74 for points D and E, respectively. These values exceed the ideal $Ti \ll 1$ condition, which is known to stretch the range of validity for the hypothesis.

To verify these estimates independently, the mean dissipation rate was also computed directly from the velocity gradients presented in Figure 5.23. This yields $\varepsilon = 5.1 \times 10^{-3}$, resulting in a Kolmogorov scale of $\eta = 5.1 \times 10^{-4}$, in satisfactory agreement with the signal-based estimates. While the maximum grid spacing reported in Table 4.2 might appear insufficient to fully resolve the smallest scales, the Kolmogorov scale varies significantly across the domain. At the cavity center, where the grid is coarsest, the local dissipation rate of $\varepsilon = 2.4 \times 10^{-7}$ yields $\eta = 6.1 \times 10^{-3}$, which is nearly double the maximum grid spacing $\Delta x_{\max} = 3.4 \times 10^{-3}$. Furthermore, at the turbulent monitoring points D and E, the maximum grid spacing $\Delta x_{\max} = 4.0 \times 10^{-4}$ remains below the corresponding local Kolmogorov scale. As reliable second-order statistics typically require capturing the bulk of the viscous dissipation, often achieved by resolving scales proportional to η [67], the spatial resolution is deemed adequate throughout the domain

Finally, the time scale of the smallest structures is approximately 9 nondimensional time units at both points, yielding a frequency of 0.111. This is significantly smaller than the acquisition frequency of 2000 ($\Delta t = 5 \times 10^{-4}$, confirming that the temporal resolution is also sufficient to capture the dynamics of the smallest resolved scales.

5.3.4 Boundary Layer Dynamics: Spectral Evolution and Flow Regimes

The vertical velocity signals are further studied to assess the transition through monoperiodic, quasiperiodic, and chaotic regimes within the vertical boundary layer. This study focuses on variations in the dominant frequency of the energy spectral density plots in the vicinity of the vertical velocity maxima at the wall-normal coordinate $x = 0.005$. The depth-wise coordinates are $y = 0.125$ and $y = 0.1875$, while the vertical locations range from $z = 0.05$ to 0.95 in increments of 0.1. The ESDs are presented in Figure 5.35.

At all heights, the averaged spectra exhibit a clean, steep power-law decay from approximately $f \approx 0.3$ to 1. The decay appears steeper than the classical Kolmogorov $-5/3$ inertial subrange, which is expected in a wall-bounded, buoyancy-influenced flow where the energy-containing motions are not fully isotropic and the turbulence has not reached a state of fully developed HIT.

The ESDs at the lower vertical positions ($z = 0.05$ and $z = 0.15$) exhibit a smooth and rapid roll-off from a narrow energy-containing range into an exponential-like decay, with no clearly identifiable dominant frequency. This behavior is attributed to the influence of the wall jets formed as the flow impinges on the vertical wall from the bottom, prior to the development of boundary layer instabilities. No significant depth-dependent differences are observed, except at $z = 0.15$, where a slightly steeper

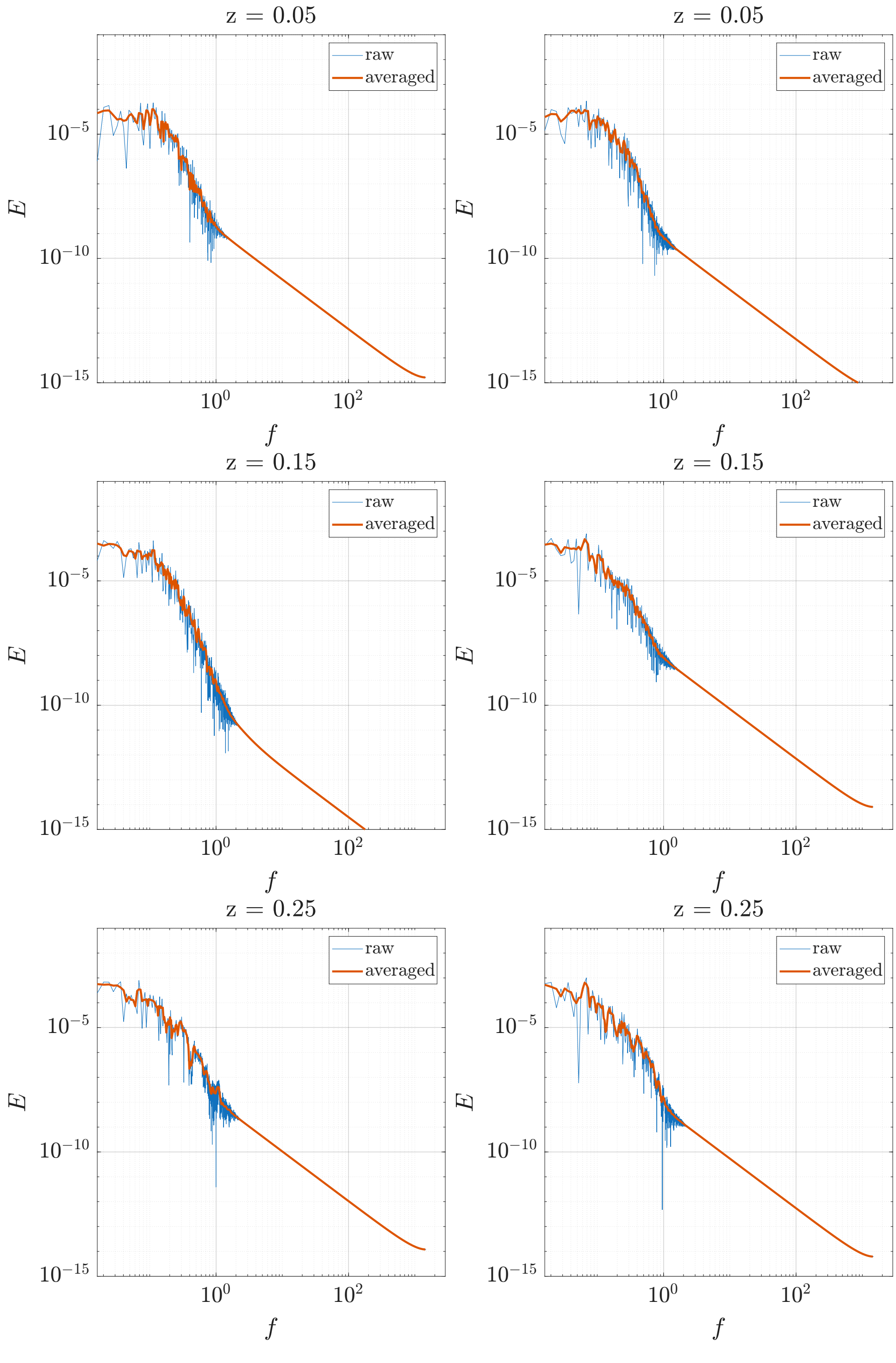

Figure 5.35: Energy spectral density in the frequency domain at $x = 0.005$, with $y = 0.125$ (left) and $y = 0.1875$ (right). The z-coordinate (indicated in the title of each panel) ranges from $z = 0.05$ to 0.95 in increments of 0.1. The red solid line corresponds to the averaged energy spectral density. $Ra = 10^{10}$. (continued on the next page).

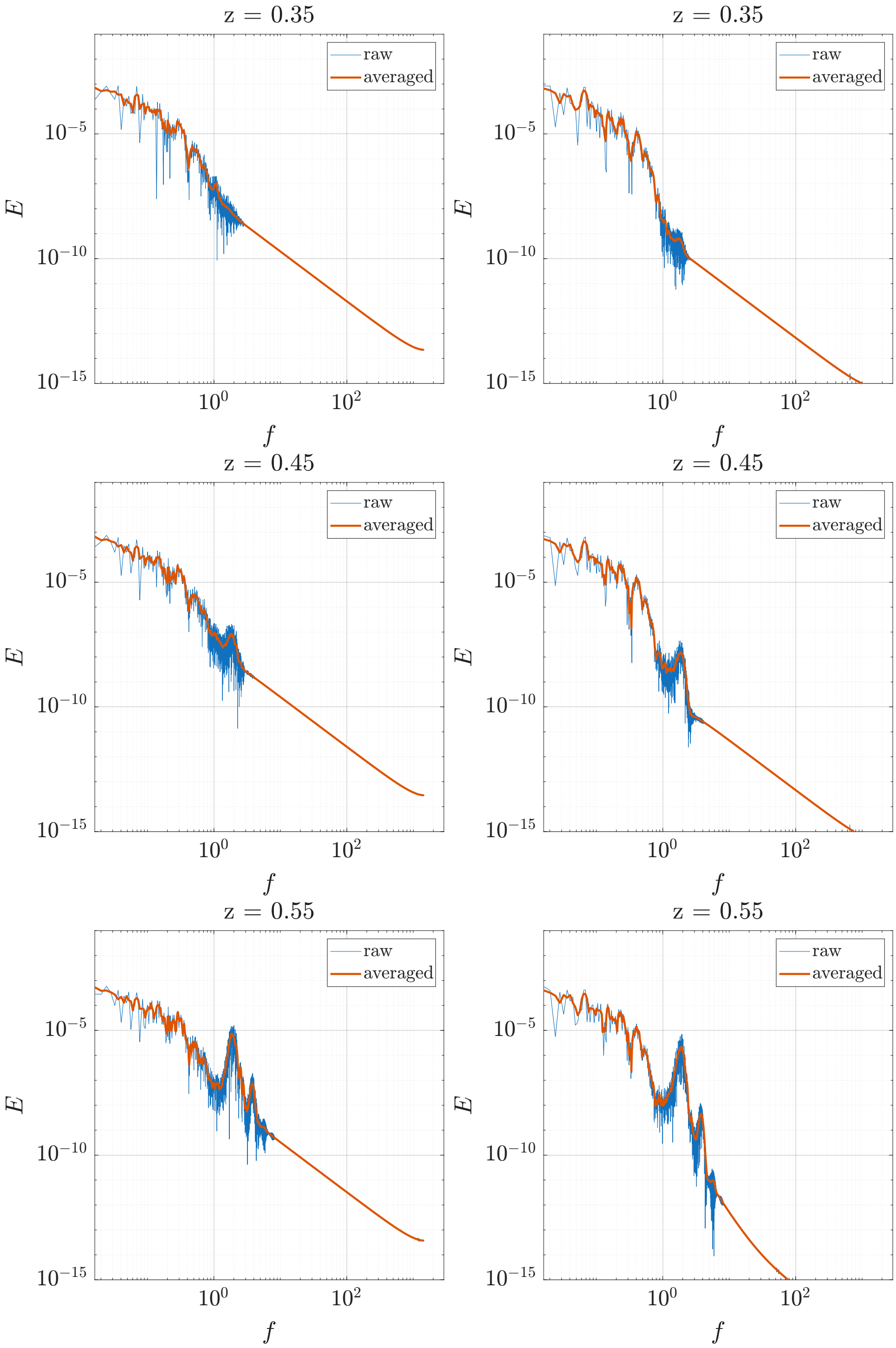

Figure 5.35: (continued)

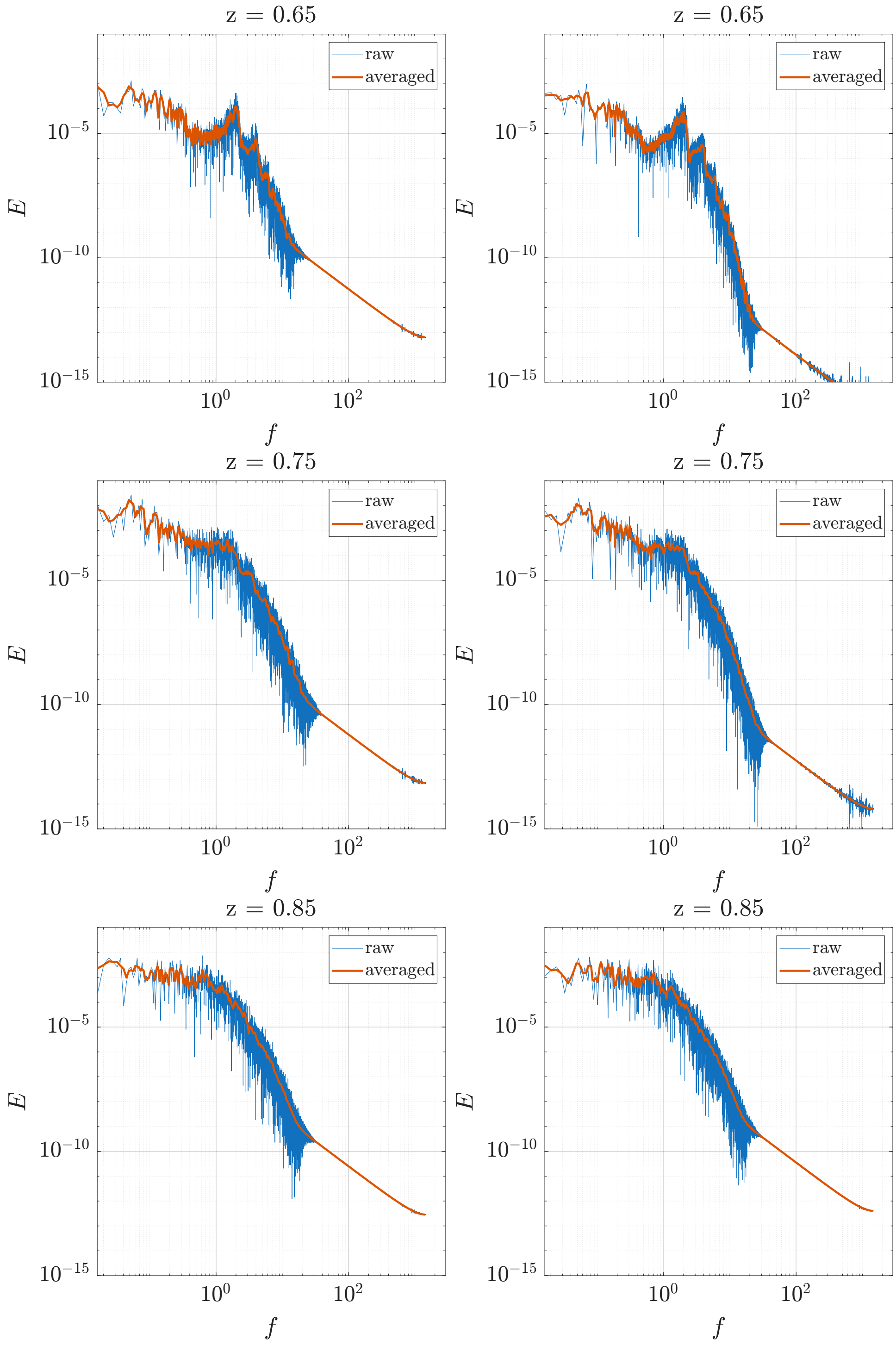

Figure 5.35: (continued)

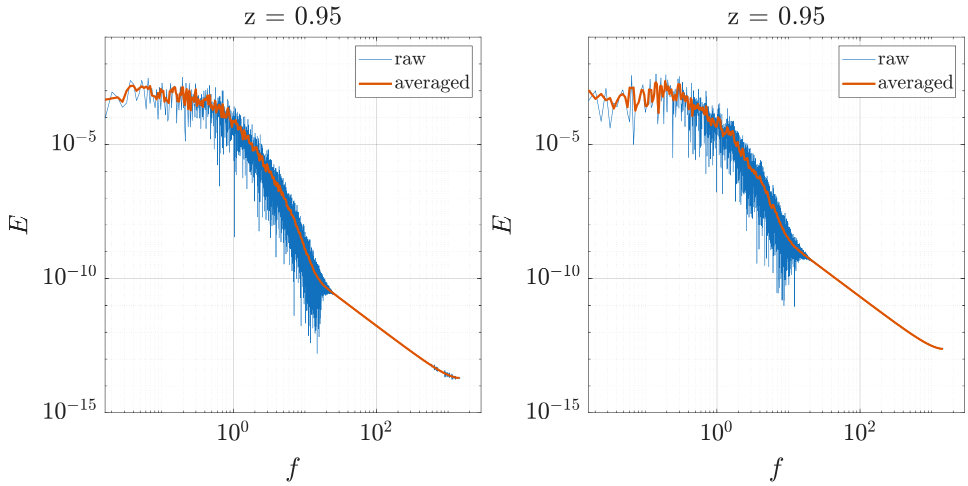

Figure 5.35: (continued)

slope is found for $y = 0.125$ compared to $y = 0.1875$ at higher frequencies ($f > 0.2$).

At $z = 0.25$, distinct spectral peaks emerge at approximately $f \in \{0.3, 0.47, 1.08\}$ for $y = 0.125$, and at $f \in \{0.3, 0.4, 1.86\}$ for $y = 0.1875$. Secondary peaks, likely representing harmonics of these fundamental frequencies, are also present. A low-frequency component around $f \approx 0.07$ is present at both depth locations. The magnitude of these peaks increases at $z = 0.35$, suggesting a transition toward a multimodal spectral state characterized by the coexistence of multiple discrete frequencies.

At mid-height positions ($z = 0.45$, 0.55, and 0.65), a peak at $f \approx 1.86$ becomes more pronounced for both spanwise coordinates, with its harmonics clearly visible. This signature points to a nonlinear regime dominated by a single frequency. Notably, this frequency is approximately four times the Tollmien–Schlichting wave frequency ($f_{\mathrm{TS}} \approx 0.47$) identified in subsection 5.1.2. The absence of a clearly resolved peak at f_{TS} itself may be due to reduced spectral resolution as frequencies approach the inverse of the sampling window.

At high-height locations ($z > 0.75$), the discrete peaks gradually vanish, being replaced by a broadband distribution characteristic of a chaotic signal. At $z = 0.85$ and $z = 0.95$, a limited inertial range is discernible, exhibiting a slope approaching Kolmogorov's $-5/3$ scaling.

The averaged spectra extend smoothly to high frequencies ($f \sim 10^2$), confirming that the DNS resolution adequately captures the dissipative scales. Spurious high-frequency tails ($f \sim 10^3$) observed at $y = 0.1875$ for vertical locations $z = 0.65$ and 0.75 are likely numerical noise; however, these carry negligible energy. Importantly, the consistency between peak locations in the raw and averaged spectra confirms that the dominant frequencies are reliably identified.

Chapter 6

Conclusions

This work investigated the turbulent convective flow in a three-dimensional differentially heated cavity of aspect ratio 4, employing no-slip boundary conditions at the front and rear walls. Direct numerical simulations were performed using the `Nek5000` spectral element solver. The objectives were to determine the critical Rayleigh number for the first bifurcation, characterize the turbulent regime, identify the mechanisms governing the generation and dissipation of coherent structures, and verify the role of Tollmien–Schlichting waves.

The analysis of the first Hopf bifurcation identified critical Rayleigh numbers of $Ra_c = 2.834 \times 10^8$ and $Ra_c = 2.840 \times 10^8$, significantly higher than the value reported for periodic boundary conditions [18]. This demonstrates the dissipative effect of the front and rear walls. Since these boundary conditions represent the physical behavior of real boundaries more closely, the results are more representative and enable more direct comparison with experimental observations.

For the turbulent case at $Ra = 10^{10}$, the mesh resolution was shown to adequately capture both the viscous sublayer and the Kolmogorov scales. The mean temperature field exhibited a vertical gradient of unity in close agreement with periodic-boundary results [11], indicating that discrepancies with experiments are unlikely due to boundary conditions and are more plausibly linked to thermal radiation effects. Consistently, the same Brunt–Väisälä frequency is obtained in the cavity core for both boundary condition approaches. Global heat transfer is slightly reduced compared to periodic boundary conditions, as reflected by the lower global Nusselt number at the hot wall [11], while remaining primarily governed by the main recirculation cell.

The flow does not exhibit a fully developed turbulent boundary layer, as indicated by the relatively low friction Reynolds number and the absence of a logarithmic region. A clear progression with increasing height is observed, from an apparent multimodal regime near the wall to a monoperiodic state that could be associated with Tollmien–Schlichting waves, and ultimately to fully turbulent behavior in the downstream region of the boundary layer. The monoperiodic state is dominated by a frequency approximately four times higher than that expected for TS waves. This discrepancy may reflect spectral aliasing or limitations in the time-series length, which may hinder the resolution of low-amplitude, high-frequency content embedded within the broadband turbulent background.

Turbulence is characterized by a region of high activity located in the boundary layer detachment region, where the vertical velocity component is the primary contributor to turbulent kinetic energy. In this region, the turbulent kinetic energy and the mean viscous dissipation rate are weakly correlated. The production of turbulence is dominated by shear, while buoyancy contributes at lower rates and locally acts as a sink in some regions. This high-activity region, despite exhibiting characteristic statistical signatures of turbulence, such as the teardrop morphology of the Q–R joint PDF, remains strongly influenced by wall effects, as evidenced by the PDFs of the Q_S and Q_W invariants and by the vorticity alignment with the eigenvectors of the rate-of-strain tensor. Spectral analysis at this location exhibits a classical broadband turbulent character; however, only a limited inertial subrange is observed, within which the Kolmogorov $-5/3$ slope can be identified. This, combined with a moderate Reynolds number based on the Taylor microscale, indicates that the flow is turbulent but has not reached the fully developed state with an extended energy cascade.

Coherent structures originate within the vertical boundary layer, are transported upward, and are periodically ejected into the cavity core, where they rapidly dissipate. The ejection location ($z \approx 0.83$) is consistent with the region of maximum Nusselt number variance. Spectral analysis further reveals internal gravity wave motion at the Brunt–Väisälä frequency within the stratified core, driven by the periodic ejection of these structures from the boundary layer.

Despite these findings, several methodological limitations remain. Thermal radiation was not considered, and its inclusion is likely necessary for precise quantitative agreement with experiments [20, 47]. The identification of the critical Rayleigh number may be affected by residual transients in the monitored signals, and longer integration times would further refine the bifurcation thresholds. Time-averaged statistics are computed over a finite interval, meaning that statistical convergence of the fields is not fully guaranteed, particularly for higher-order moments. The analysis of coherent structures focused primarily on large-scale ejection dynamics, and the interaction between structures of different sizes was not systematically examined, partly due to the known sensitivity of isosurface-based methods to the Q-criterion threshold. Finally, Taylor's frozen turbulence hypothesis and the local isotropy assumption are not strictly satisfied throughout the cavity: the former being questionable in the core, where the mean vertical velocity is near zero, and the latter given the anisotropy observed in the boundary layer, introducing uncertainties that should be borne in mind when interpreting the results. Proposed technical improvements include:

- **Consistency in initial conditions:** Using identical initial conditions across all cases would enable a more accurate comparison of temperature variance and transient evolution.
- **Objective vortex identification:** Implementing third-order methods such as Liutex or Rortex [64], which are threshold-independent, would remove the ambiguity associated with Q-criterion.
- **Statistical convergence:** Extending integration times for the turbulent case would improve the convergence of higher-order moments and enhance low-frequency spectral resolution.

This work opens several directions for future investigation. The analysis should be extended to higher Rayleigh numbers, such as $Ra = 3 \times 10^{10}$ and $Ra = 10^{11}$, and explore different aspect ratios to assess the generality of these findings. Incorporating thermal radiation modeling and a dedicated analysis of the thermal boundary layer structure remain key priorities.

The present results contribute to the understanding of turbulent natural convection in confined geometries, a configuration of both fundamental and practical relevance. The DNS dataset produced here provides a reference for the validation and development of turbulence models in buoyancy-driven flows, where standard closure models developed for shear-driven turbulence are known to perform poorly.

To conclude, a differentially heated cavity, however simple in geometry, represents a remarkably complex physical problem. This study constitutes a small step in the long journey toward understanding the mechanisms of turbulence: a challenge that continues to resist complete description. It is a puzzle that we must continue to pursue, slowly unraveling the mysteries that nature has quietly kept from us.

Bibliography

[1] L. Moosavi, N. Mahyuddin, N. Ab Ghafar, and M. Ismail, "Thermal performance of atria: An overview of natural ventilation effective designs," *Renew. Sustain. Energy Rev.*, vol. 34, pp. 654–670, 2014.

[2] H. Kim, B. An, J. Park, and K. Gong-Kwon, "Experimental study on natural convection heat transfer from horizontal cylinders with longitudinal plate fins," *J. Mech. Sci. Technol.*, vol. 27, pp. 593–599, 2013.

[3] O. Aydın, "Conjugate heat transfer analysis of double pane windows," *Build. Environ.*, vol. 41, no. 2, pp. 109–116, 2006.

[4] S. Amraqui, A. Mezrhab, and C. Abid, "Combined natural convection and surface radiation in solar collector equipped with partitions," *Appl. Sol. Energy*, vol. 47, pp. 36–47, 2011.

[5] J. Jeong and F. Hussain, "On the identification of a vortex," *J. Fluid Mech.*, vol. 285, pp. 69–94, 1995.

[6] P. Schmid, "Chapter Six - Data-driven and operator-based tools for the analysis of turbulent flows," in *Adv. Approaches Turbul.*, pp. 243–305, 2021.

[7] G. K. Batchelor, "Heat transfer by free convection across a closed cavity between vertical boundaries at different temperatures," *Q. Appl. Math.*, vol. 23, pp. 209–233, 1954.

[8] A. E. Gill, "The boundary-layer regime for convection in a rectangular cavity," *J. Fluid Mech.*, vol. 26, no. 3, pp. 515–536, 1966.

[9] A. Bejan, "Note on Gill's solution for free convection in a vertical enclosure," *J. Fluid Mech.*, vol. 90, no. 3, pp. 561–568, 1979.

[10] G. de Vahl Davis, "Natural convection of air in a square cavity: A benchmark numerical solution," *Int. J. Numer. Methods Fluids*, vol. 3, pp. 249–264, 1983.

[11] F. Trias, A. Gorobets, M. Soria, and A. Oliva, "Direct numerical simulation of a differentially heated cavity of aspect ratio 4 with Rayleigh numbers up to Ra = 10^{11}, Part I: Numerical methods and time-averaged flow," *Int. J. Heat Mass Transf.*, vol. 53, pp. 665–673, 2010.

[12] S. Paolucci and D. Chenoweth, "Transition to chaos in a differentially heated vertical cavity," *J. Fluid Mech.*, vol. 201, pp. 379–410, 1989.

[13] R. Janssen and R. Henkes, "Influence of Prandtl number on instability mechanisms and transition in a differentially heated square cavity," *J. Fluid Mech.*, vol. 290, pp. 319–344, 1995.

[14] P. Le Quéré and M. Behnia, "From onset of unsteadiness to chaos in a differentially heated square cavity," *J. Fluid Mech.*, vol. 359, pp. 81–107, 1998.

[15] P. Le Quéré, "Accurate solutions to the square thermally driven cavity at high Rayleigh number," *Comput. Fluids*, vol. 20, pp. 29–41, 1991.

[16] P. Le Quéré, "Onset of unsteadiness, routes to chaos and simulations of chaotic flows in cavities heated from the side: A review of present status," in *Proc. 10th Int. Heat Transfer Conf.*, vol. 1, pp. 281–296, 1994.

[17] S. Xin and P. Le Quéré, "Direct numerical simulations of two-dimensional chaotic natural convection in a differentially heated cavity of aspect ratio 4," *J. Fluid Mech.*, vol. 304, pp. 87–118, 1995.

[18] S. Xin and P. Le Quéré, "Stability of two-dimensional (2D) natural convection flows in air-filled differentially heated cavities: 2D/3D disturbances," *Fluid Dyn. Res.*, vol. 44, p. 031419, 2012.

[19] R. Gers, O. Skurtys, N. Thiers, F. Moreau, and D. Saury, "Three-dimensional effects induced by depth variation in a differentially heated cavity," *Phys. Fluids*, vol. 34, no. 9, p. 093602, 2022.

[20] W. Ting and L. Chengwang, "On numerical modelling of conjugate turbulent convection and radiation in a DHC," *Int. J. Heat Mass Transf.*, vol. 91, pp. 454–466, 2015.

[21] N. Thiers, "Influence of a thermal disturbance and flows induced by variations in depth in a differentially heated cavity flow," Ph.D. dissertation, Univ. Técnica Federico Santa María, Valparaíso, Chile, 2023.

[22] F. Charru, *Hydrodynamic Instabilities*, P. de Forcrand-Millard, Trans. Cambridge, U.K.: Cambridge Univ. Press, 2011, p. 13.

[23] F. X. Trias, M. Soria, A. Oliva, and C. D. Pérez-Segarra, "Direct numerical simulations of two- and three-dimensional turbulent natural convection flows in a differentially heated cavity of aspect ratio 4," *J. Fluid Mech.*, vol. 586, pp. 259–293, 2007.

[24] P. A. Davidson, *Turbulence: An Introduction for Scientists and Engineers*, 2nd ed. Oxford, U.K.: Oxford Univ. Press, 2015, pp. 57, 126, 260–269.

[25] L. F. Richardson, *Weather Prediction by Numerical Process*, 2nd ed. Cambridge, U.K.: Cambridge Univ. Press, 2007, p. 66.

[26] A. N. Kolmogorov, "The local structure of turbulence in incompressible viscous fluid for very large Reynolds numbers," *Dokl. Akad. Nauk SSSR*, vol. 30, pp. 299–303, 1941.

[27] C. Greenshields and H. Weller, "Notes on CFD: General principles," CFD Direct, Apr. 2022. [Online]. Available: `https://doc.cfd.direct/notes/cfd-general-principles/energy-cascade`. [Accessed: Nov. 11, 2025].

[28] J. Mathieu and J. Scott, *An Introduction to Turbulent Flow*. Cambridge, U.K.: Cambridge Univ. Press, 2000, pp. 61–68.

[29] A. Tsinober, *An Informal Conceptual Introduction to Turbulence*, 2nd ed. Dordrecht, Netherlands: Springer, 2009, pp. 127–128, 372–375.

[30] A. Alexakis and L. Biferale, "Cascades and transitions in turbulent flows," *Phys. Rep.*, vol. 767–769, pp. 1–101, 2018.

[31] H. Tennekes and J. L. Lumley, *A First Course in Turbulence*. Cambridge, MA, USA: MIT Press, 1972, pp. 95–96.

[32] K. R. Sreenivasan and R. A. Antonia, "The phenomenology of small-scale turbulence," *Annu. Rev. Fluid Mech.*, vol. 29, no. 1, pp. 435–472, 1997.

[33] G. K. Batchelor and A. A. Townsend, "The nature of turbulent motion at large wavenumbers," *Proc. R. Soc. Lond. A*, vol. 199, no. 1057, pp. 238–255, 1949.

[34] J. Jiménez, "Intermittency in turbulence," 2006.

[35] J. Jiménez, A. A. Wray, P. G. Saffman, and R. S. Rogallo, "The structure of intense vorticity in isotropic turbulence," *J. Fluid Mech.*, vol. 255, pp. 65–90, 1993.

[36] F. Belin, J. Maurer, P. Tabeling, and H. Willaime, "Observation of intense filaments in fully developed turbulence," *J. Phys. II France*, vol. 6, no. 4, pp. 573–583, 1996.

[37] P. K. Yeung, X. M. Zhai, and K. R. Sreenivasan, "Extreme events in computational turbulence," *Proc. Natl. Acad. Sci. U.S.A.*, vol. 112, no. 41, pp. 12633–12638, 2015.

[38] A. N. Kolmogorov, "A refinement of previous hypotheses concerning the local structure of turbulence in a viscous incompressible fluid at high Reynolds number," *J. Fluid Mech.*, vol. 13, no. 1, pp. 82–85, 1962.

[39] U. Frisch, P.-L. Sulem, and M. Nelkin, "A simple dynamical model of intermittent fully developed turbulence," *J. Fluid Mech.*, vol. 87, no. 4, pp. 719–736, 1978.

[40] C. S. Ng, A. Ooi, D. Lohse, and D. Chung, "Changes in the boundary-layer structure at the edge of the ultimate regime in vertical natural convection," *J. Fluid Mech.*, vol. 825, pp. 550–572, 2017.

[41] M. Gad-el-Hak and P. R. Bandyopadhyay, "Reynolds number effects in wall-bounded turbulent flows," *Appl. Mech. Rev.*, vol. 47, no. 8, pp. 307–365, 1994.

[42] C. Bosshard, A. Dehbi, M. Deville, E. Leriche, R. Puragliesi, and A. Soldati, "Large eddy simulation of the differentially heated cubic cavity flow by the spectral element method," *Comput. Fluids*, vol. 86, pp. 210–227, 2013.

[43] J. Jiménez, "Coherent structures in wall-bounded turbulence," *J. Fluid Mech.*, vol. 842, P1, 2018.

[44] A. K. M. F. Hussain, "Coherent structures and turbulence," *J. Fluid Mech.*, vol. 173, pp. 303–356, 1986.

[45] D. Gray and A. Giorgini, "The validity of the Boussinesq approximation for liquids and gases," *Int. J. Heat Mass Transf.*, vol. 19, no. 5, pp. 545–551, 1976.

[46] H. Mlaouah, T. Tsuji, and Y. Nagano, "A study of non-Boussinesq effect on transition of thermally induced flow in a square cavity," *Int. J. Heat Fluid Flow*, vol. 18, no. 1, pp. 100–106, 1997.

[47] M. Bouafia, S. Hamimid, and M. Guellal, "Non-Boussinesq convection in a square cavity with surface thermal radiation," *Int. J. Therm. Sci.*, vol. 96, pp. 236–247, 2015.

[48] A. Bejan, *Convection Heat Transfer*, 4th ed. Hoboken, NJ, USA: John Wiley & Sons, 2013, pp. 233–241.

[49] F. Dabbagh, F. X. Trias, A. Gorobets, and A. Oliva, “On the evolution of flow topology in turbulent Rayleigh–Bénard convection,” *Phys. Fluids*, vol. 28, no. 11, p. 115105, 2016.

[50] M. S. Chong, A. E. Perry, and B. J. Cantwell, “A general classification of three-dimensional flow fields,” *Physics of Fluids A*, vol. 2, no. 5, pp. 765–777, 1990.

[51] P. Fischer, J. Lottes, and S. Kerkemeier, “NEK5000: Open source spectral element CFD solver,” 2016. [Online]. Available: `http://nek5000.mcs.anl.gov`. [Accessed: Nov. 02, 2025].

[52] A. Patera, “A spectral element method for fluid dynamics: Laminar flow in a channel expansion,” *J. Comput. Phys.*, vol. 54, pp. 468–488, 1984.

[53] S. Pirozzoli and P. Orlandi, “Natural grid stretching for DNS of wall-bounded flows,” *J. Comput. Phys.*, vol. 439, p. 110408, May 2021.

[54] S. H. Strogatz, *Nonlinear Dynamics and Chaos: With Applications to Physics, Biology, Chemistry, and Engineering*, Boca Raton, FL, USA: CRC Press, Taylor & Francis Group, 2018, pp. 251–257.

[55] R. Vinuesa, L. Fick, P. Negi, O. Marin, E. Merzari, and P. Schlatter, “Turbulence statistics in a spectral element code: A toolbox for high-fidelity simulations,” OSTI OAI, U.S. Dept. Energy, Feb. 2017.

[56] A. Ooi, J. Martin, J. Soria, and M. S. Chong, “A study of the evolution and characteristics of the invariants of the velocity-gradient tensor in isotropic turbulence,” *Phys. Fluids*, vol. 11, no. 2, pp. 329–343, 1999.

[57] C. Liu, Y. Gao, X. Dong, Y.-Q. Wang, J. Liu, Y.-N. Zhang, X.-S. Cai, and N. Gui, “Third generation of vortex identification methods: Omega and Liutex/Rortex based systems,” *J. Hydrodynamics*, vol. 31, no. 2, pp. 205–223, 2019.

[58] A. Fuchs, S. Kharche, A. Patil, J. Friedrich, M. Wächter, and J. Peinke, “An open source package to perform basic and advanced statistical analysis of turbulence data and other complex systems,” *Phys. Fluids*, vol. 34, no. 10, Sep. 2022.

[59] J. Ke, N. Williamson, S. W. Armfield, and A. Komiya, “The turbulence development of a vertical natural convection boundary layer,” *J. Fluid Mech.*, vol. 964, A24, 2023.

[60] K. R. Maryada, S. W. Armfield, P. Dhopade, and S. E. Norris, “Large-scale motions in a turbulent natural convection boundary layer immersed in a stably stratified environment,” *J. Fluid Mech.*, vol. 967, A40, 2023.

[61] J. Kim, P. Moin, and R. D. Moser, "Turbulence statistics in fully developed channel flow at low Reynolds number," *J. Fluid Mech.*, vol. 177, pp. 133–166, 1987.

[62] C. J. Howland, C. S. Ng, R. Verzicco, and D. Lohse, "Boundary layers in turbulent vertical convection at high Prandtl number," *J. Fluid Mech.*, vol. 930, A40, 2021.

[63] F. Trias, A. Gorobets, M. Soria, and A. Oliva, "Direct numerical simulation of a differentially heated cavity of aspect ratio 4 with Rayleigh numbers up to Ra = 10^{11}, Part II: Heat transfer and flow dynamics," *Int. J. Heat Mass Transf.*, vol. 53, pp. 674–683, 2010.

[64] Y. Gao and C. Liu, "Rortex and comparison with eigenvalue-based vortex identification criteria," *Phys. Fluids*, vol. 30, no. 8, p. 085107, 2018.

[65] D. E. Mowbray and B. S. Rarity, "A theoretical and experimental investigation of the phase configuration of internal waves of small amplitude in a density-stratified fluid," *J. Fluid Mech.*, vol. 28, no. 1, pp. 1–16, 1967.

[66] G. I. Taylor, "The spectrum of turbulence," *Proc. R. Soc. Lond. A*, vol. 164, pp. 476–490, 1938.

[67] P. Moin and K. Mahesh, "Direct numerical simulation: A tool in turbulence research," *Annu. Rev. Fluid Mech.*, vol. 30, no. 1, pp. 539–578, 1998.

[68] M. Abramowitz and I. A. Stegun, *Handbook of Mathematical Functions with Formulas, Graphs, and Mathematical Tables*, 10th ed. Washington, DC, USA: National Bureau of Standards, 1972, pp. 331–341.

[69] O. Rodrigues, "De l'attraction des sphéroïdes," *Correspondence sur l'École Impériale Polytechnique*, vol. 3, no. 3, pp. 361–385, 1816.

[70] M. Atzori, S. Mirzareza, and A. G. Balasubramanian, "Solver stabilization," in *Nek5000: Theory, Implementation and Optimization*, FLOW–SESE Course 2021, KTH Royal Institute of Technology, Stockholm, Sweden, pp. 129–145, 2021.

[71] J. H. Bramble, "A proof of the inf–sup condition for the Stokes equations on Lipschitz domains," *Math. Models Methods Appl. Sci.*, vol. 13, no. 3, pp. 361–371, Mar. 2003.

[72] C. Canuto, M. Y. Hussaini, A. Quarteroni, and T. A. Zang, *Spectral Methods*, Berlin, Germany: Springer Science & Business Media, pp. 75–76, 220–524, 2007.

[73] I. C. F. Ipsen and C. D. Meyer, "The idea behind Krylov methods," *Amer. Math. Mon.*, vol. 105, no. 10, pp. 889–899, 1998.

[74] S. Kern, V. Lupi, and V. Kleine, “Iterative solvers and projection method,” in *Nek5000: Theory, Implementation and Optimization*, FLOW–SESE Course 2021, KTH Royal Institute of Technology, Stockholm, Sweden, pp. 59–70, 2021.

[75] D. Massaro, D. Xavier, and H. Eivazi, “Pressure preconditioning,” in *Nek5000: Theory, Implementation and Optimization*, FLOW–SESE Course 2021, KTH Royal Institute of Technology, Stockholm, Sweden, pp. 95–112, 2021.

Appendix A

Numerical Methodology

A.1 Discretization of Governing Equations

Since no general analytical solution exists for the governing equations, numerical simulation becomes essential for resolving the complexity of the flow. For clarity, the following derivation is presented in one dimension. The same procedure generalizes directly to two- and three-dimensional domains. Consider a system of the form:

$$\begin{cases} \mathcal{L}(v) = 0 \\ v|_{\Gamma} = v_0, \quad v : \Omega \to \mathbb{R}^n, \quad \Gamma \subset \partial\Omega \end{cases} \tag{A.1}$$

with its corresponding initial and boundary conditions, where $v(x,t)$ is the unknown function. A discrete approximation can be constructed by expanding the solution in a finite set of basis functions:

$$v_N(x,t) = \sum_{k=0}^{N} v_k(t)\phi_k(x), \tag{A.2}$$

where $v_k(t)$ are the expansion (interpolation) coefficients and $\phi_k(x)$ are the base functions. The choice of these trial functions defines the numerical method:

- **Finite Differences Method:** Characterized by pointwise support, typically utilizing the cardinal functions associated with the grid points:

$$\phi_k(x) = \delta(x - x_k) = \begin{cases} 1, & x = x_k \\ 0, & x \neq x_k. \end{cases} \tag{A.3}$$

- **Finite Volume Method (FVM) and Finite Elements Method (FEM):** Characterized by compact support. A representative example is:

$$\phi_k(x) = \begin{cases} 1, & x \in [x_k, x_{k+1}] \\ 0, & x \notin [x_k, x_{k+1}], \end{cases} \tag{A.4}$$

  Although in practice, FEM uses piecewise-polynomial basis functions and FVM employs control-volume indicator functions.

- **Spectral Method:** Characterized by global support. ϕ_k are typically trigonometric or orthogonal polynomials defined over the entire domain.

Each method provides distinct strategies for discretizing partial differential equations. Finite difference schemes are straightforward to implement and computationally efficient on structured grids, but they struggle with complex geometries and irregular boundaries. Finite element methods offer excellent geometric flexibility, rigorous variational foundations; however, they present certain limitations when implementing high-order schemes and they require more elaborate meshing and assembly procedures. Finite volume methods enforce local conservation laws by construction, making them well suited for fluid dynamics and hyperbolic problems, but they can be less accurate on highly irregular meshes unless carefully formulated. Spectral methods achieve extremely high accuracy for smooth solutions through global basis functions, yet their efficiency deteriorates in the presence of discontinuities or complicated geometries.

An attractive alternative is the Spectral Element Method, proposed by Patera [52], which combines the geometric flexibility of finite elements with the high-order accuracy of spectral approximations, providing an appealing compromise that delivers superior accuracy on complex domains while maintaining good computational efficiency.

A.1.1 Strong and Weak Formulations of Differential Equations

The equations in 3.8 are expressed in their strong form, meaning that the PDE must hold pointwise in the entire spatial domain and for all times. To obtain the corresponding weak form, one instead requires that the PDE be satisfied in an averaged sense over a suitable Sobolev space $\mathcal{H}_0^1(\Omega)$ of test functions. This is achieved by multiplying the governing equation by an arbitrary test function $\psi(x)$, integrating over the spatial domain Ω (at each time), and applying integration by parts where appropriate. For the system, $\mathcal{L}(v) = 0$ this corresponds to:

$$\iiint_{\Omega} \psi \mathcal{L}(v) dV = 0. \tag{A.5}$$

The weak form lowers the differentiability requirements on the solution, incorporates natural boundary conditions more cleanly, and provides a framework suitable for numerical methods. It is easily noted that $\mathcal{L}(v) = 0$ when v is the exact solution. For a numerical approximation v_N typically results in a residual $\mathcal{R} = \mathcal{L}(v_N)$. The objective is therefore to reduce the residual such that:

$$\iiint_{\Omega} \psi \, \mathcal{L}(v_N) \, dV = \iiint_{\Omega} \psi \, \mathcal{R} \, dV \approx 0. \tag{A.6}$$

In both the finite element and finite volume methods, the computational domain is partitioned into M subdomains Ω_m. This leads to

$$\iiint_{\Omega} \psi \, \mathcal{L}(v) \, dV = \sum_{m=1}^{M} \iiint_{\Omega_m} \psi_m \, \mathcal{L}(v) \, dV, \tag{A.7}$$

which allows the equations to be solved piece by piece over the domain. In particular, in the Galerkin method, the test function ψ is represented by the same set of trial functions ϕ_k:

$$\psi_k(x) = \phi_k(x). \tag{A.8}$$

Considering the inner product notation:

$$\int_{\Omega} f g \, d\Omega = (f, g)_{\Omega} \tag{A.9}$$

$$\oint_{\Gamma} f g \, n \, d\Gamma = (f, g)_{\Gamma}, \tag{A.10}$$

the governing equations (in one-dimensional form) can be rewritten in their weak form as:

$$
\begin{aligned}
(\psi, \nabla \cdot u)_\Omega &= 0, \\
\frac{\partial}{\partial t}(\psi, u)_\Omega + (\psi, u \cdot \nabla u)_\Omega &= -(\psi, p)_\Gamma + (\nabla\psi, p)_\Omega + \frac{Pr}{\sqrt{Ra}}\left\{(\psi, \nabla u)_\Gamma - (\nabla\psi, \nabla u)_\Omega\right\} \\
&\quad + Pr\,(\psi, \theta)_\Omega, \\
\frac{\partial}{\partial t}(\psi, \theta)_\Omega + (\psi, u \cdot \nabla\theta)_\Omega &= \frac{1}{\sqrt{Ra}}\left\{(\psi, \nabla\theta)_\Gamma - (\nabla\psi, \nabla\theta)_\Omega\right\}.
\end{aligned}
\tag{A.11}
$$

A.1.2 Choice of Basis Functions

The choice of basis functions plays a central role in determining the accuracy, stability, and efficiency of a numerical discretization. In the modal formulation, the basis functions are predefined and the unknowns are the expansion coefficients. In contrast, the nodal formulation uses the values of the solution at selected nodes as coefficients, requiring the basis to be constructed accordingly. Each approach offers distinct advantages and properties, motivating a careful selection of the basis functions used in the discretization.

Modal Basis: Legendre Polynomials

In the modal formulation, Legendre polynomials L_k are commonly employed due to their orthogonality and favorable convergence properties. These polynomials are solutions of the Legendre differential equation:

$$
\frac{d}{dx}\left[(1-x^2)\frac{dL_k}{dx}\right] + k(k+1)L_k(x) = 0, \quad x \in [-1, 1], \tag{A.12}
$$

where k is the polynomial degree. They can be obtained either recursively through the Bonnet's recursion formula [68]:

$$
(k+1)L_{k+1}(x) = (2k+1)xL_k(x) - kL_{k-1}(x), \quad L_0(x) = 1, \quad L_1(x) = x, \tag{A.13}
$$

or by using Rodrigues' formula [69]:

$$
L_k(x) = \frac{1}{2^k k!}\frac{d^k}{dx^k}\left[(x^2-1)^k\right]. \tag{A.14}
$$

Legendre polynomials are orthogonal with respect to the L^2 inner product

$$\int_{-1}^{1} L_k(x)L_m(x)\,dx = \frac{2}{2k+1}\delta_{km}, \tag{A.15}$$

which ensures that each mode contributes independently to the solution expansion.

Nodal Basis: Lagrange Polynomials

The nodal formulation often relies on Lagrange polynomials, which are constructed to take the value 1 at a specific node and 0 at all others. Given a set of $N+1$ nodes $\{x_i\}_{i=0}^{N}$ within the domain, the Lagrange polynomial associated with node x_j is defined as:

$$\ell_j(x) = \prod_{\substack{i=0 \\ i\neq j}}^{N} \frac{x - x_i}{x_j - x_i}. \tag{A.16}$$

By construction, these polynomials satisfy the nodal property $\ell_j(x_i) = \delta_{ij}$, which allows the solution to be represented directly by its values at the nodes:

$$u_N(x) = \sum_{j=0}^{N} u_j \ell_j(x), \tag{A.17}$$

where $u_j = u(x_j)$. Lagrange polynomials are particularly suitable for collocation and interpolation-based methods. Their main characteristics include the ability to exactly interpolate polynomials of degree up to N and the flexibility to choose non-uniform nodes (e.g., Gauss–Lobatto or Chebyshev points) to improve stability and reduce Runge's phenomenon at higher degrees.

In particular, Gauss–Lobatto–Legendre (GLL) collocation points are obtained by finding the $N+1$ roots of the polynomial $(1-x^2)\,L'_N(x)$, where L'_N is the derivative of the Legendre polynomial of order N. When the nodes coincide with the GLL points, the nodal basis functions also become orthogonal with respect to the discrete inner product defined at these nodes. This effectively reproduces the orthogonality properties of modal expansions, thereby enhancing both the accuracy and numerical stability of the method.

A.2 Nek5000 Numerical Framework

A.2.1 Spectral Element Formulation

The Navier–Stokes equations are reformulated in the weak form using a Galerkin projection for each spectral element, with test and trial functions selected from distinct polynomial spaces. Because the use of a collocated grid for pressure and velocity can result in spurious coupling modes [70], a $P_N - P_{N-2}$ formulation is utilized. In this framework, the velocity and temperature fields are approximated using Nth-degree Lagrange interpolants defined at Gauss–Lobatto–Legendre quadrature points, while the pressure field is approximated with $(N-2)$th-degree Lagrange interpolants defined at Gauss–Legendre quadrature points. Consequently, Equation A.11 can be rewritten as:

$$
\begin{aligned}
(\psi, \nabla \cdot u)_{GLL} &= 0, \\
\frac{\partial}{\partial t}(\psi, u)_{GLL} + (\psi, u \cdot \nabla u)_{GLL} &= (\nabla \psi, P)_{GL} + \frac{Pr}{\sqrt{Ra}}\Big[(\psi, \nabla u)_{GLL,\Gamma} - (\nabla \psi, \nabla u)_{GLL}\Big] \\
&\quad + Pr\,(\psi, \theta)_{GLL,\Gamma}, \\
\frac{\partial}{\partial t}(\psi, \theta)_{GLL} + (\psi, u \cdot \nabla \theta)_{GLL} &= \frac{1}{\sqrt{Ra}}\left\{(\psi, \nabla \theta)_{GLL,\Gamma} - (\nabla \psi, \nabla \theta)_{GLL}\right\}.
\end{aligned}
\tag{A.18}
$$

The subscripts GLL and GL denote integrations computed using Gauss–Lobatto–Legendre and Gauss–Legendre quadratures, respectively. This scheme satisfies the Inf-Sup or Ladyzhenskaya–Babuška–Brezzi condition, spurious modes in the pressure field [71, 52]. A significant implication of the $P_N - P_{N-2}$ formulation is that the Gauss–Legendre basis used for the pressure field contains no quadrature points on the boundaries of the spectral elements. Consequently, the pressure is not constrained to be continuous across element interfaces and possesses no boundary degrees of freedom. This property eliminates the need for explicit boundary conditions for the pressure Poisson equation, as the formulation naturally accommodates a discontinuous pressure field. This explains why the boundary contribution from the pressure term in the continuous weak formulation (Equation A.11) vanishes upon discretization. In this framework, velocity, temperature, and pressure are discretized using the following basis functions:

$$
u(x,t) = \sum_{i=0}^{N} u_i(t)\, \psi_i(x), \tag{A.19}
$$

$$
\theta(x,t) = \sum_{i=0}^{N} \theta_i(t)\, \psi_i(x), \tag{A.20}
$$

$$p(x,t) = \sum_{i=0}^{N-2} p_i(t)\, \psi_i(x), \tag{A.21}$$

where u_i, θ_i, and p_i are the nodal values of velocity, temperature, and pressure at the i-th node, respectively. Given that testing each basis function ψ_j is equivalent to testing with any linear combination of them, Equation A.18 may be expressed in the following equivalent compact matrix formulation:

$$A_{ji}\, u_i(t) = 0, \tag{A.22}$$

$$M_{ij}\, \frac{\partial \hat{u}_j}{\partial t} + A_{ij}(u(t))\, u_j(t) = A_{ij}\, P_j(t) - \frac{Pr}{\sqrt{Ra}}\, D_{ij}\, u_j(t) + Pr\, M_{ij}\, \theta_j(t), \tag{A.23}$$

$$M_{ij}\, \frac{\partial \theta_j}{\partial t} + A_{ij}(u(t))\, \theta_j(t) = -\frac{1}{\sqrt{Ra}}\, D_{ij}\, \theta_j(t), \tag{A.24}$$

where:

$$A_{ji} = \int_\Omega \psi_j(x)\, \frac{\partial \psi_i(x)}{\partial x}\, d\Omega \approx \sum_{k=0}^{N} \psi_j(x_k)\, \frac{\partial \psi_i(x_k)}{\partial x}\, w_k = \sum_{k=0}^{N} \delta_{jk}\, \frac{\partial \psi_i(x_k)}{\partial x}\, w_k = \frac{\partial \psi_i(x_j)}{\partial x}\, w_j, \tag{A.25}$$

$$M_{ij} = \int_\Omega \psi_j(x)\, \psi_i(x)\, d\Omega \approx \sum_{k=0}^{N} \psi_j(x_k)\, \psi_i(x_k)\, w_k = \sum_{k=0}^{N} \delta_{jk}\, \delta_{ik}\, w_k = \delta_{ij} w_i, \tag{A.26}$$

$$\begin{aligned} A_{ji}(u(t)) = \int_\Omega \psi_j(x) \sum_k \psi_k(x)\, u_k(t)\, \frac{\partial \psi_i(x)}{\partial x}\, d\Omega &\approx \sum_{l=0}^{N} \psi_j(x_l) \sum_k \psi_k(x_l)\, u_k(t)\, \frac{\partial \psi_i(x_l)}{\partial x}\, w_l \\ &= \sum_{l=0}^{N} \delta_{jl}\, u_l(t)\, \frac{\partial \psi_i(x_l)}{\partial x}\, w_l = u_j(t)\, \frac{\partial \psi_i(x_j)}{\partial x}\, w_j, \end{aligned} \tag{A.27}$$

$$D_{ij} = \int_\Omega \frac{\partial \psi_j(x)}{\partial x}\, \frac{\partial \psi_i(x)}{\partial x}\, d\Omega \approx \sum_{k=0}^{N} w_k\, \frac{\partial \psi_j(x_k)}{\partial x}\, \frac{\partial \psi_i(x_k)}{\partial x}. \tag{A.28}$$

The weights w_k are derived from the Gauss–Lobatto–Legendre (GLL) quadrature rule. This scheme is based on the property that GLL collocation points enable the exact numerical integration of polynomials of degree up to $2N-1$ [72]. Accordingly, the integral of a function f over a physical element $[x_0, x_1]$ is approximated as:

$$\int_{x_0}^{x_1} f(x)\, dx \;\approx\; \sum_{k=0}^{N} \rho_k\, f(\xi_k)\, |J|, \tag{A.29}$$

where $|J|$ is the Jacobian determinant of the affine mapping:

$$T : [x_0, x_1] \longrightarrow [-1, 1], \qquad x \longmapsto \xi = T(x), \tag{A.30}$$

and ρ_k are the quadrature weights, given by

$$\rho_k^{GLL} = \frac{2}{N(N+1)\left[l_N(\xi_k)\right]^2} \qquad k = 0, \ldots, N. \tag{A.31}$$

For GLL collocation points. Then:

$$w_k = \rho_k|J| \tag{A.32}$$

Although the operator symbol A_{ij} is retained for notational convenience in Equation A.25, its application to the pressure field requires the associated inner product $(\nabla\psi_j, p)$ o be evaluated using Gauss–Legendre (GL) quadrature. The corresponding quadrature weights are given by:

$$\rho_k^{GL} = \frac{2}{(1-\xi_k^2)\,[l'_{N-1}(\xi_k)]^2}, \qquad k = 0, \ldots, N-2, \tag{A.33}$$

A.2.2 Time Integration

For time integration, the non-linear (NL) convective terms are integrated explicitly using a third-order extrapolation scheme (EXT_3) while the linear terms are discretized using a third-order backward differentiation formula (BDF_3). This combined approach is referred to as the BDF_3/EXT_3 scheme:

$$NL\left(\eta^{n+1}\right) \approx \sum_{k=1}^{3} \alpha_k NL\left(\eta^{n+1-k}\right) \tag{A.34}$$

$$\frac{\partial\eta}{\partial t} \approx \sum_{k=0}^{3} \beta_k \eta^{n+1-k} \tag{A.35}$$

where α_k, β_k are the corresponding coefficients of third-order Adam-Bashforth (explicit scheme) and Adam-Moulton (implicit scheme), respectively. See Table A.1 for the corresponding coefficients. The

Table A.1: Coefficients for the BDF_3/EXT_3 scheme [72].

k	0	1	2	3
α_k	0	$23/12$	$-16/12$	$5/12$
β_k	$5/12$	$8/12$	$-1/12$	0

resulting system can be expressed as a linear system of Helmholtz equations:

$$\begin{bmatrix} -\boldsymbol{A} & 0 & 0 \\ \left(\boldsymbol{M}\frac{\beta_0}{\Delta t} + \frac{Pr}{\sqrt{Ra}}\boldsymbol{D}\right) & -\boldsymbol{A}^T & -Pr\boldsymbol{M} \\ 0 & 0 & \left(\boldsymbol{M}\frac{\beta_0}{\Delta t} + \frac{1}{\sqrt{Ra}}\boldsymbol{D}\right) \end{bmatrix} \begin{pmatrix} \boldsymbol{u}^{n+1} \\ \boldsymbol{p}^{n+1} \\ \boldsymbol{\theta}^{n+1} \end{pmatrix} = \begin{pmatrix} 0 \\ -\frac{1}{\Delta t}\sum_{m=1}^{k} \beta_m \boldsymbol{M}\boldsymbol{u}^{n+1-m} - \sum_{m=1}^{k} \alpha_m \boldsymbol{A}(\boldsymbol{u}^{n+1-m})\boldsymbol{u}^{n+1-m} \\ -\frac{1}{\Delta t}\sum_{m=1}^{k} \beta_m \boldsymbol{M}\boldsymbol{\theta}^{n+1-m} - \sum_{m=1}^{k} \alpha_m \boldsymbol{A}(\boldsymbol{u}^{n+1-m})\boldsymbol{\theta}^{n+1-m} \end{pmatrix} \tag{A.36}$$

It is important to note that using this integration scheme decouples the energy equation from the rest of the system.

A.2.3 Fractional Step Method

The system is solved using a fractional-step method, in which the temperature, velocity, and pressure fields are computed in separate steps. First, the temperature field and an intermediate prediction of the velocity are obtained by solving the Helmholtz equations using the pressure from the previous time step:

$$\begin{bmatrix} \left(\boldsymbol{M}\frac{\beta_0}{\Delta t} + \frac{Pr}{\sqrt{Ra}}\boldsymbol{D}\right) & -Pr\boldsymbol{M} \\ 0 & \left(\boldsymbol{M}\frac{\beta_0}{\Delta t} + \frac{1}{\sqrt{Ra}}\boldsymbol{D}\right) \end{bmatrix} \begin{pmatrix} \boldsymbol{u}^{*} \\ \boldsymbol{\theta}^{n+1} \end{pmatrix} = \begin{pmatrix} -\frac{1}{\Delta t}\sum_{m=1}^{k} \beta_m \boldsymbol{M}\boldsymbol{u}^{n+1-m} - \sum_{m=1}^{k} \alpha_m \boldsymbol{A}(\boldsymbol{u}^{n+1-m})\boldsymbol{u}^{n+1-m} + \boldsymbol{A}^T\boldsymbol{p}^n \\ -\frac{1}{\Delta t}\sum_{m=1}^{k} \beta_m \boldsymbol{M}\boldsymbol{\theta}^{n+1-m} - \sum_{m=1}^{k} \alpha_m \boldsymbol{A}(\boldsymbol{u}^{n+1-m})\boldsymbol{\theta}^{n+1-m} \end{pmatrix}. \tag{A.37}$$

Then, a pressure correction is computed:

$$\boldsymbol{p}^{n+1} = \boldsymbol{p}^n + \delta\boldsymbol{p} \tag{A.38}$$

$$\boldsymbol{u}^{n+1} = \Delta t \boldsymbol{M}^{-1}\boldsymbol{A}^T\delta\boldsymbol{p} + \boldsymbol{u}^*. \tag{A.39}$$

And to ensure a divergence-free velocity field, multiplying the previous equation by $\boldsymbol{A}$ leads to a Poisson equation for the correction of pressure:

$$\boldsymbol{A}\boldsymbol{M}^{-1}\boldsymbol{A}^T\delta\boldsymbol{p} = -\frac{1}{\Delta t}\boldsymbol{A}\boldsymbol{u}^*. \tag{A.40}$$

A.2.4 Generalized Minimal Residual Method

The resulting linear system of equations is then solved using the generalized minimal residual method (GMRES) for velocity and temperature. Considering the $n \times n$ linear system $\boldsymbol{A}\boldsymbol{x} = \boldsymbol{b}$, the GMRES method finds approximate solutions $\tilde{\boldsymbol{x}}$ belonging to a lower-dimensional Krylov subspace $\mathcal{K}_m$ of order m, which is generated by the matrix $\boldsymbol{A}$ and vector $\boldsymbol{b}$:

$$\mathcal{K}_m(\boldsymbol{A}, \boldsymbol{b}) = \text{span}\{\boldsymbol{b}, \boldsymbol{A}\boldsymbol{b}, \boldsymbol{A}^2\boldsymbol{b}, ..., \boldsymbol{A}^{m-1}\boldsymbol{b}\}. \tag{A.41}$$

If the matrix $\boldsymbol{A}$ is nonsingular, the exact solution for $\boldsymbol{x}$ is guaranteed to lie in a Krylov subspace [73]. However, an acceptable approximation can be obtained for a given tolerance long before the exact solution is found, particularly when effective preconditioning is employed [74]. The method minimizes $||\boldsymbol{b} - \boldsymbol{A}\boldsymbol{x}||_2$ using the Arnoldi iteration. An $(m+1) \times m$ upper Hessenberg matrix and an $(n \times m)$ orthonormal matrix $\boldsymbol{V}_m$ whose columns represent an orthonormal basis of the Krylov subspace $\mathcal{K}_m(\boldsymbol{A}, \boldsymbol{b})$ are constructed, satisfying:

$$\boldsymbol{A}\boldsymbol{V}_m = \boldsymbol{V}_{m+1}\bar{\boldsymbol{H}}_m. \tag{A.42}$$

At iteration m, the approximate solution is sought within the Krylov subspace and written as

$$\tilde{\boldsymbol{x}} = \boldsymbol{V}_m\tilde{\boldsymbol{y}}, \tag{A.43}$$

with

$$\tilde{\boldsymbol{y}} = \arg\min_{\boldsymbol{y}\in\mathbb{R}^m} ||\boldsymbol{e}_1||\boldsymbol{b}|| - \bar{\boldsymbol{H}}_{\boldsymbol{m}}\boldsymbol{y}||_2, \tag{A.44}$$

where $\boldsymbol{e}_1 = (1, 0, 0, ..., 0)^T \in \mathbb{R}^{m+1}$ is the first vector of the standard basis. This linear least-squares problem is efficiently solved using Givens rotations to transform the Hessenberg matrix $\bar{\boldsymbol{H}}_m$ into the $(m+1) \times m$ matrix $\bar{\boldsymbol{R}}_m = \boldsymbol{G}_m...\boldsymbol{G}_2\boldsymbol{G}_1\bar{\boldsymbol{H}}_m$ that is an upper triangular matrix with an added row of zeros. The minimization problem becomes

$$\tilde{\boldsymbol{y}} = \arg\min_{\boldsymbol{y}\in\mathbb{R}^m} ||\boldsymbol{\gamma}_m - \bar{\boldsymbol{R}}_m\boldsymbol{y}||_2, \tag{A.45}$$

where $\boldsymbol{\gamma}_m = \boldsymbol{G}_m...\boldsymbol{G}_2\boldsymbol{G}_1\boldsymbol{e}_1||\boldsymbol{b}||$, allowing the residual to be monitored and convergence to be assessed without explicitly computing the full solution at every iteration. Once the convergence criterion is met, the final approximate solution is recovered by solving a small least-squares problem followed by backward substitution.

The pressure Poisson equation is solved using the GMRES method combined with a Schwarz-based preconditioner, an efficient domain decomposition technique originating from Schwarz's alternating method. In this approach, the global computational domain is decomposed into partially overlapping subdomains, on which local problems are solved independently and combined iteratively to construct the global solution. While a one-level Schwarz preconditioner efficiently reduces high-frequency (local) error components, its convergence deteriorates as the number of subdomains increases due to the persistence of low-frequency (global) error modes. To address this limitation, a two-level preconditioner is employed by incorporating a coarse-grid correction, which captures global information by solving an auxiliary problem on a reduced spectral element mesh [75]. The combination of two overlapping Schwarz solvers with a coarse-grid correction, referred to as SEMG (Spectral Element Multigrid), effectively couples all subdomains at each iteration and significantly accelerates the convergence of the GMRES solver.

Appendix B

Slices of Average Velocity Components

This appendix presents slices of the time-averaged velocity components for the simulation of $Ra = 10^{10}$ discussed in chapter 5, subsection 5.2.1.

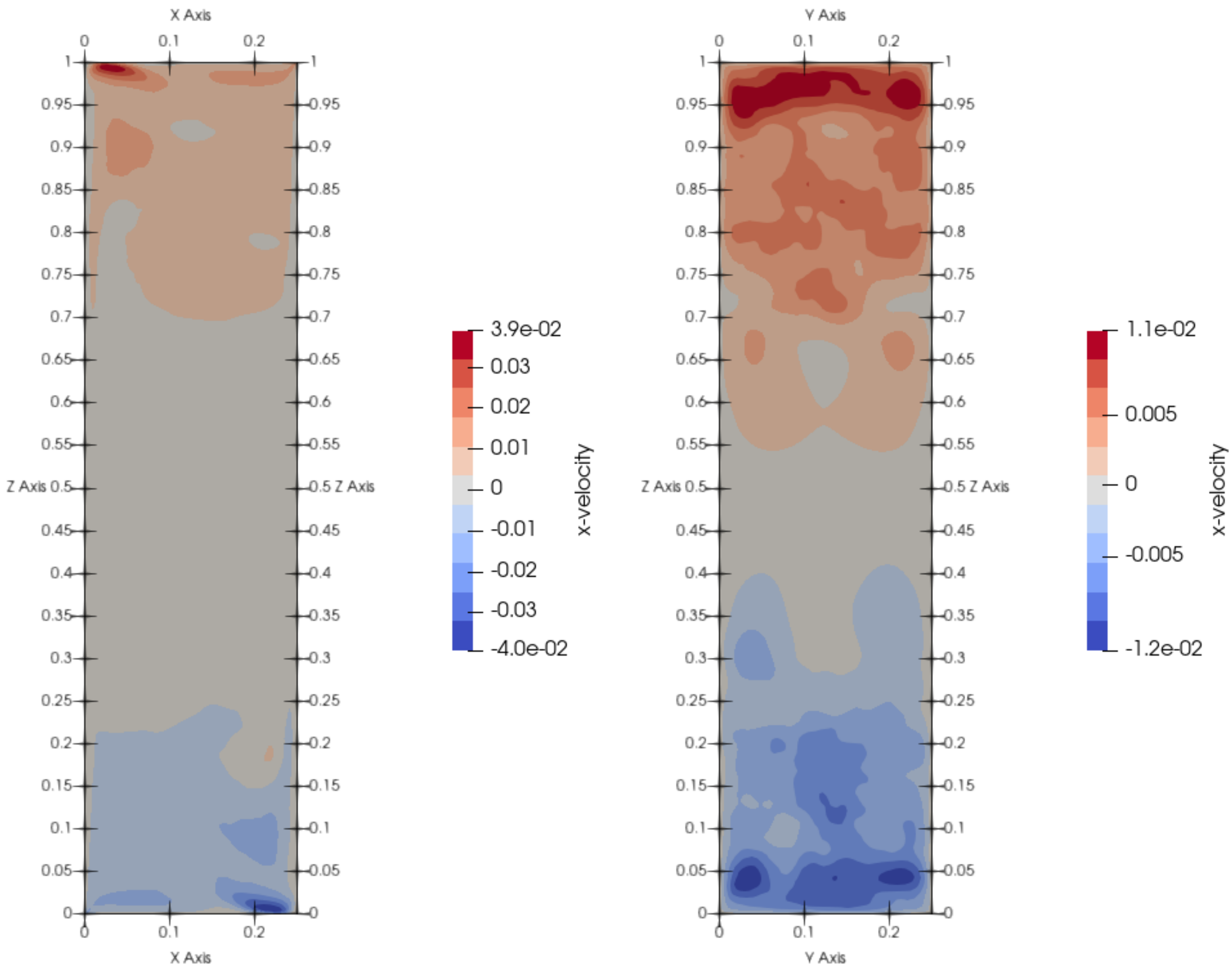

Figure B.1: Slices of average x-velocity component for $Ra = 10^{10}$, (left) $y = 0.125$ and (right) $x = 0.125$.

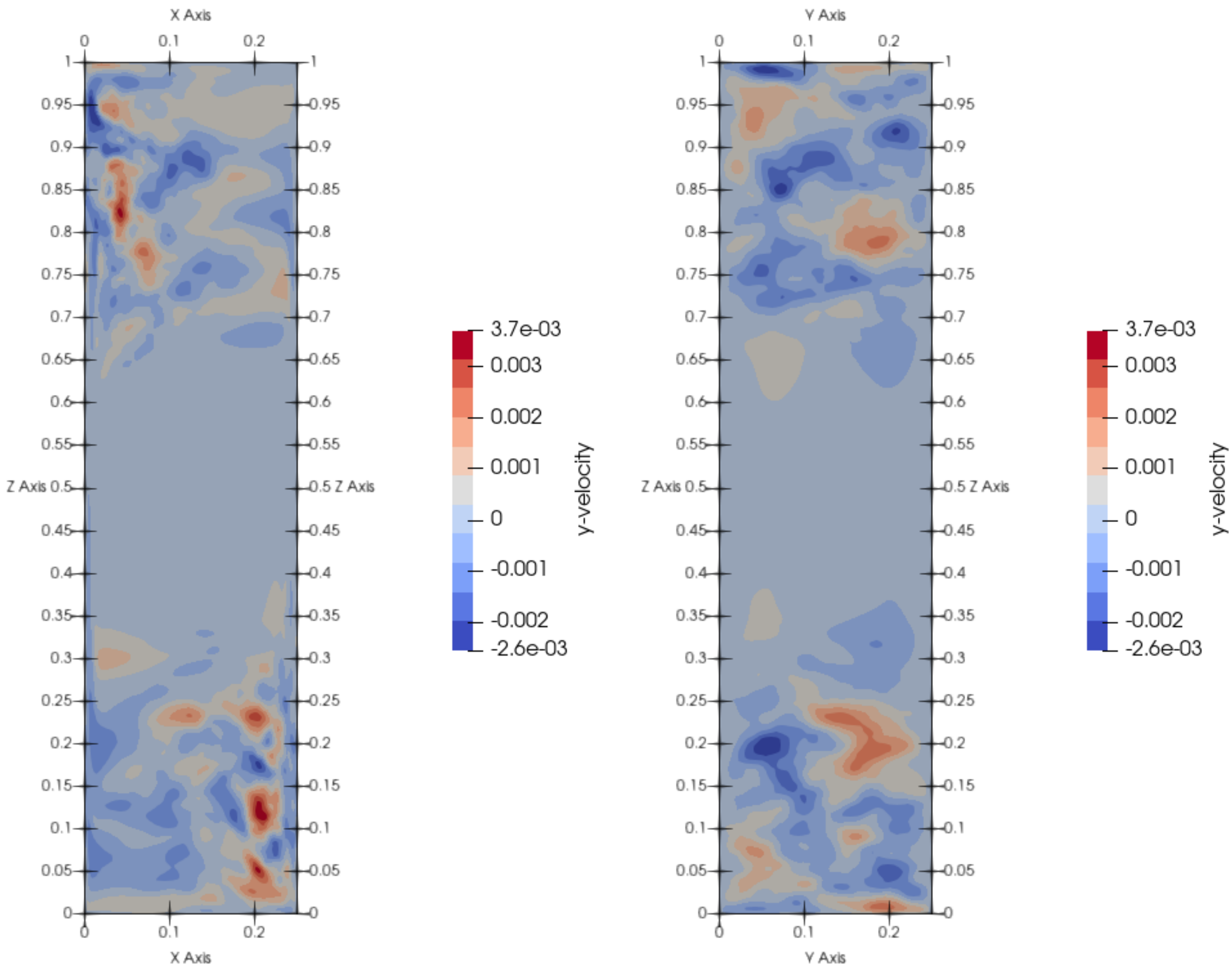

Figure B.2: Slices of average y-velocity component for $Ra = 10^{10}$, (left) $y = 0.125$ and (right) $x = 0.125$.

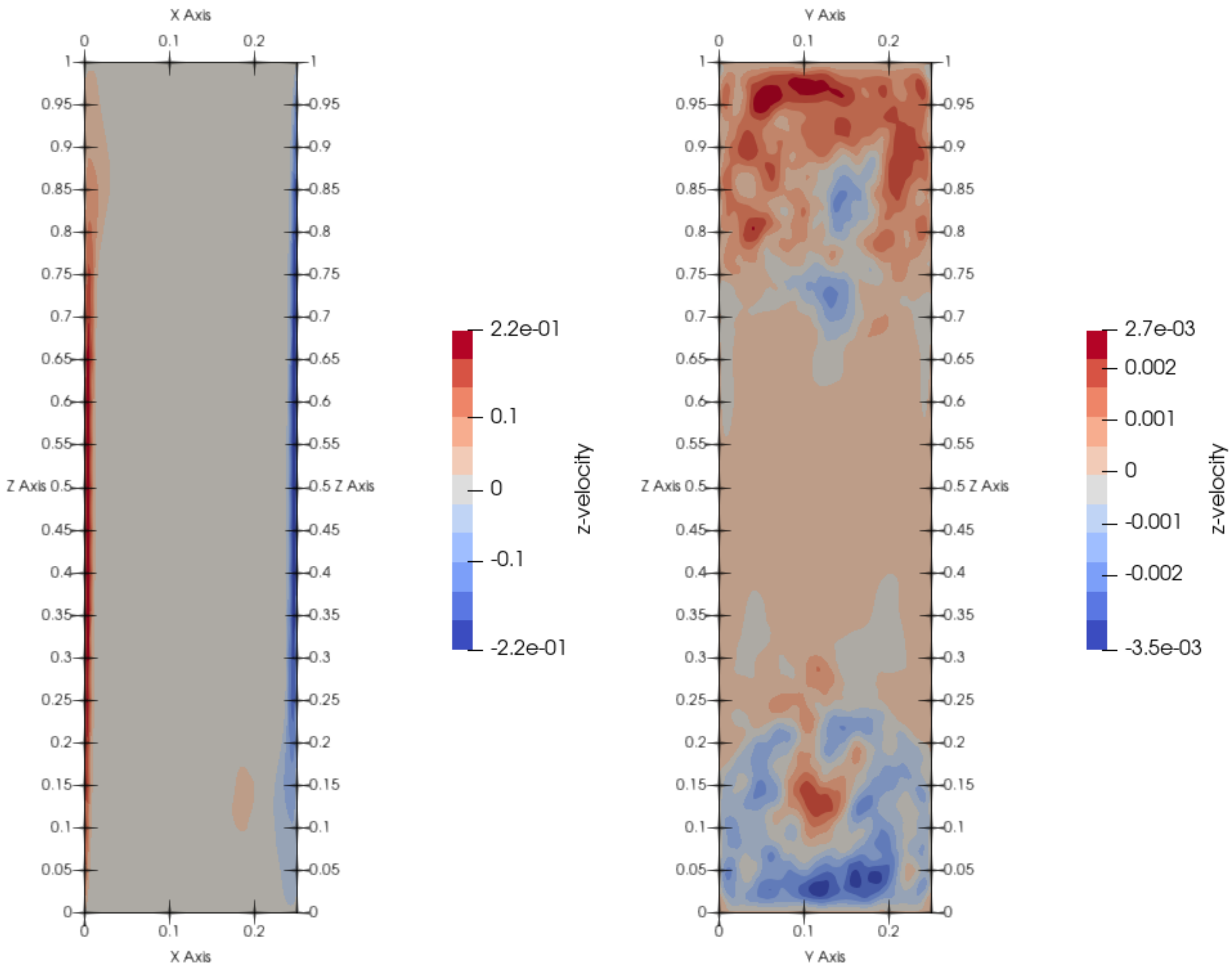

Figure B.3: Slices of average z-velocity component for $Ra = 10^{10}$, (left) $y = 0.125$ and (right) $x = 0.125$.